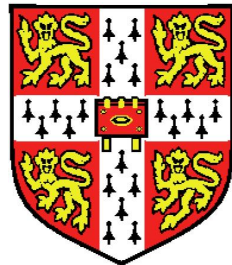


Plasmonic Properties of Metal Nanovoids



Robin Mark Cole
Jesus College
University of Cambridge

A thesis submitted for the degree of
Doctor of Philosophy
July 2009

Declaration

This dissertation is the result of my own work and includes nothing which is the outcome of work done in collaboration except where specifically indicated in the text. This work has not been submitted for a degree, diploma or any other qualification at any other university.

Acknowledgements

I would like to thank my supervisor, Professor Jeremy Baumberg, for all his hard work and guidance on this project. His enthusiasm and tenacity have been a source of constant inspiration over the last three years. I would also like to thank Dr Sumeet Mahajan, for producing many of the beautiful samples investigated in this thesis, and for the many fruitful discussions about the science of these structures. I extend my thanks to Professor Javier Garcia de Abajo, for helping develop the theory describing these structures and providing the opportunity for international collaboration. I would like to thank Dr Tim Kelf and Dr Yoshiro Sugawara who helped get this project off to a flying start. I would also like to thank everyone in the nano-photonics group for all their collaboration, discussions and entertaining company over many lunch times. I would finally like to thank my family for their support and encouragement over the years, along with everyone else who has helped me to fulfil this goal.

Abstract

This thesis describes a study into the plasmonic properties of nano-structured metallic films. Structures are produced by electrochemically depositing metal through a self-assembled template of polymer micro-spheres. This versatile technique allows nano-structures made from metals which can be electrodeposited to be produced quickly and cheaply. Geometries ranging from arrays of shallow dishes, to sharp metallic spikes and encapsulated spherical cavities can all be produced on the same sample. This thesis presents an in-depth study into the properties of delocalised and localised surface plasmons on these structures. These plasmons can be tuned in energy by controlling the sample geometry and local dielectric environment. Techniques are explored for modifying the energy, absorption strength and field distribution of plasmon modes for specific applications. With an understanding into the plasmonic properties of the metallic nano-structures, research is undertaken to explore how the associated local electric-field couples to molecules adsorbed onto a sample surface. The role of specific plasmon modes in enhanced Raman scattering is identified, and then optimised using multilayer nanostructures with tailored plasmon modes. Finally, the use of flexible elastomeric substrates for mechanically tuneable plasmonic substrates is explored. Initial experiments confirm the feasibility of such an approach and pave the way for further research.

Contents

| | |
|--|-----------|
| Table of Contents | vi |
| Nomenclature | x |
| 1 Introduction | 1 |
| 2 Optical Properties of Metals | 6 |
| 2.1 Inspired by Nature | 6 |
| 2.2 Modern Photonics | 7 |
| 2.3 Metals | 10 |
| 2.4 Fundamental Optical Properties | 12 |
| 2.5 Optical Response | 13 |
| 2.6 Real Metals | 17 |
| 2.7 Surface Plasmon Polaritons | 20 |
| 2.8 Plasmons on Silver, Gold and Aluminium | 23 |
| 2.9 Grating Coupling to Surface Plasmons | 26 |
| 3 Sample Production and Analysis | 28 |
| 3.1 Sample Preparation | 28 |
| 3.1.1 Template Preparation | 28 |
| 3.1.2 Electrochemical Deposition | 30 |
| 3.2 Sample Characterisation | 33 |
| 3.2.1 SEM Characterisation | 33 |
| 3.2.2 (Quick) Optical Analysis | 34 |
| 3.3 Conclusions | 36 |

CONTENTS

| | |
|---|------------|
| 4 Experimental Setup | 37 |
| 4.1 Experimental Setup | 37 |
| 4.2 Data Presentation | 39 |
| 5 Types of Plasmon | 41 |
| 5.1 Introduction | 41 |
| 5.2 Bragg Plasmons | 42 |
| 5.3 Void Plasmons | 46 |
| 5.4 Low Energy Plasmon Mode | 57 |
| 5.5 SNOM Mapping of Void Plasmons | 60 |
| 5.6 Conclusion | 63 |
| 6 Plasmon Interaction and Control | 64 |
| 6.1 Introduction | 64 |
| 6.2 Tuning Plasmons with Refractive Index | 65 |
| 6.3 Microsphere Samples | 66 |
| 6.4 Trench Guided Plasmons | 76 |
| 6.5 Hybrid Nanovoids | 78 |
| 6.6 Conclusions | 85 |
| 7 Surface Enhanced Raman Spectroscopy on Nanovoids | 86 |
| 7.1 Introduction | 86 |
| 7.2 Raman Spectroscopy | 87 |
| 7.3 SERS on Nanovoids | 88 |
| 7.4 SERS on Hybrid Nanovoids | 98 |
| 7.5 Conclusions | 104 |
| 8 Flexible Plasmonics | 105 |
| 8.1 Introduction | 105 |
| 8.2 Stretchable 1D and 2D Diffraction Gratings | 106 |
| 8.3 Metal Films on Elastomers | 109 |
| 8.4 Flexible Metal-Elastomer Nanostructures | 112 |
| 8.4.1 Flexible Nanovoids | 114 |
| 8.5 Tuneable Nanotriangle Substrates | 119 |

CONTENTS

| | |
|---|------------|
| 8.6 Conclusion | 122 |
| 9 Conclusions | 123 |
| A Derivations | 127 |
| A.1 Finding Electric Charge Density | 127 |
| A.2 Resonant Plasmon Model | 128 |
| B Publications | 131 |
| References | 144 |

Nomenclature

Roman Symbols

| | |
|-----------|--|
| \bar{n} | Effective refractive index |
| \bar{t} | Normalised sample thickness |
| \hat{k} | Complex wave vector = $k' + ik''$ |
| \hat{n} | Complex refractive index = $n + i\kappa$ |
| κ | Extinction coefficient |
| B | Magnetic induction vector |
| D | Electric displacement vector |
| E | Electric field vector |
| H | Magnetic vector |
| J | Current density |
| r | Spatial vector |
| a | Period of a structure |
| b | Damping coefficient |
| c | Speed of light = $2.998 \times 10^8 \text{ ms}^{-1}$ |
| e | Electron charge = $1.602 \times 10^{-19} \text{ C}$ |

| | |
|-------|---|
| G | Reciprocal lattice vector |
| h | Planck's constant = $6.626 \times 10^{-34} \text{ Js}$ |
| I | Intensity |
| i | Imaginary number = $\sqrt{-1}$ |
| K | Spring constant |
| k | Wave vector |
| M | Transition moment |
| m | Mass |
| N | Number of molecules |
| n | Refractive index |
| N_A | Avogadro's number = $6.022 \times 10^{23} \text{ mol}^{-1}$ |
| n_e | Density of electrons |
| P | Dipole moment |
| t | Time |
| x | Displacement |

Greek Symbols

| | |
|------------------|---|
| δ | skin depth |
| ϵ | Dielectric constant |
| γ | Damping coefficient |
| $\hat{\epsilon}$ | Complex dielectric constant = $\epsilon_1 + i\epsilon_2$ |
| λ | Wavelength |
| μ | Free space magnetic permeability = $4 \times 10^{-7} \text{ Hm}^{-1}$ |

| | |
|----------------|--------------------------------------|
| ν | Frequency |
| ω | Angular frequency = $2\pi\nu$ |
| ω_0 | Resonant frequency |
| ω_p | Bulk plasma frequency |
| ω_{spp} | Surface plasmon polariton frequency |
| ϕ | Sample orientation |
| ρ | Charge density |
| σ | Conductivity |
| τ | Relaxation time |
| θ | Incident angle |
| k_{spp} | Surface plasmon polariton wavevector |

Acronyms

| | |
|-------------|--|
| <i>BEM</i> | Boundary element method |
| <i>FWHM</i> | Full width at half maximum |
| <i>HWHM</i> | Half width at half maximum |
| <i>NA</i> | Numerical aperture |
| <i>NIR</i> | Near infrared |
| <i>RPP</i> | Radiative plasmon polariton |
| <i>SEM</i> | Scanning electron microscopy |
| <i>SERS</i> | Surface enhanced Raman scattering |
| <i>SNOM</i> | Scanning near-field optical microscopy |
| <i>SPP</i> | Surface plasmon polariton |

Nomenclature

SRR Split-ring resonator

TE Transverse Electric polarisation

TM Transverse Magnetic polarisation

UV Ultraviolet

WGM Whispering gallery mode

Chapter 1

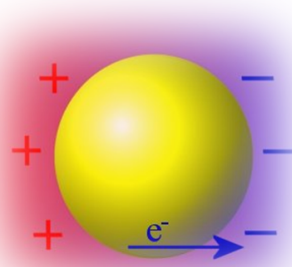
Introduction

In recent years there has been an increasing amount of interest in controlling the interaction between light and metals by creating nanostructures on length scales similar to or smaller than the wavelength of the light involved. The Romans were the first to exploit the optical properties of nanoscale metal colloids, using them to create exquisitely coloured objects such as the Lycurgus cup pictured in figure 1.1(a). Although unknown to them at the time, the fantastic colouration of the cup is due to the size-dependent interaction of light with surface charges on the colloids. These form an electron gas that moves away from its equilibrium position when perturbed by an incident light-field, inducing surface polarisation charges that act as a restoring force on the electron gas, shown in figure 1.1(b). This results in collective oscillatory motion of the electrons which is characterised by a dominant resonance band lying in the vis-NIR spectral region for gold, referred to as the plasmon resonance.

However plasmon resonances are not limited to particles, and can be excited on planar 2D surfaces as well as more complex geometries such as cavities, tips and gratings. Plasmon resonances generate intense electric fields at the metal surface which are exploited for a range of applications, such as molecule sensing via surface enhanced Raman spectroscopy, and to create novel photovoltaics. There have been many types of nanostructure demonstrated for these applications, however in practice the optimisation of these structures is hindered by a lack of understanding of the fundamental properties of plasmons in nanostructures.



(a)



(b)

Figure 1.1: (a) the Lycurgus Cup, made in the 4th century AD [from reference (1)]. (b) Schematic nanoparticle plasmon resonance.

A plasmonic nanostructure which has shown enormous potential for a wide range of applications is the nanovoid structure investigated in this thesis. These are periodic metal nanostructures which are produced using a self-assembly and electrochemical deposition process. A schematic of one such sample is shown in figure 1.2(a). The surfaces produced through this natural lithography are of excellent quality in terms of both smoothness and regularity and can be fabricated using a wide range of materials. These samples support both localised and propagating plasmons depending on the structure geometry, \bar{t} , defined in figure 1.2(a). Propagating plasmons are referred to as Bragg plasmons due to their coupling via Bragg diffraction, and have an energy strongly dependent on their in-plane wavevector k , as shown in figure 1.2(b). For thick nanovoid structures (around $\bar{t} \approx 1$) the structure represents almost completely encapsulated spherical cavities and plasmons can become localised within individual voids. The localised nature of these plasmons in real space is confirmed by their broad angular range in k -space, and modes have energies independent of the incident angle of excitation light and sample orientation, as shown in figure 1.2(c). Therefore angle-resolved spectroscopy measurements are utilised throughout this thesis to characterise the observed plasmon modes of nanovoid samples.

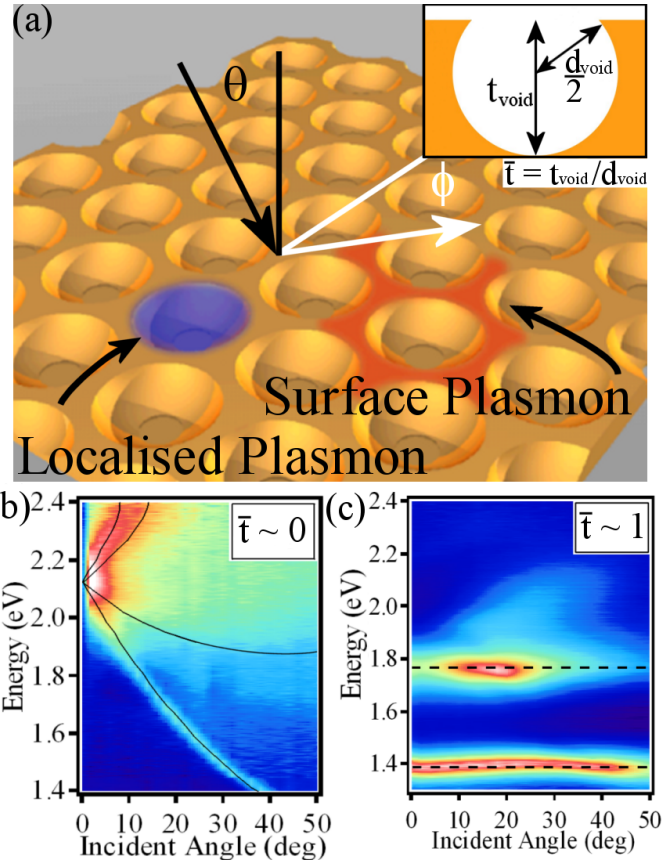


Figure 1.2: (a) Schematic of delocalised surface plasmons (red) and localised plasmons (blue) existing on gold nanovoid surfaces (2). θ is the angle of incidence with respect to the normal, and ϕ the angle with respect to the hexagonal lattice director. (b,c) Typical experimental angle-dependent plasmon dispersions, with absorption from 0 % (dark blue) to 80% (red/white), for (b) a delocalised surface plasmon (black lines indicate theoretical dispersion modelled using an empty lattice scattering equation), and (c) a localised plasmon (dashed lines indicate the expected plasmon energy). The existence of the different plasmons depends on the thickness of the metal, where normalised thickness $\bar{t} = \text{thickness}(t)/\text{diameter}(d)$.

Understanding the properties of the different plasmon modes is crucial for the optimisation of nanovoid structures for applications such as surface enhanced Raman scattering (*SERS*). This thesis collects related experiments and calculations performed by the author over the past three years. The topics span from the fundamental characterisation of the surfaces, through the analysis of the plasmonic properties, to the interaction of plasmons with molecules adsorbed on the structure. This requires the partitioning of this thesis into a number of chapters as outlined below.

Chapter 2 provides a brief introduction to the optical properties of nanostructures and gives an overview of the range of nano-structured devices currently being investigated for plasmonic applications. The fundamental optical properties of metals are presented, before looking at the formation of surface plasmons from a theoretical viewpoint. Plasmons are shown to exist as both localised and delocalised states, which exhibit very different characteristics.

Chapter 3 subsequently describes the nanovoid fabrication process and presents a brief analysis of the sample properties using *SEM* imaging to characterise the structure morphology and microscope reflectivity measurements to observe the plasmon resonances of these structures.

Chapter 4 then outlines the setup of the experiments performed using a computer controlled goniometer. This setup produces large volumes of data and so an explanation into the different graphical representation techniques is also presented.

After this thorough background, chapter 5 outlines the experiments performed to characterise the different types of surface plasmon found on the nanovoid structure. These fall into two categories, those of localised and delocalised modes. Delocalised plasmons are highly dependent on the sample orientation as well as the incident angle of the light source. Localised plasmons on the other hand have an isotropic dispersion. These plasmons are studied in detail and an understanding of their properties is presented.

With many of the fundamental properties of the plasmons in nanovoids acquired, chapter 6 then discusses various techniques for modifying or tuning the properties of plasmons. It is shown that the energy of plasmon resonances can

be tuned simply by altering the refractive index at the metal/dielectric interface. Secondly, fabricating samples where the spheres remain embedded within the structure produces new propagating surface modes with modified dispersion properties, useful for coupling light into micro-spheres. It is then shown that by placing nanovoids into linear arrays, it is possible to guide plasmons in specific directions along a sample, producing a plasmon waveguide. Finally, the properties of specific plasmon modes are investigated by fabricating hybrid nanovoid structures, composed of layers of different metals.

Chapter 7 explains the current theoretical knowledge of surface enhanced Raman scattering (*SERS*), and discusses the experimental *SERS* results obtained. These identify the specific plasmon modes responsible for *SERS* enhancement on nanovoid substrates and reveal the relationship between absorption, light coupling and *SERS* enhancement.

Chapter 8 then discusses some more recent work, describing the fabrication of mechanically stretchable plasmonic substrates. Using simple fabrication techniques it is possible to produce a range of flexible structures, such as nanovoids, gratings and triangle arrays. Initial experiments are presented which indicate that it is possible to actively tune plasmon resonances on these structures, with potential applications including tuneable *SERS* substrates and new colour changing materials.

Finally, chapter 9 summarises the finding of the previous chapters and speculates on the future research directions that may be of interest.

Chapter 2

Optical Properties of Metals

Modern technology has given us incredibly powerful tools to control and manipulate light, from the ability to produce and manipulate individual photons, to systems which rapidly distribute information on a global scale. However, millions of years before these recent advances, nature evolved sophisticated systems to control light which science is still striving to reproduce.

2.1 Inspired by Nature

Although much colouration in the natural world is due the absorption of light by pigments, there are many examples of colour by various optical phenomena such as interference, diffraction and scattering. In the latter, colouration is referred to as structural colour, because the interaction between light and a sub-micron structure is intrinsic to the phenomena. A striking example of structural colour in nature is the iridescent wings of the Morpho butterfly, shown in figure 2.1(a). Here the structure of the butterfly wing forbids the transmission of blue light (a phenomena known as a photonic crystal band-gap), giving the wing a bright opalescent blue colouration⁽³⁾. *SEM* imaging reveals extremely fine scales covering the butterfly wings which reflect incident light repeatedly at successive periodically spaced layers, leading to interference effects that depend on both the wavelength and angle of incidence. Such a periodically structured optical material is referred to as a photonic crystal, of which there are many examples in nature. A range of colours is observed in peacock feathers, shown in figure 2.1(c).

Each colour is uniquely achieved by variations in the periodicity of the feather nanostructure.

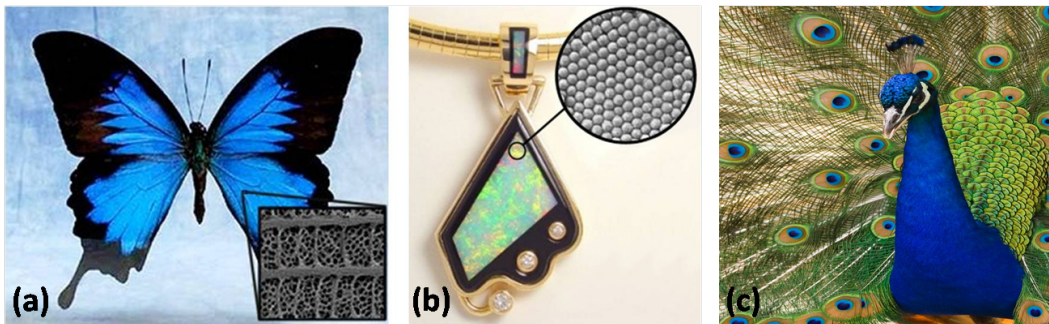


Figure 2.1: (a) The Morpho butterfly is highly iridescent due to nano-structuring of its wings (inset) [from reference (3)]. (b) Natural opal is iridescent and colourful due to its structure (inset), making it ideal for jewellery [from reference (4)]. (c) A range of colours in peacock feathers is achieved by variations in the lattice constant and the number of periods in the photonic-crystal structure, from reference (5).

Naturally occurring photonic crystals are not just limited to biologically directed systems. Another example of a photonic crystal is the naturally occurring gemstone opal, shown in figure 2.1(b). At the nanoscale, opal is composed of ≈ 250 nm diameter silica spheres (6) arranged in a closed-packed lattice, forming a natural 3D photonic crystal bearing a close resemblance to some of the structures investigated in this thesis. The 3D structure of opals is formed by a process of self-assembly in which a mix of precursors are directed to form complex structures by the interplay of various packing forces. Due to the diversity and sheer abundance of natural photonic systems, it should come as no surprise that they are providing inspiration for a wealth of novel technological applications.

2.2 Modern Photonics

Perhaps the area of life in which modern optical technologies have had the most significant impact is in communication. Optical telecommunications systems have

surpassed traditional copper wire technology, providing an immense capacity to distribute information globally and enabling lifestyle changing technologies such as the internet. There is a global push toward developing technology which can manipulate the interaction between light and matter, at ever decreasing time scales and size dimensions. Among the challenges facing modern technology is that of integrating optical and electronic communication systems. The current necessity to switch between photonics for information transport and electronics for data handling, limits the potential operating speeds of future technology.

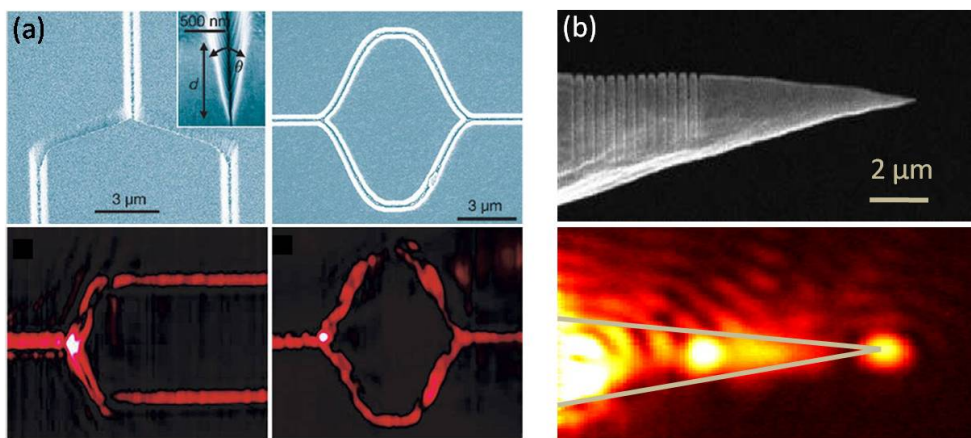


Figure 2.2: (a) Plasmonic Y-splitter and Mach-Zehnder interferometer showing (top) *SEM* and (bottom) *SNOM* images [from reference (7)]. (b) (top) *SEM* image showing a nanoscale tip with a grating on its shaft [from reference (8)], (bottom) scattered light images with the tip shape indicated in gray showing plasmon coupling by the grating and localisation at the tip apex.

A technology which shows huge potential to overcome this obstacle is that of engineered surface plasmon polaritons (henceforth referred to as plasmons or *SPPs*). A plasmon is a quasiparticle composed of a photon coupled to an electric charge fluctuation, bound to a metal surface. *SPPs* therefore bridge the gap between photonic and electronic systems and have been the subject of intensive research, both into their physical properties and potential applications. One of the most attractive properties of *SPPs* is the way in which they can be used to concentrate and channel light using subwavelength structures(9). *SPPs* may

one day be utilised in miniaturised integrated photonic circuits with size scales much smaller than those currently possible(10; 11). Such devices would require a variety of plasmonic components, many of which have already been demonstrated in principle; including waveguides(7), switches(12) and couplers(8).

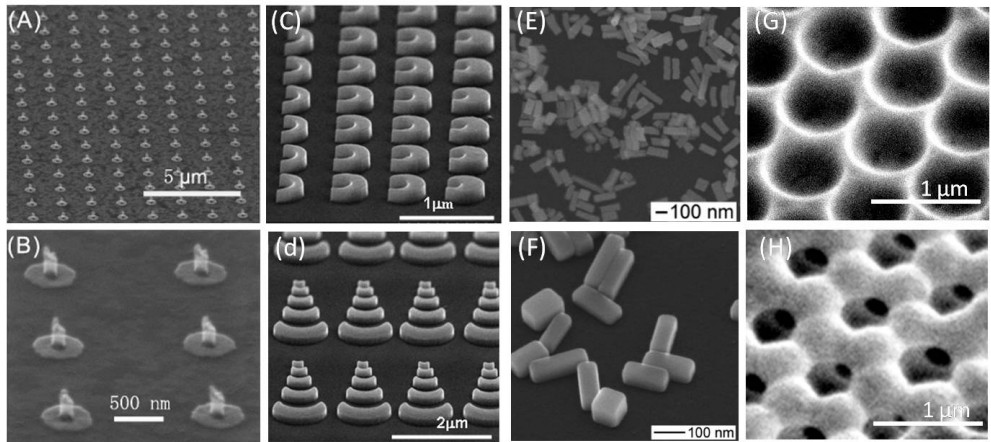


Figure 2.3: (a) *SEM* image of a nanopin array and (b) zoomed-in [from reference (13)]. (c) *SEM* images of nanocrescents with an external curvature radius of 200 nm but different openings and (d) array of nanocrescents with different external radii ranging from 400 nm down to 200 nm [from reference (14)]. (e) *SEM* image of silver nanobars and (f) of the same sample tilted by 45° [from reference (15)]. (g) *SEM* image of a thin 600 nm diameter nanovoid surface and (h) a thick surface.

Concentrating light in the form of a plasmon creates a spatially localised enhanced electric field that can be used to manipulate light-matter interactions and amplify non-linear phenomena. For instance, the enhanced electric fields of *SPPs* can be applied to identify molecules attached to a surface by a process known as surface enhanced Raman spectroscopy (*SERS*); a technique that is capable of detecting single molecules(16; 17). There have been considerable efforts toward fabricating nanostructures which generate large field enhancements in a controllable way, and many types of structure have been demonstrated. These include sharp metal tips(18; 19; 20), dielectric conical tips coated with metal films(21; 22; 23; 24), particles(25), plasmonic lenses(26), sharp metallic grooves

and wedges(23; 27; 28; 29), burgers(30), triangular prisms(31), pins(13) (figure 2.3(a,b)), cages(32), cubes(33), crescents(14) (figure 2.3(c,d)), bars and rice(15) (figure 2.3(e,f)), and the nanovoids (figure 2.3(g,h)) described in this thesis.

However in many of these structures the fields generated are neither precisely understood or well controlled. It has therefore been the aim of this thesis to investigate in detail all aspects of the nanovoid plasmonic behaviour in order to both advance our understanding of the physics of these structures and develop the ability to manipulate their plasmonic properties for specific applications.

2.3 Metals

Highly reflective metal surfaces have a long history of being utilised for their optical properties. Greco-Roman historians recorded how at the Roman siege of Syracuse from 214 to 212 B.C., the ancient Greek mathematician Archimedes used an array of bronze mirrors to focus sunlight onto advancing Roman ships, setting them on fire and repelling the invasion(34). However perhaps the earliest recorded use of metals for their optical qualities is as decorative jewelry, with copper examples dating back over 7000 years(35). The most commonly used metal for decorative purposes is gold, which in its pure form is a pleasing yellow colour. Ancient jewelery makers understood that gold could be alloyed with other metals such as copper, zinc and silver to produce metals with entirely new colours, such as orange, blue or white; this is perhaps one of the earliest example of optical engineering.

Colloidal metal nano-particles have been used as colourants for over 2000 years, when gold nano-particles were used to create extraordinary colourations in stained glass. A fantastic example of this technology is the Lycurgus cup, manufactured in Rome around 400 A.D. (figure 2.4). Here, surface plasmon resonances of the metal particles efficiently scatter green light, giving the cup its unusual colour. This allows only red light to be transmitted, providing a strong contrast in colours to dazzling effect. However, it was not until the turn of the 20th century that the scattering and absorption mechanisms responsible for the optical properties of small metal particles were first understood. The size dependent optical properties of metal spheres were finally explained by Mie in

2.3 Metals

1908([36](#)). However it has taken powerful computational methods to fully understand the plasmon resonances of the anisotropic metal cavities which form the topic of this thesis.

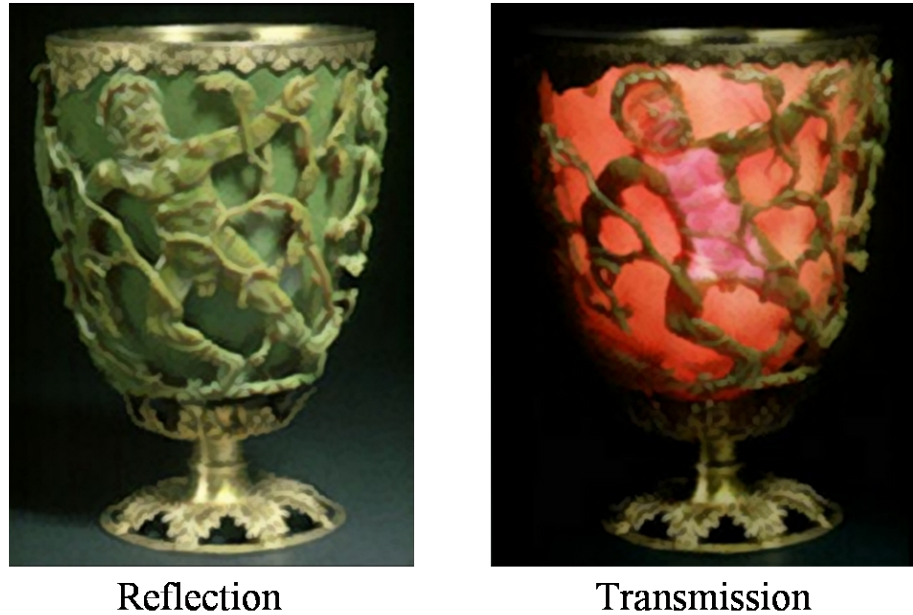


Figure 2.4: The Lycurgus Cup, made in the 4th century AD. The glass contains 70 nm particles of silver and gold with a ratio of about 7:3 which make the cup appear green in reflection but red in transmission [from reference ([1](#))].

2.4 Fundamental Optical Properties

As a first approximation a metal can be considered to be an isotropic medium of dielectric constant ϵ , permeability μ and conductivity σ . Maxwell's equations in S.I. units take the form:

$$\nabla \cdot \mathbf{H} = 0 \quad (2.1)$$

$$\nabla \cdot \mathbf{E} = \frac{\rho}{\epsilon} \quad (2.2)$$

$$\nabla \times \mathbf{E} + \mu \frac{\partial \mathbf{H}}{\partial t} = 0 \quad (2.3)$$

$$\nabla \times \mathbf{H} - \epsilon \frac{\partial \mathbf{E}}{\partial t} = \sigma \mathbf{E} \quad (2.4)$$

Using equations 2.4 and 2.3 an expression for the time variation of the electric charge density ρ can be obtained(37). [See appendix A.1 for the full derivation.] On integration, the solution to this equation takes the form:

$$\rho = \rho_0 e^{-t/\tau} \quad \text{where} \quad \tau = \frac{\epsilon}{\sigma} \quad (2.5)$$

Metals have a large conductivity σ making the relaxation time τ very short; for gold this value is of order 10^{-18}s . Therefore the electric charge density ρ can be set to zero. Now equations 2.4 and 2.3 can be re-arranged to eliminate \mathbf{H} . For monochromatic light and assuming a plane wave solution to Maxwell's equations, \mathbf{E} takes the form:

$$\mathbf{E} = \mathbf{E}_0 \exp(i\mathbf{k} \cdot \mathbf{x} - i\omega t) \quad (2.6)$$

And the wave equations for a metal is given by:

$$\nabla^2 \mathbf{E} + \hat{k}^2 \mathbf{E} = 0 \quad \text{where} \quad \hat{k}^2 = \omega^2 \mu \left(\epsilon + i \frac{\sigma}{\omega} \right) \quad (2.7)$$

These equations are identical to those of a non-conducting medium if a complex dielectric constant, $\hat{\epsilon} = \epsilon + i\frac{\sigma}{\omega} = \epsilon_1 + i\epsilon_2$ is defined. It is also possible to define a complex refractive index, $\hat{n} = n + i\kappa = \sqrt{\hat{\epsilon}\hat{\mu}}$, where κ is the extinction

2.5 Optical Response

coefficient. Refractive index and dielectric constant are then linked through the equations:

$$n = \sqrt{\frac{\sqrt{\epsilon_1^2 + \epsilon_2^2} + \epsilon_1}{2}} \quad \text{and} \quad \kappa = \sqrt{\frac{\sqrt{\epsilon_1^2 + \epsilon_2^2} - \epsilon_1}{2}} \quad (2.8)$$

Taking into account the complex wave vector \hat{k} , the plane wave can be re-written in terms of n and κ :

$$\mathbf{E} = \mathbf{E}_0 \exp\left(\frac{-2\pi\kappa x}{\lambda}\right) \exp\left[i\left(\frac{2\pi nx}{\lambda} - i\omega t\right)\right] \quad (2.9)$$

where the first exponential is real and describes the attenuation of the wave, and is determined by the imaginary part ϵ_2 of the relative dielectric constant. The second exponential is imaginary, corresponding to the oscillatory part of the wave. If $|\epsilon_1| \gg |\epsilon_2|$ then the real part of the refractive index n is mainly determined by ϵ_1 and quantifies the reduction in phase velocity of the propagating wave. A value for the penetration depth, defined as the distance into a material where the wave energy density falls to $1/e$ of its initial value, is known as the skin depth δ where:

$$\delta(\lambda) = \frac{\lambda}{2\pi\kappa(\lambda)} \quad (2.10)$$

For *NIR* frequencies the skin depth of gold is around 20 nm, which is small compared to the wavelength of visible light. Therefore in this regime gold can be considered a perfect reflector, however the situation changes significantly as the wavelength is decreased to the blue region of the spectrum.

2.5 Optical Response

In the previous derivation it was assumed that a metal's conductivity, dielectric constant and magnetic permeability are all constants. In reality these values are dependent on the frequency of the incident field ω . The dielectric constant of a medium is purely dependent on how the electrons within the material respond to an optical field. Electrons can be either bound to the host atoms, as in a dielectric material, or be free to move through the material, as in the case of a

2.5 Optical Response

metal. Since an applied optical field is oscillatory, both cases can be described in terms of simple harmonic motion and are known as the Lorentz and Drude models for dielectrics and metals respectively. The equation for simple harmonic motion of an electron in a material can be written as:

$$m\ddot{x} + b\dot{x} + Kx = e\mathbf{E} \quad (2.11)$$

where m and e are the electron mass and charge, b is the damping coefficient describing the energy loss due to scattering, K is the spring constant describing the restoring force due to electrostatic attraction of the binding atom and \mathbf{E} is the electric field. In a dielectric, electrons fill the valence band and so only interband transitions with large energies are allowed, shown in figure 2.5. If it is assumed that the incident field is less than that required to induce an electronic transition then the material is described directly by equation 2.11. For a perfect metal, free electrons occupy a partially filled conduction band, allowing intraband transitions of very low energies. Therefore, the optical response of a perfect metal can be obtained from the harmonic oscillator model by setting the spring constant K to zero(38). However for real metals, electrons loosely bound to the atoms also contribute to the optical properties, and hence a combination of both descriptions is required.

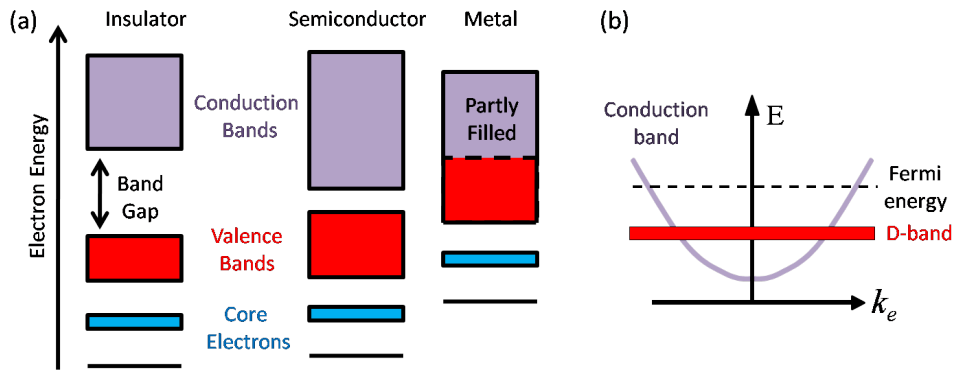


Figure 2.5: (a) Electron bands in non-conductors (insulators and semiconductors) and conductors (metals) (38). (b) Loosely bound electrons in a D-band also contribute to absorption in real metals.

2.5 Optical Response

Upon solving equation 2.11 in terms of the amplitude and phase(37), solutions for the real and imaginary parts of the dielectric constant can be found for both the metal and dielectric cases.

Metal, Drude solution:

$$\epsilon_1 = 1 - \frac{\omega_p^2}{\omega^2 + \gamma^2} \quad \text{and} \quad \epsilon_2 = \frac{\omega_p^2 \gamma}{\omega (\omega^2 + \gamma^2)} \quad (2.12)$$

Dielectric, Lorentz solution:

$$\epsilon_1 = 1 + \frac{\omega_p^2 (\omega_0^2 - \omega^2)}{(\omega_0^2 - \omega^2)^2 + \gamma^2 \omega^2} \quad \text{and} \quad \epsilon_2 = \frac{\omega_p^2 \gamma \omega}{(\omega_0^2 - \omega^2)^2 + \gamma^2 \omega^2} \quad (2.13)$$

Here the plasma frequency is defined as:

$$\omega_p = \sqrt{\frac{n_e e^2}{m \epsilon_0}} \quad (2.14)$$

where n_e is the density of electrons, e is the charge of an electron and m is the mass of an electron. The relationship $\gamma = b/m$ quantifies the damping in the system and $\omega_0 = \sqrt{K/m}$ corresponds to the resonant frequency of the bound electrons in a dielectric medium. These values are plotted in figure 2.6 along with the corresponding complex refractive indices, calculated using equation 2.8.

In the case of a perfect metal, the electrons are free ($\omega_0 = 0$) and embedded within a matrix of positive ions, giving the system zero net charge. Under illumination, these free electrons are displaced and the positive background is no longer screened, producing an attractive force on the neighbouring electrons. These electrons move to the positive region in order to restore charge neutrality. Coulomb repulsion now produces a motion in the opposite direction. This cycle repeats, causing oscillations of the free electron gas. At a frequency known as the plasma frequency ω_p , the dielectric constant passes through zero (figure 2.6(a)), and at this point the wave is purely longitudinal - corresponding to a collective oscillation of the electrons in the direction of the wave propagation. In a quantum mechanical treatment of this problem the collective plasma oscillation is known as a *bulk* plasmon, a quasi-particle made up of the combined effect of many particles.

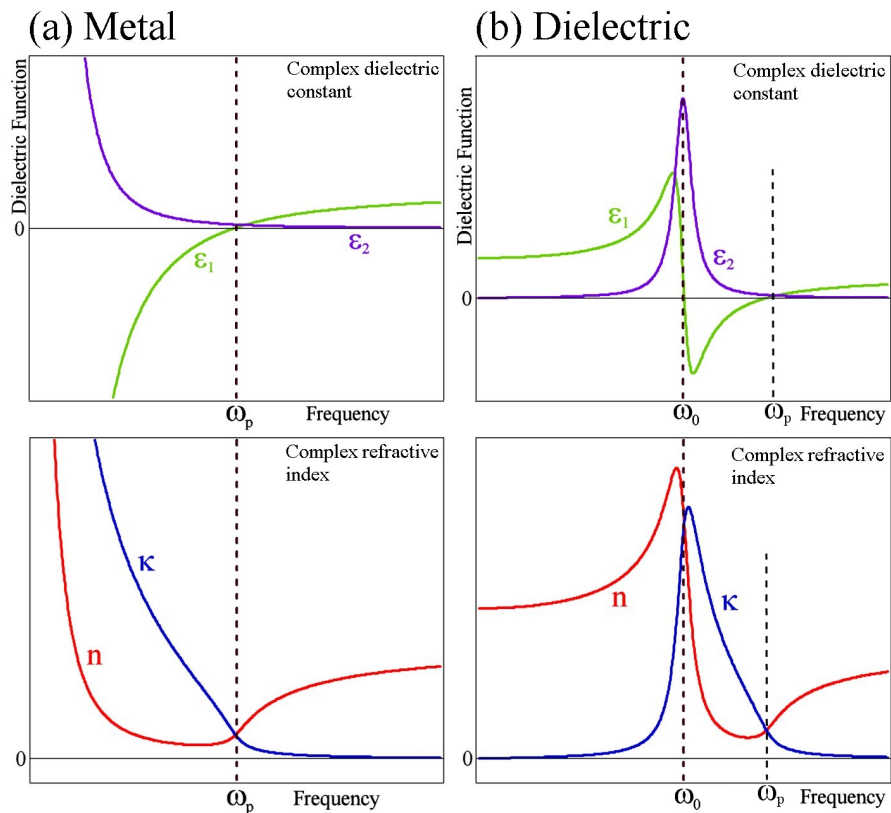


Figure 2.6: Graphs showing the components of the complex dielectric function (top) and the complex refractive index (bottom) for (a) metals, modelled using the Drude equations and (b) dielectrics, modelled using the Lorentz equations.

Figure 2.6(b) shows the frequency response of a dielectric material. The binding of electrons to atoms gives rise to a natural frequency of oscillation ω_0 , which leads to a peak in absorption as energy is efficiently coupled into the crystal lattice. Above ω_0 the electrons can oscillate strongly and the real and imaginary parts of the dielectric constant acquire the same form as for metals, with ϵ_1 going negative. Therefore the dielectric is highly reflective in this frequency region, although absorption significantly reduces the effect. Using the Lorentz and Drude expressions it is possible to calculate the optical properties of many materials. However for many metals, such as silver and gold, the influence of inter-band transitions must also be taken into consideration.

2.6 Real Metals

Despite its applicability to metals such as aluminium, the Drude model does not accurately compute the optical properties of many other metals, including silver and gold. In order to accurately understand the frequency response of these metals, one must consider the influence of bound electrons. Figure 2.7 shows the electron shell configuration of gold. The outermost $6s$ electron is responsible for the free electron sea that gives gold its metallic properties, however the closed $5d$ shell has a very similar energy. Figure 2.7 sketches the electron dispersion near the Fermi energy. This shows the delocalised s -band crossing the Fermi energy, allowing intra-band transitions. Also shown is the localised $5d$ -band, which consists of a number of modes (not shown, see (39) for more details) and represents a large number of bound electron states just below the Fermi energy.

Silver exhibits free-electron type behaviour (as described by the Drude model), but also has a significant bound-electron component(38). The reflectance of silver is shown in figure 2.8(a). The low energy part of the spectrum follows a free-electron type of reflectance, being almost 100% reflective and falling to low values at the plasma frequency ω_p around 3.9 eV. However beyond ω_p the reflectance rises abruptly, before again falling to low values; this behaviour is due to bound electrons. The experimentally determined ϵ_1 is separated into free ϵ_f and bound ϵ_b electron components in figure 2.8(b). The free electron component is obtained from Drude theory with parameters determined from the low

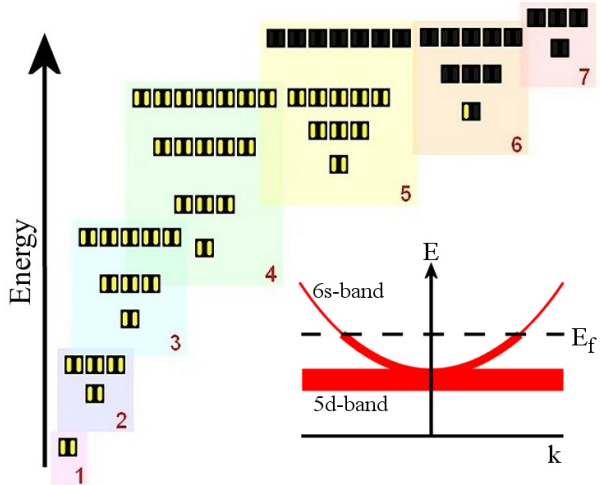


Figure 2.7: Plot depicting the electron shells and energies for a gold atom, filled boxes represent electrons, from (40). Inset sketches electron dispersion for gold, with the outer $6s$ electron delocalising, leading to the conduction band.

frequency limit, the bound contribution is then obtained by subtraction. This result reveals the strong effect of bound charges on the plasma frequency. Using equation 2.14 the plasma frequency is calculated to be 9.2 eV. However, the strong positive contribution from bound charges raises ϵ_1 such that it crosses the $\epsilon_1=0$ axis at 3.9 eV. Above the plasma frequency bound charges contribute a further rise in reflectance, not accounted for in the Drude model. This example clearly reveals how competing bound and free electrons alter the optical properties of metals. For practical purposes, rather than attempting to calculate the precise refractive index of metals, they are measured using ellipsometry. This technique consists of measuring the change in polarisation state of a beam of light when it is reflected from a surface. Since the reflection coefficients are angle dependent, the polarisation components perpendicular and parallel to the plane of incidence can be distinguished. Thus the difference in amplitude and phase between the two polarisation components can be accurately determined, yielding $\hat{\epsilon}$, shown for gold and silver in figure 2.9(41; 42; 43).

If these plots are compared to those of the models in figure 2.6, it can be seen that the dielectric constants and refractive indices follow the trends of a

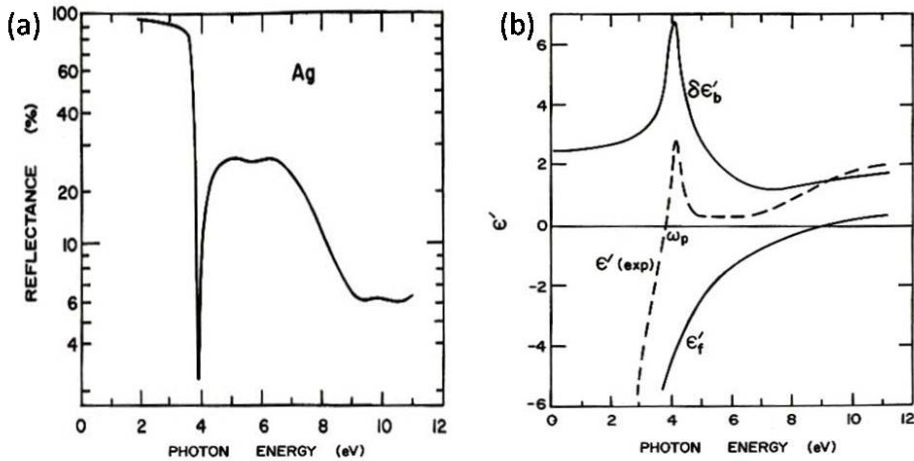


Figure 2.8: (a) Reflectance of silver(44) and (b) separation of the measured ϵ_1 (here $\epsilon'_{(exp)}$) into free ϵ_f and bound ϵ_b electron components(45).

pure metal, decreasing with increasing frequency (the absolute value of the real dielectric constant is shown, hence the positive value). However, around 2.36 eV and 3.8 eV (46) for gold and silver respectively, some rapid variations in the values occur. These correspond to the interactions with bound electrons in the outer shells; this is most notable for silver, where the graphs closely follow the dielectric model in this regime. Also plotted is the reflectivity of these metals. As expected, at low frequencies in the pure metal region of the spectrum 100% reflection is observed. However, as the interactions with the bound electrons become stronger, energy is more efficiently coupled to these oscillating modes, and so the reflectivity drops substantially. For the experiments performed in this thesis the energy of the incident light never exceeds 3 eV, allowing silver to be considered a perfect metal and gold suffering absorption towards the higher frequency end of the spectrum. Therefore for all metals considered in this thesis the experimental values of the real and imaginary dielectric constants are taken from the classic paper published by P. Johnson and R. Christy(42). Using this information, the absorption of light from a metal can be fully calculated. However, experiments which observed the absorption of electrons fired through thin metal films found other sources of absorption not observed optically(47). This marked

the discovery of the *surface* plasmon and the birth of the field of plasmonics.

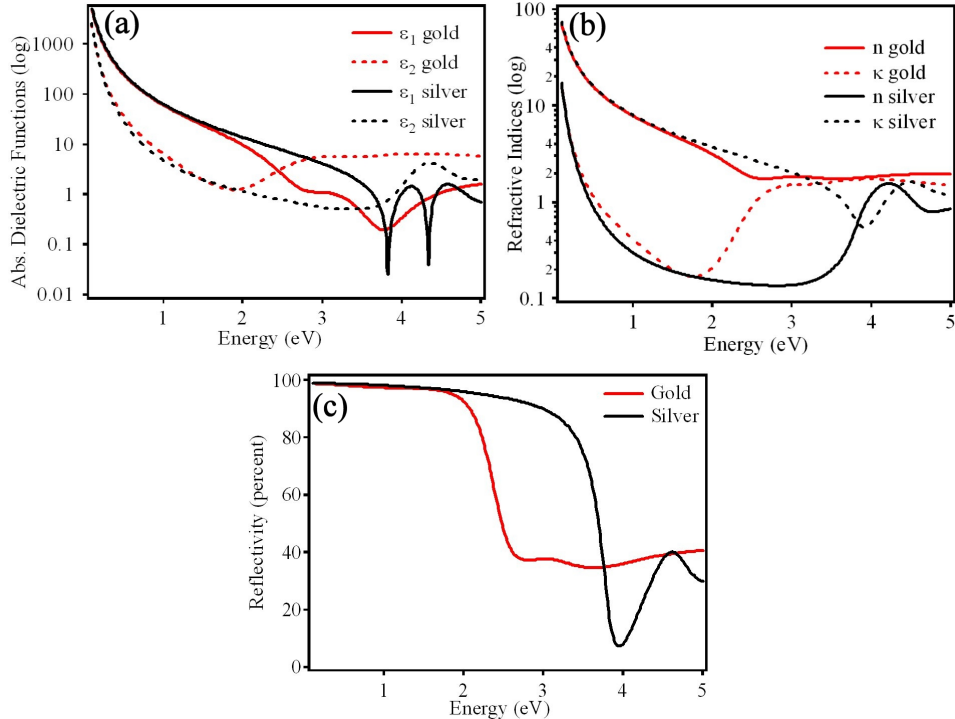


Figure 2.9: Experimentally deduced values for silver and gold of (a) absolute complex dielectric function, (b) complex refractive index and (c) reflectivity.

2.7 Surface Plasmon Polaritons

In the previous section, a plasmon was introduced as a bulk oscillation of the electron cloud within an isotropic infinite conductor. However at a metal/dielectric interface, this picture must break down with the loss of one of the dimensions. By solving Maxwell's equations with the appropriate boundary conditions it is found that surface plasmon waves exist which propagate along the surface of the metal. These waves have frequencies in the range from $\omega = 0$ to $\omega_p/\sqrt{2}$, where $\omega_{spp} = \omega_p/\sqrt{2}$ is defined as the 2D surface plasmon polariton frequency. Hence, surface plasmon waves (commonly called surface plasmon polaritons or *SPPs*)

2.7 Surface Plasmon Polaritons

will be excited at energies *below* that of the bulk plasmon. A schematic of an *SPP* is shown in figure 2.10(a).

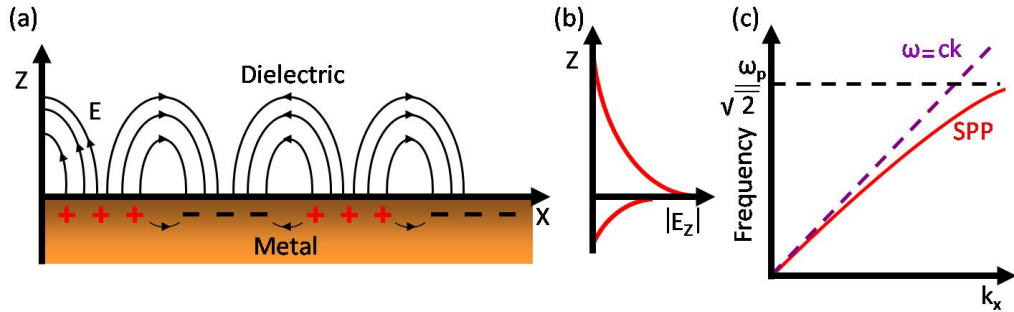


Figure 2.10: The surface plasmon polariton (*SPP*). (a) Schematic of the surface charge and electric field. (b) Electric field distribution perpendicular to the surface. (c) Dispersion relation for a *SPP*, the light line represents the dispersion of light in a vacuum.

The longitudinal surface charge oscillations give rise to an electric field perpendicular to the interface which decays exponentially with distance (figure 2.10(b)). This corresponds to an evanescent field above the surface with a decay length similar to that of the wavelength of light. At the metal, the *SPP* exists as a charge fluctuation which penetrates into the surface a distance equal to the skin depth. If the dielectric constants of the metal and dielectric are taken to be ϵ_m and ϵ_d respectively, then by solving Maxwell's equations for an optical mode at the interface, the *SPP* dispersion relation is found to be(48):

$$\hat{k}_{spp} = \frac{\omega}{c} \left(\frac{\hat{\epsilon}_m \epsilon_d}{\hat{\epsilon}_m + \epsilon_d} \right)^{1/2} \quad (2.15)$$

where for completeness, this equation can be split into real and imaginary components $\hat{k}_{spp} = k'_{spp} + ik''_{spp}$ where:

$$k'_{spp} = \frac{\omega}{c} \left(\frac{\epsilon_m \epsilon_d}{\epsilon_m + \epsilon_d} \right)^{1/2} \quad \text{and} \quad k''_{spp} = \frac{\omega}{c} \left(\frac{\epsilon_m \epsilon_d}{\epsilon_m + \epsilon_d} \right)^{3/2} \frac{\epsilon_m}{2\epsilon_m^2} \quad (2.16)$$

For real k_{spp} solutions, $\epsilon_m < 0$ and $|\epsilon_m| > |\epsilon_d|$ must be satisfied, which is true for metals which have ϵ_m both negative and complex. The *SPP* dispersion

2.7 Surface Plasmon Polaritons

relation $\omega(k_{spp})$ (red line plotted in figure 2.10(c)), shows that for small wave vectors the plasmon is close to that of the light line, but always to the right hand side. Therefore the *SPP* has similar properties to the coupled light field but always has a greater momentum and is non-radiative. This increased momentum is associated with the binding of the mode to the surface. For larger wave vectors the value of ω_{spp} approaches the characteristic 2D bulk surface plasma frequency:

$$\omega_{spp} = \frac{\omega_p}{\sqrt{1 + \epsilon_d}} \quad (2.17)$$

At this frequency, the group velocity $v_g = \partial\omega/\partial k$ equals zero so that the *SPP* resembles a localised 2D fluctuation of the electron plasma. With increasing ϵ_d , the value of ω_{spp} is reduced; an important result exploited to manipulate the energetics of plasmons in later chapters. Again starting from Maxwell's equations, the intensity of a *SPP* propagation along a smooth surface is found to decrease as $\exp\{-2k''_{spp}x\}$. Therefore the decay length L_i after which the intensity decreases to $1/e$ is then given by:

$$L_i = (2k''_{spp})^{-1} = \frac{c}{\omega} \left(\frac{\epsilon_{m1}\epsilon_d}{\epsilon_{m1} + \epsilon_d} \right)^{-3/2} \frac{\epsilon_{m1}^2}{\epsilon_{m2}} \quad (2.18)$$

Perpendicular to the surface the electric field decreases as $\exp\{-|k_{zi}|z|\}$. The value of the (skin) depth at which the field falls to $1/e$ becomes:

$$\hat{z}_d = \frac{\lambda}{2\pi} \left(\frac{\epsilon_{m1} + \epsilon_d}{\epsilon_d^2} \right)^{1/2} \quad \text{and} \quad \hat{z}_m = \frac{\lambda}{2\pi} \left(\frac{\epsilon_{m1} + \epsilon_d}{\epsilon_m^2} \right)^{1/2} \quad (2.19)$$

This set of equations allows the key plasmonic properties of a metal to be quickly calculated from their dielectric function. It is useful to have in mind values for these key plasmonic properties, in particular for the metals most common throughout this thesis.

2.8 Plasmons on Silver, Gold and Aluminium

The majority of structures investigated in this thesis are fabricated from silver, gold or aluminium; metals chosen for their strong plasmonic properties. Using the analytic expressions previously derived and the experimentally tabulated dielectric functions of Johnson and Christy⁽⁴²⁾ it is possible to calculate the full plasmonic properties of these metals. Figure 2.11 shows the calculated plasmonic properties of a plane silver surface. (a) shows the refractive index and (b) dielectric function of silver, markers indicate the frequency of the (black) bulk plasmon at ω_p , and (green) surface plasmon at ω_{spp} . At the bulk plasmon frequency $\epsilon_1 = 0$ and an incident photon will be efficiently coupled into a plasmon oscillation, with damping proportional to ϵ_2 . The surface plasmon dispersion relation is shown in red in (c) with the dispersion curve for light in air ($k_x = \epsilon_d^{1/2} \omega/c$) shown in blue. For photon energies $E < 3.5$ eV a bound surface plasmon (*SPP*) mode is observed, tending to the light line at short wave vectors (defined as $2\pi/\lambda$). For $E > 3.8$ eV a radiative plasmon mode (*RPP*) is observed to the left of the light line, corresponding to wavelengths satisfying the relation $\epsilon_{m2} > |\epsilon_{m1}|$. For energies between the *SPP* and *RPP*, heavily damped quasibound (*QB*) modes with negative phase velocities exist. (d) shows the reflectivity spectrum calculated using the Fresnel equations. Below the plasma frequency the metal efficiently reflects incident light, becoming increasingly transparent around the plasma frequency. (e) shows the electric field penetration into the metal. Below the plasma frequency the field penetration into the air is proportional to the photon wavelength, tending to a minimum at ω_{spp} as the plasmon is tightly bound to the metal surface. At ω_p the field penetration into the metal is a maximum. Away from this frequency range, penetration into the metal is limited to the skin depth of silver. (f) shows the plasmon propagation length. At the important telecommunications wavelength of 1550 nm, the propagation length approaches 400 μm , whereas at 500 nm the propagation length is limited to around 30 μm . Therefore large surface plasmon wavevectors (corresponding to short plasmon wavelengths) can be achieved but at the expense of propagation distance.

The plasmonic properties of silver are contrasted with those of gold and aluminium in figure 2.12, calculated using the measured optical constants of Johnson

2.8 Plasmons on Silver, Gold and Aluminium

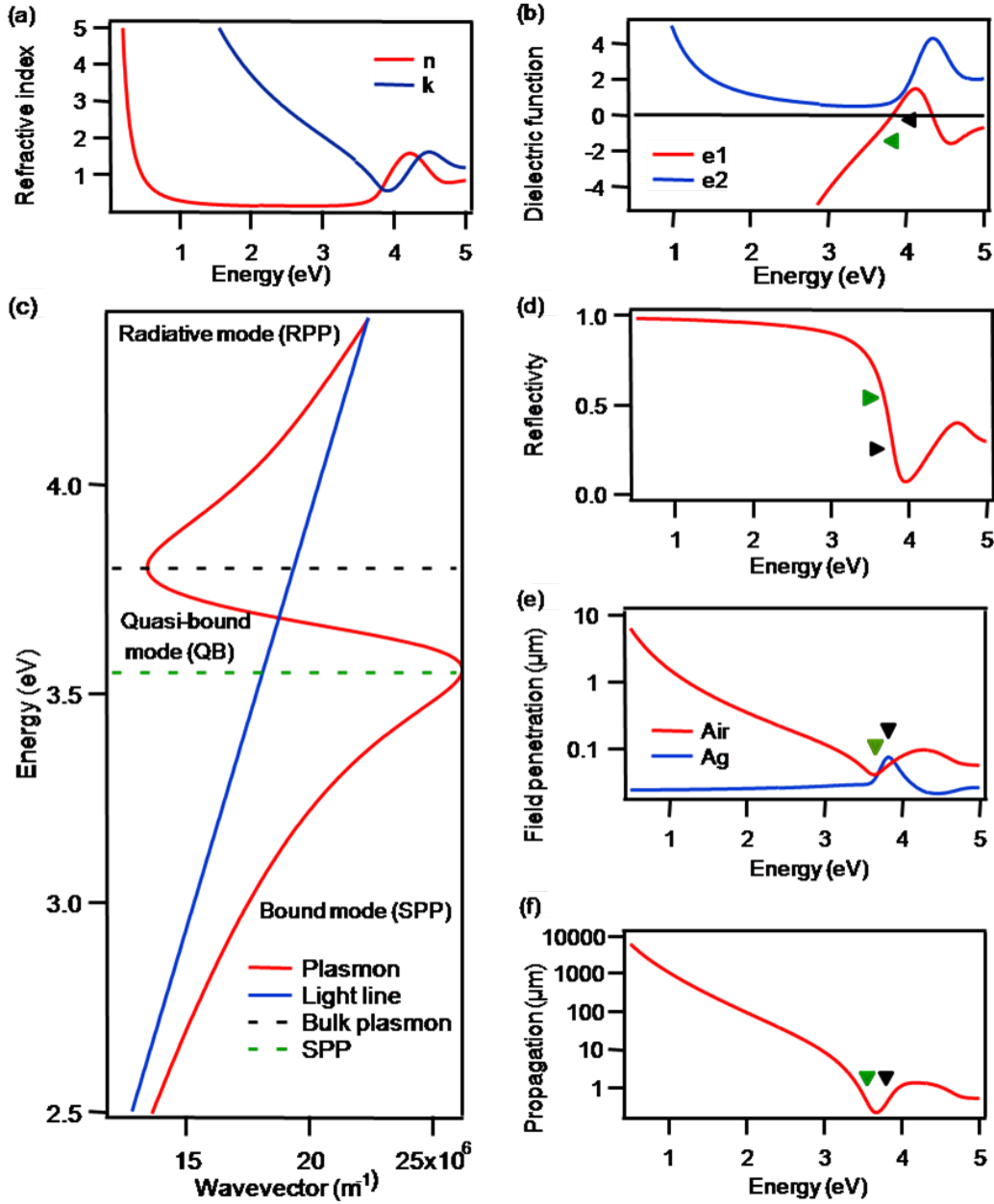


Figure 2.11: The plasmonic properties of silver calculated using experimentally tabulated values of the dielectric function. (a) the refractive index, (b) dielectric function, (c) plasmon dispersion, (d) reflectivity, (e) electric field penetration and (f) plasmon propagation length. Arrows mark the wavelength of the (black) bulk plasmon (ω_p) and (green) surface plasmon (ω_{spp}).

2.8 Plasmons on Silver, Gold and Aluminium

(42) and Palik (49). It is clear that identical structures fabricated from these three metals will have very different plasmonic properties. Therefore by selecting the appropriate metal, structures can be designed for resonances at specific wavelengths. The nanovoid samples presented in this thesis have been fabricated in gold and silver for plasmonic resonances optimised in the red and blue wavelength ranges respectively, and by alloying it is possible to produce structures optimised for resonances at intermediate wavelengths.

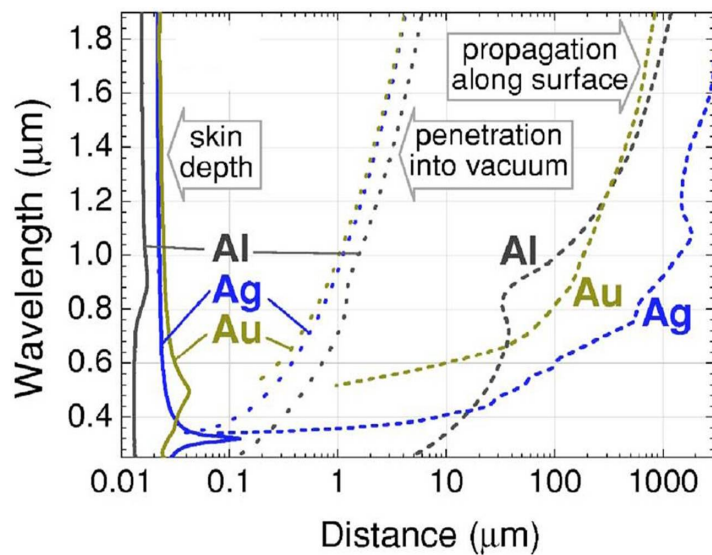


Figure 2.12: Extension of the plasmon field into the metal skin depth, into the vacuum, and along the surface propagation distance for silver, gold and aluminium(50).

2.9 Grating Coupling to Surface Plasmons

Since *SPPs* do not directly couple to an optical field (due to the momentum mismatch) they must be created via some intermediate step(9; 51). This requires either converting the incident light into an evanescent mode by means of total internal reflection, or by scattering the light to higher momentum via a grating or scattering site. A prism coupling method has been used extensively when studying the properties of *SPPs* on plane surfaces(51). In this technique, light is totally internally reflected from the base of a glass prism, which is positioned within several hundred nanometres of a metal surface. Due to the higher refractive index of the glass, the momentum matching condition is satisfied and light can tunnel through the air gap to excite a *SPP*(48). Using this technique, many of the properties of *SPPs* have been experimentally characterised, such as decay length and the interaction between plasmon modes on either side of a thin metal film(52; 53). However this technique is limited to a very precise geometry and does not produce some of the interesting features found when a grating is used as the coupling mechanism.

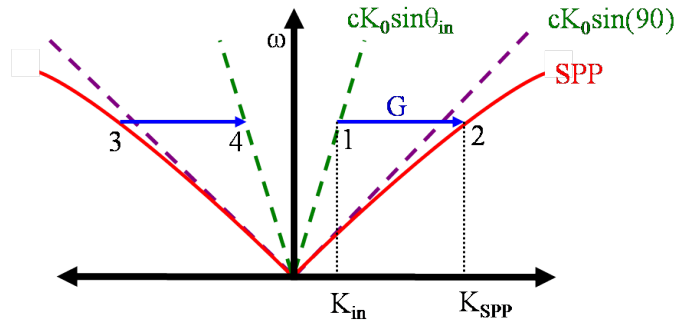


Figure 2.13: Incoming light has a wavevector of $k_0 \sin \theta_0$. At 1 the photon is given momentum G and transformed to k_{spp} at 2. The reverse process occurs at 3 and k_{spp} decays to light at 4 via G .

Grating coupling allows direct excitation of *SPPs* and places fewer limitations on the experimental conditions. The gratings used to couple light to *SPPs* typically have structural features on the size scale of the incident light. A periodic

2.9 Grating Coupling to Surface Plasmons

corrugation, such as that of a diffraction grating or periodic array of nanovoids, will scatter a photon of wavevector $k_0 = \omega/c$, incident at an angle θ_0 , imparting momentum, nG , where $G = 2\pi/a$ is the grating wavevector, a is the period of the grating and n is an integer. By conservation of momentum:

$$k_{spp} = k_0 \sin \theta_0 \pm nG \quad (2.20)$$

Therefore tuning of θ_0 and a allows direct coupling to an *SPP* mode. The periodicity of the surface allows the reverse process and the coupling of non-radiative *SPPs* back to free space photons, illustrated in figure 2.13. Because of the similarities between the optical and plasmonic descriptions, propagating *SPP* modes will be referred to as Bragg modes in later chapters.

Chapter 3

Sample Production and Analysis

Most of the samples studied in this thesis were produced by Sumeet Mahajan using a two-stage process developed at the University of Southampton. First, latex spheres are self-assembled into a close-packed array on a conducting substrate. Metal is then electroplated through the template to form a nano-structured surface. This simple approach produces complex nano-structures that support a wealth of plasmonic properties. Furthermore, the technique is quick, cheap and scalable for possible mass production. This chapter will give a brief overview of sample fabrication, then outline the analysis techniques used to characterise the properties of nanovoid samples.

3.1 Sample Preparation

This section describes the techniques used to produce templates of self-assembled sub-micron polystyrene spheres. The electrochemical deposition procedure used to invert the template into a structured metal surface is then discussed.

3.1.1 Template Preparation

The first stage in the fabrication procedure is the self-assembly of polystyrene spheres which form the template used for electrodeposition. The procedure has been optimised to produce large monolayer domains of close packed spheres([54](#)). Mono-dispersed polystyrene spheres (Duke Scientific Corporation) are purchased

3.1 Sample Preparation

as a 1 wt.% solution in water. The latex spheres are slightly negatively charged and do not aggregate when in solution. Sphere sizes between 350 nm and 2 μm have been used with a typical variation in diameter of 1%. Initial work in this field used a technique of sedimentation to deposit the spheres onto a substrate(55). Whilst this approach produced results(56; 57), the templates were comprised of varying layers of spheres and large numbers of defect sites, making the optical features complex and quantitative analysis difficult. An alternative method using capillary forces was subsequently developed, allowing far greater control over the assembly process(54). This allowed the formation of a monolayer of well ordered spheres, greatly simplifying the surface geometry and allowing easier analysis of data.

Typical templates are produced using the method depicted in figure 3.1. Substrates are made of 200 nm of gold evaporated on a glass side coated with 10 nm of chromium. These substrates are extensively cleaned by sonication in isopropanol, followed by a deionised water rinse and dried using argon. All solvents used are of reagent grade quality and obtained from Aldrich. Substrates are subsequently immersed in an ethanolic solution of cysteamine for three days, allowing a monolayer of cysteamine to assemble onto the surface. This cysteamine layer is more hydrophilic than gold and so reduces the contact angle of aqueous solutions on the substrate, aiding the final template production.

The substrate, along with a clean cover slip, is then made to form a small fluid cell by means of a thin layer of Parafilm (Pechiney Plastic Packaging, Inc). This cell has a thickness of around 100 μm and an area of 1 cm^2 . Held vertically, the aqueous sphere solution is added, and the cell is placed in an incubator at 15° C. Evaporation of the solution can only occur at the top edge of the cell, and here the cysteamine forces the water into a thin layer. As the solution evaporates, the sweeping meniscus tail draws spheres out of the solution. As the solution level falls below the sphere diameter, capillary forces build up between spheres, causing them to deposit and order on the flat surface. Since deposition only occurs at the meniscus edge and the rate of deposition can be controlled by the evaporation rate, the seeding of a single domain becomes highly probable. Typical domain sizes are 100 μm^2 , allowing imaging of single domains using a microscope at $\times 10$ magnification. Subsequent spheres will add to the initial domain and, if the sphere

3.1 Sample Preparation

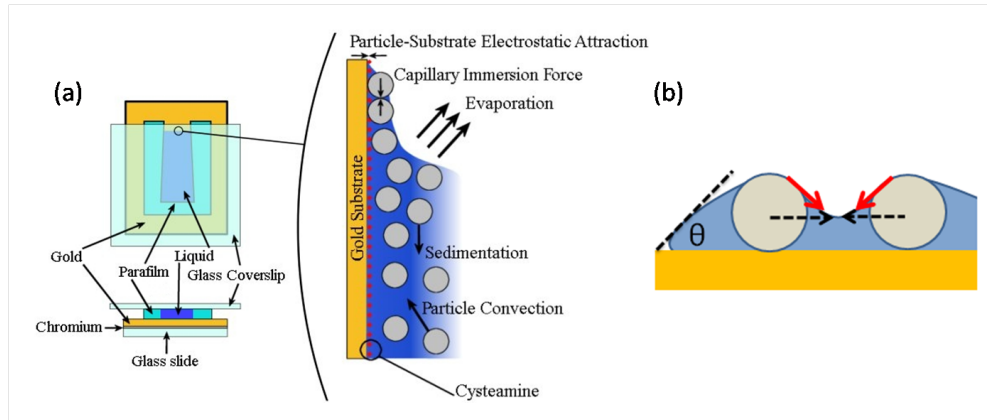


Figure 3.1: (a) (Left) Cell used for template deposition. (Right) Schematic of the meniscus edge at the top of the cell. Spheres are drawn out of solution by the meniscus tail and forced into a close packed domain by the surface tension between spheres(1). (b) Strong capillary forces which develop at the meniscus between the solution and substrate and between adjacent spheres assemble the spheres into a close packed array.

concentration is carefully controlled, the entire surface will form a single ordered close packed structure. The meniscus tail also prohibits the formation of a second layer of spheres, keeping the geometry of the system to the simplest case, that of a monolayer. Figure 3.2 shows a scanning electron microscope (*SEM*) image of a typical region of a template. The template forms a single, monolayer domain of close-packed, touching spheres. The spheres are resistant to re-suspension when, in the next production step, the sample is lowered into an electrochemical plating solution.

3.1.2 Electrochemical Deposition

Electrochemical deposition is performed using a three-electrode arrangement, depicted in figure 3.3(a). The sample on which the metal is to be grown forms the working electrode. The counter electrode supplies the charge to complete the circuit while the reference electrode is used to control the potential applied to the working electrode. A commercial plating solution (Technic Inc), containing

3.1 Sample Preparation

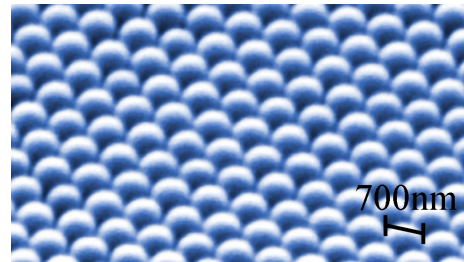


Figure 3.2: SEM image of a template made from 700 nm spheres(1).

gold ions, forms the connection between the electrodes. For the sake of simplicity, the plating of gold will be specifically described here, other metals follow very similar lines, using different solutions and voltages. Figure 3.3(b) shows the time dependence of the charge when plating through a micro-sphere template, where throughout plating the voltage is kept constant.

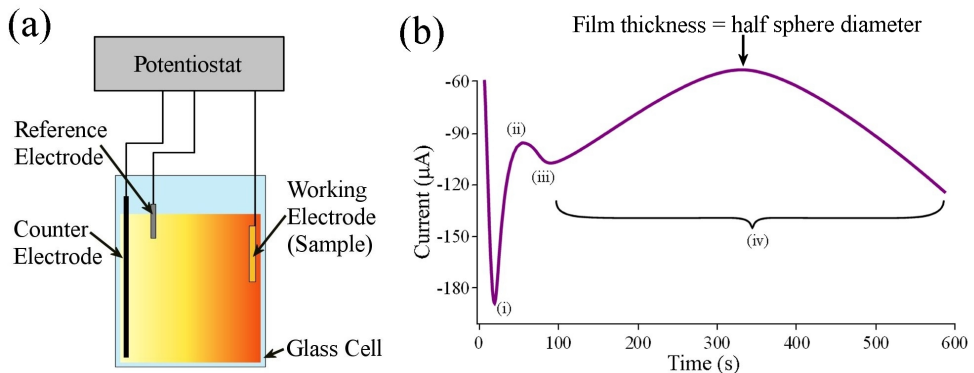


Figure 3.3: (a) Electrochemical deposition setup. (b) Current vs. time for the deposition of gold through a close packed sphere template, initially a voltage is applied that causes a capacitive effect in the cell (i), then gold will begin to deposit (ii) until a steady deposition rate is reached (iii). The changing area of deposition through the template causes a change in current (iv)(1).

At time $t = 0$ a voltage is applied through the cell and the working electrode becomes negatively charged. Positive ions in the solution are drawn towards the negative electrode, while negative ions accumulate near the positive one;

3.1 Sample Preparation

this effect gives rise to a current (point i), which quickly returns to zero. The voltage in the cell is sufficient for gold ions to overcome the Coulomb potential and undergo the reaction: $Au^+ + e^- \rightarrow Au$. First, the nucleation of single gold atoms occurs, then the formation of islands as more gold is deposited (point ii) and finally, the formation of a gold film. The speed of growth is now limited by the rate at which gold atoms can diffuse out of solution and into the plating region. This steady state is determined by the diffusion-limited current (reached at point iii). By monitoring the charge passed in region (iv) the thickness of the deposited film can be calculated. When producing a nano-structured film the growth occurs through the sphere template, causing a modulation in the growth area and a corresponding variation in charge. The peak, corresponding to a charge minimum, in region (iv) corresponds to a thickness equal to the radius of the spheres, where the deposition area is a minimum.

To grade the thickness of a deposited layer the sample is mounted on a micrometer stage, allowing the systematic retraction of the surface out of the plating bath. At every step the new plating area is measured, allowing the absolute thickness of each deposited step to be calculated. After deposition the samples are washed in tetrahydrofuran for two hours to completely remove the spheres, leaving a free-standing array of nano-voids, shown in figure 3.4.

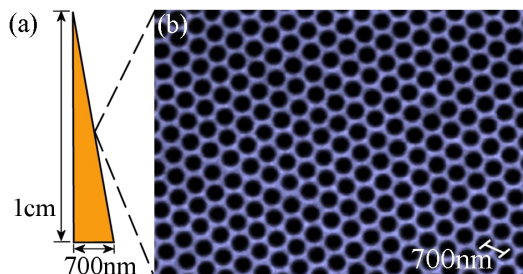


Figure 3.4: (a) Schematic of a graded thickness sample. (b) *SEM* image of a nanostructured gold film fabricated by templating with 700 nm diameter spheres(1).

Using this technique samples graded from zero to the sphere diameter can be reliably produced. To date, samples made from gold, silver, nickel, platinum,

3.2 Sample Characterisation

palladium, copper and poly-pyrole have been produced. The versatility of this technique also allows the production of more complex structures.

3.2 Sample Characterisation

After production, samples undergo a rigorous set of analysis experiments. Some of these characterisation methods are applied to all samples to understand the morphology over the film. Other tests are conducted to understand specific sample properties, the results of which can be used to understand other experimental details. The biggest challenge facing this process is finding the precise structural geometry at the different thicknesses across different samples. This information is crucial to accurately compare and correlate the complex optical spectra presented in later chapters, hence each characterisation method has been used to try to gain more information to fulfil this goal.

3.2.1 SEM Characterisation

Imaging using a LEO 1550VP Field Emission *SEM* provides information about the short-range order and crystalline structure of the films, along with information about the approximate film thickness by measuring pore mouth diameter as defined in figure 3.5 and using the equation:

$$\bar{t} = \frac{r_{void} \pm \sqrt{(r_{void}^2 - r_{pore}^2)}}{2r_{void}} \quad (3.1)$$

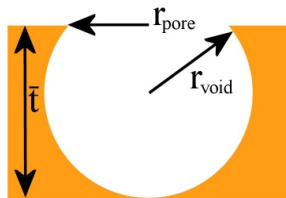


Figure 3.5: Definition of normalised thickness \bar{t} = thickness/diameter along with other parameters required to calculate the film thickness from *SEM* images.

3.2 Sample Characterisation

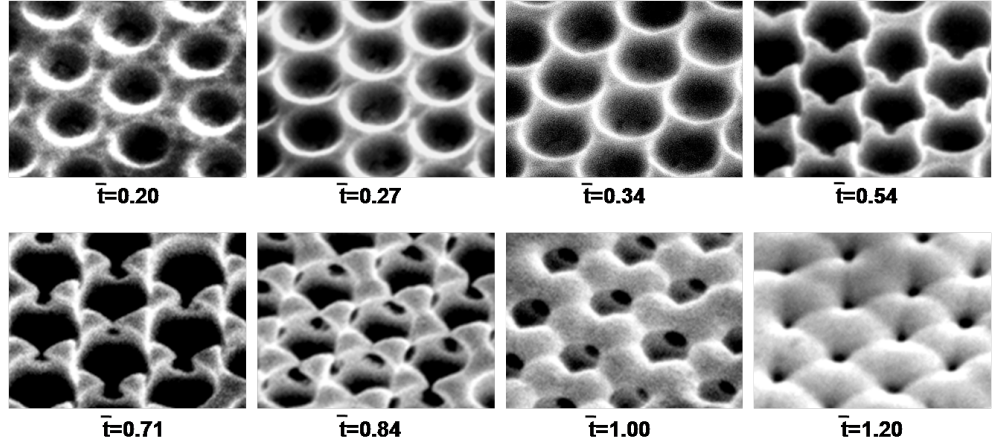


Figure 3.6: (Top) *SEM* images of a 600 nm nanostructured surface with increasing normalised thicknesses.

Here, the normalised thickness, $\bar{t} = \text{thickness}/\text{diameter}$, is defined, and will be consistently used throughout the rest of this thesis to define sample thickness. *SEM* images of eight different thicknesses are shown in figure 3.6. Using equation 3.1 it is possible to calculate approximate thicknesses for each of these positions. This image highlights the variation in surface geometry with changing thickness. When thin, the sample consists of an array of well-spaced shallow dishes, with a smooth top surface. Near half void height, $\bar{t} = 0.54$, the cavities are separated by triangular pillars and touch the neighbouring six dishes in between these spikes. Above $\bar{t} = 0.54$, the metal is forced to grow out from these islands over the non-conducting spheres, leading to increased roughness and less efficient growth. In this thick regime the cavities start to resemble spherical cavities, and at $\bar{t} = 1.2$ become almost completely encapsulated.

3.2.2 (Quick) Optical Analysis

With a full understanding of the structural properties of a sample, it is useful to perform a quick optical experiment to find the fundamental absorption features present. This optical characterisation gives direct information about the thickness and ordering of a sample, as well as an indication of the overall appearance.

3.2 Sample Characterisation

Samples are viewed using an Olympus BX51 optical microscope with an objective of $NA = 0.25$ collecting over a range of angles θ from 0 to 15° . A collection fibre feeds into a Ocean Optics 2000 visible spectrometer. At $\times 10$ magnification the collection spot size is $6\mu\text{m}^2$, allowing spectra to be recorded from single crystal domains. The first step is to find the best longitudinal sample position to perform reflectivity experiments down the thickness gradation, shown in figure 3.7(a). This is required to avoid intrinsic scratches and blemishes found on some samples. Images and spectra are then taken along this line to form a data set such as the one shown in figure 3.7(b,c).

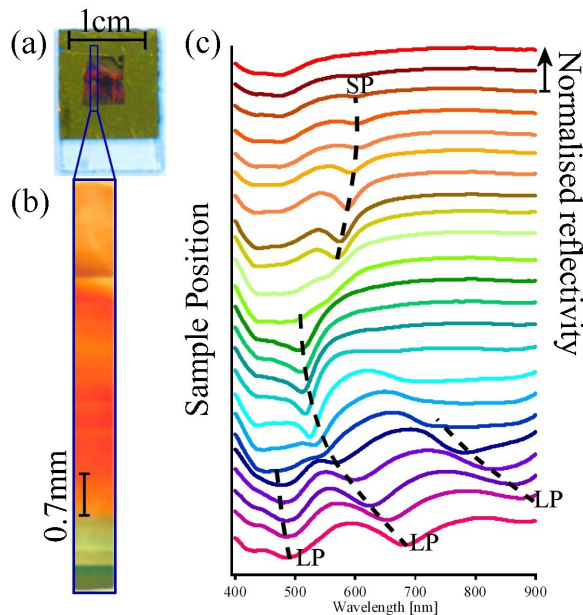


Figure 3.7: (a) Photograph of a sample made from 600 nm voids, graded from $\bar{t} = 0$ to 0.8, and (b) $\times 10$ optical image of the surface from top to bottom. (c) Normalised spectra taken at regular intervals down the same line of the sample, absorption by surface plasmon (*SP*) and localised plasmon (*LP*) modes is identified by comparison with angle resolved plots.

The clear variation in colour of the optical image shows the varying absorption of the sample at different thicknesses, while the purity of the colour also indicates that the sample is well ordered and smoothly templated. This image is also

3.3 Conclusions

useful in showing the top and bottom points of the line over which all subsequent data will be taken, allowing well-correlated data on samples where variations are inherent. The set of normal incidence, un-polarised reflection spectra are normalised to the reflection off a silver mirror and show the fundamental features of the sample: at the top, a sharp surface plasmon absorption dip is visible, while broader localised plasmon absorption dips are apparent over the bottom half of the sample. Using this data, it is easy to select samples that absorb well at different wavelengths for experiments where these resonances play a fundamental role.

3.3 Conclusions

The process of self-assembly and electroplating has been shown to be a powerful means of producing nano-structured surfaces both quickly and incredibly cheaply. Analysis has shown that the samples are well ordered and that excellent control and understanding of the surface geometry has been achieved. Samples can be made from a wide variety of materials, providing the means to produce an almost limitless variety of structures. Having introduced the sample properties, the way is paved to begin to understand the complex and varied optical response of these nano-structured metals. However, first a discussion into the experimental setup will be presented.

Chapter 4

Experimental Setup

The detailed optical experiments performed in this thesis use a computer controlled goniometer. The data produced is quite substantial, so this chapter will provide an explanation into the different imaging techniques applied to the data in the forthcoming chapters, as well as a discussion into the experimental setup.

4.1 Experimental Setup

Much of the work undertaken to date has been performed using a computer-controlled goniometer, assembled by Tim Kelf at the University of Southampton and programmed using the Igor computer language by the author at the University of Cambridge. For the reflectivity experiments exploring surface plasmons on nanovoids, a super-continuum white-light laser performs the job of illumination. The full setup is shown in figure 4.1. A passively mode locked, 1064 nm, 1 ns, microchip laser (JDS Uniphase) is focused into a holey fibre (Blaze Photonics). The fibre has a very small core and is designed to have zero dispersion at the pump wavelength as well as being single mode for all guided frequencies. The high confinement in the fibre core leads to strong non-linear effects, which for this particular fibre the most important of these is four-wave mixing. As the light travels through the fibre this mixing process efficiently broadens the spectra of the pump laser, after 20 meters the emerging light is well collimated and has an optical spectrum from 480 nm up to at least 2 μm . The spectral characteristics are stable over time scales of months for both intensity and shape.

4.1 Experimental Setup

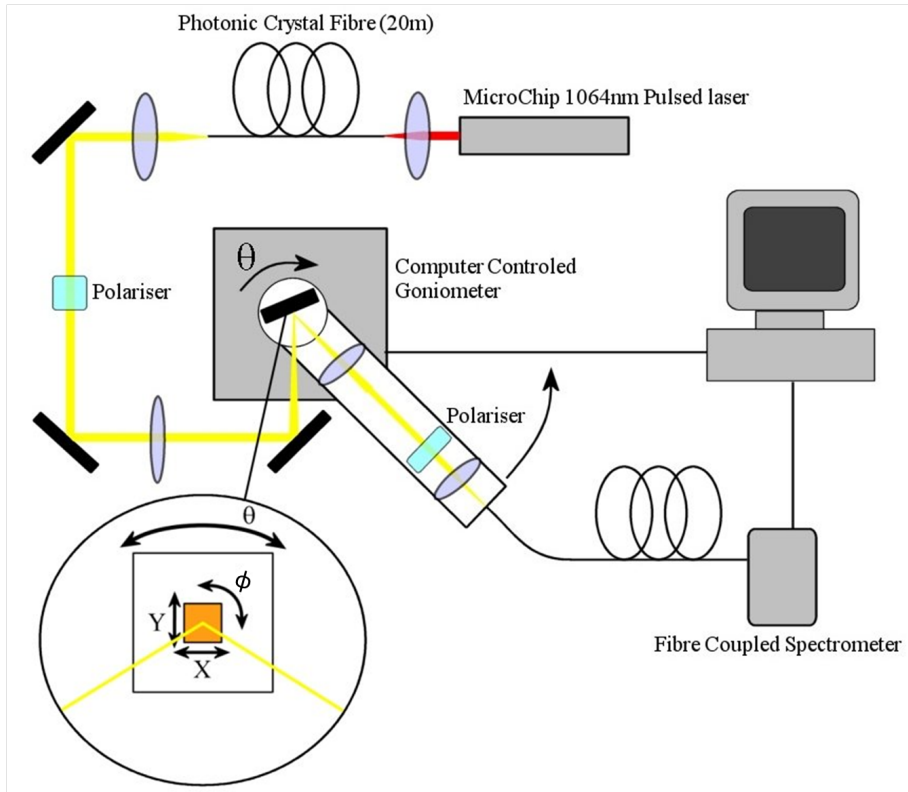


Figure 4.1: Experimental setup for measuring the angle resolved reflectivity of nanovoid samples. Inset shows definitions for θ - incident angle, ϕ - sample orientation, and X/Y movement directions(1).

The polarisation of the white-light laser beam can be selected before the beam is guided onto a sample. The sample can be moved in both in-plane directions (X and Y) as well as rotated in the θ/ϕ directions, as defined in figure 4.1. This requires the laser beam to be incident on the sample at the centre of both planes of rotation as well as the sample being precisely aligned in the same planes. This requires a high degree of precision to ensure the reflected laser beam will then always precisely land on the opening of an optical fibre attached to the collection arm. The spot size imaged onto the sample has an area of $250\mu\text{m}^2$, and collected spectra therefore represent an average over several crystal domains. The goniometer has no limit to the positive angles it can record, however the geometry enforces a limit on the negative angles possible. All sample movements,

as well as the arm, are computer controlled. A split collection fibre feeds into an Ocean Optics 2000 and an NIR optical spectrometer, providing an effective spectral range from 340 nm - 2000 nm, resolution 0.3 nm. The spectrometers are also directly connected into the software written to control the goniometer. The whole system can therefore be programmed to record the reflectivity of the sample at different positions and for both rotations of θ and ϕ , over the complete visible and *NIR* spectrum. This data is subsequently normalised to the reflectivity of an aluminium mirror and compiled into a four dimensional matrix, $R(\text{position}, \theta, \phi, \lambda)$. The setup takes a spectrum of aluminium for each different recorded angle to remove any reflectivity effects associated with angle and polarisation. Finally, cuts are taken to present various aspects of the data.

4.2 Data Presentation

To gain a clear understanding into the plasmonic activity on the nanovoid samples, two different types of data plot are utilised. These show different aspects of the whole data set and are shown in figure 4.2 together with the aspect of the data set they represent.

Dispersion plots (figure 4.2(b)) display the energy of the reflected light vs. the angle of the incident light. These images form a figure analogous to the dispersion plots used for photonic crystals. The only difference here is that the bottom axis is the angle of the input light, not the k -vector of the dispersion bands, although these are related by $k_{\parallel} = \frac{2\pi}{\lambda} \sin \theta$. Dispersion plots start at normal incidence ($\theta = 0^\circ$), then scan out to a certain incident angle, ideally beyond the Brillouin zone. These plots are extremely useful as they provide information about the dispersion of different features, and for this reason they are the most widely used in this thesis. Dispersion plots are at a single position and are presented in a colour scheme where dark blue represents negligible absorption, going through green to red, with white representing maximum absorption. Dispersion plots mainly map out energy vs. incident angle at a single sample orientation ϕ . However, by overlaying the theoretical dispersion of the delocalised features, the exact sample orientation ϕ with respect to the crystal lattice can be calculated for every sample position, allowing accurate comparisons between different positions on a sample.

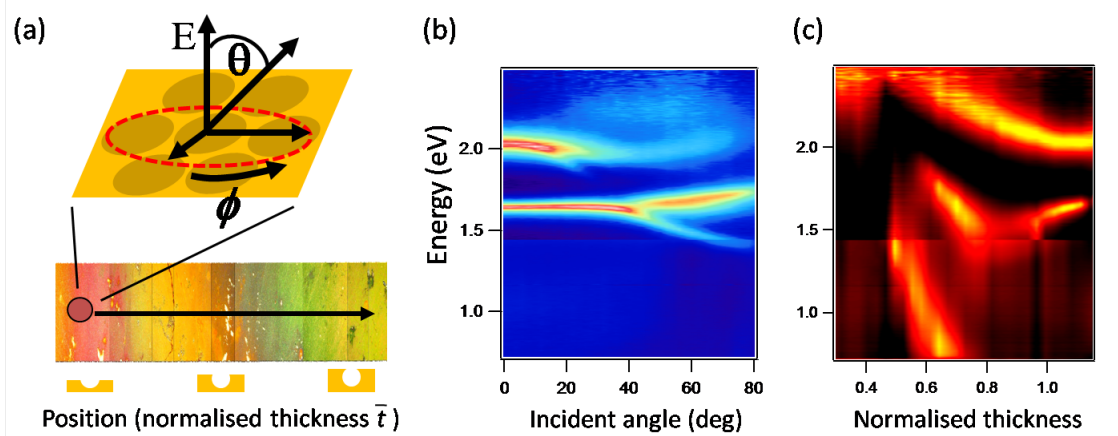


Figure 4.2: (a) Schematic representation of the four-dimensional data set produced by the reflectivity setup. (b) Dispersion plot, energy of reflected light vs. incident angle θ for a single \bar{t} . (c) Position map, plotting energy of reflected light at $\theta/\phi = 0^\circ$ vs. sample position, and hence geometry.

The second graph type is the position map, shown in figure 4.2(c). As the name suggests, this shows how, for a single sample orientation ϕ and incident angle θ , the position of the sample - and hence the sample geometry - affects the energy of different modes. The position map plot is much like the stacked spectra taken using a microscope, but can be viewed at different θ and ϕ , or summed over a range of θ for direct comparison with spectra recorded using a microscope. The most practical use of the position map is when comparing different samples, but it is also good for providing intuitive information on the observed plasmon modes. The information provided by the position map is coloured from black (negligible absorption) to yellow (maximum absorption).

Between these two image types, nearly all the required optical information about the samples can be obtained.

Chapter 5

Types of Plasmon

5.1 Introduction

Using the experimental setup shown in the previous chapter, the reflectivity of many different nano-structured substrates has been recorded. Understanding the range of plasmon modes and their energies gives an insight into how to optimally structure surfaces for particular applications. Whilst in practice it is often impossible to separate out and definitively categorise the observed plasmons (and calculations cannot yet describe arrays of voids), several categories of plasmon have been defined to aid the interpretation of complex reflectivity data. The first type of plasmons are delocalised Bragg plasmons, so called due to their coupling via Bragg scattering. The second type are void or Mie plasmons, which are localised within the truncated spherical geometry and have electric field distributions closely related to those of Mie scattering. Thirdly, are tip or rim plasmons, which are localised at the sharp cavity openings and triangular wedge features. This chapter presents each of these plasmon types individually with a discussion of the models used to understand them.

5.2 Bragg Plasmons

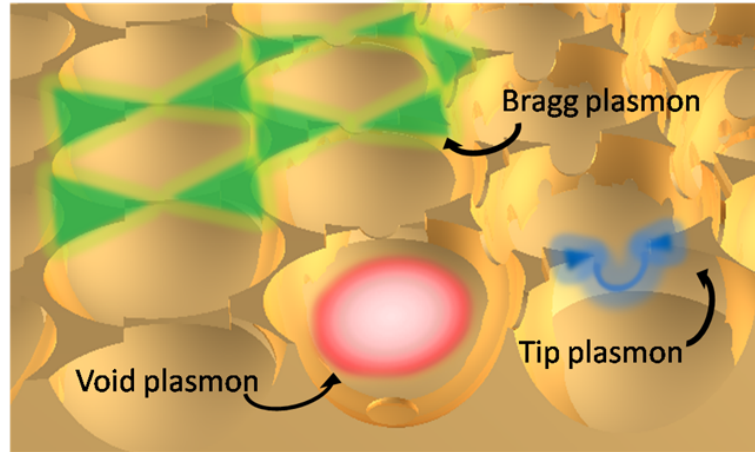


Figure 5.1: Pictorial representation of Bragg, void and tip plasmons on the nanovoid surfaces.

The plasmon modes of nanovoids are strongly influenced by the structure geometry, as described by the normalised sample film thickness \bar{t} defined in section 3.2.1. For sample regions where $\bar{t} < 0.3$ the nanovoid surfaces take the form of a thin two-dimensional grating. Propagating surface plasmons (*SPPs*) exist on the sample top surface and have energies that depend strongly on both incident angle θ and sample orientation ϕ , the dispersion of which fit well to a weak scattering approximation. This model assumes the surface to be flat with point scatterers of a certain periodicity in a hexagonal lattice. In this 2D array, two lattice vectors, **a** and **b**, parameterise the scattering sites. These vectors are orientated at 60° to one another and have a magnitude equal to the centre to centre spacing of the dishes. Under ideal sample growing conditions this periodicity would be equal to the void diameter, however due to the templating process the actual domain pitch is found to be 50 nm greater than the diameter of the voids. The close packed nature of the surface leads to diffraction from the planes of scatters, which are spaced by a distance $\Lambda = \sqrt{\frac{3}{4}}(m\mathbf{a} + n\mathbf{b})$, where m and n are integers. The weak scattering approximation with the energy of a surface plasmon mode, $E(\theta, \phi)$, is given by:

$$E(\theta, \phi) = \hbar c \sqrt{\epsilon_m^{-1}(E) + \epsilon_d^{-1}} \cdot f(\phi) \cdot |\mathbf{k}_{mn} + \mathbf{q}_{mn}| \quad (5.1)$$

where \mathbf{k}_{mn} is the in plane wavevector of the incident light, $\mathbf{q}_{mn} = 2\pi/\Lambda_{mn}$, ϵ_d is the dielectric constant of the region above the surface and $\epsilon_m(E)$ is the energy-dependent complex dielectric constant of gold(42). Finally $f(\phi)$ is a function which accounts for the dependence in sample orientation of the incoming beam on the six-fold symmetric surface(58). The solutions to equation 5.1 represent all allowed plasmon modes which can be coupled from the incident beam \mathbf{k}_{mn} , giving at any wavelength a maximum of six solutions for each band. This compares to diffraction where light of *any* wavelength shorter than $|\Lambda|$ can be diffracted from the surface. Thus there will be a reduction in reflection as diffraction turns on for $\lambda < |\Lambda|$. It is found that the redistribution of light into the diffracted orders is around 100 times weaker than the absorption from the surface plasmon modes and hence the diffracted features are not visible in the data. This is due to the low aspect ratio of the surface morphology reducing the overall diffraction efficiency, and is a general result on all samples studied. Hence the effect of diffraction can be neglected throughout the remainder of this thesis.

The wavevectors of Bragg plasmons (red) excited by the coupling between the smallest reciprocal lattice vectors \mathbf{q}_{mn} for in-plane components of incident light with $\phi = 0^\circ$ and 30° are shown in figure 5.2(a,b). This leads to theoretical Bragg plasmon dispersions as a function of incident angle calculated by equation 5.1 and plotted in figure 5.2(c,d). Each band labelled with \mathbf{q}_{mn} corresponds to a plasmon band coupled by a reciprocal vector \mathbf{q}_{mn} in figure 5.2(a,b). Plasmons propagating in different directions have different energies at the same incident angle in these dispersion relations even though the *SPP* dispersion is isotropic, due to the overlap of the plasmon fields with the surface geometry. Generally, Bragg plasmons are excited in six in-plane directions at six different energies if unpolarised light is incident on the sample. However, degeneracies at symmetry orientations of $\phi = 0^\circ$ and 30° reduce the number of modes to 4 and 3 respectively (as apparent in figure 5.2(c,d)). In addition, observation of Bragg plasmon modes depends on the polarisation of the incident light because *SPPs* are allowed only in *TM* polarisation on flat surfaces. This results in different coupling efficiencies

5.2 Bragg Plasmons

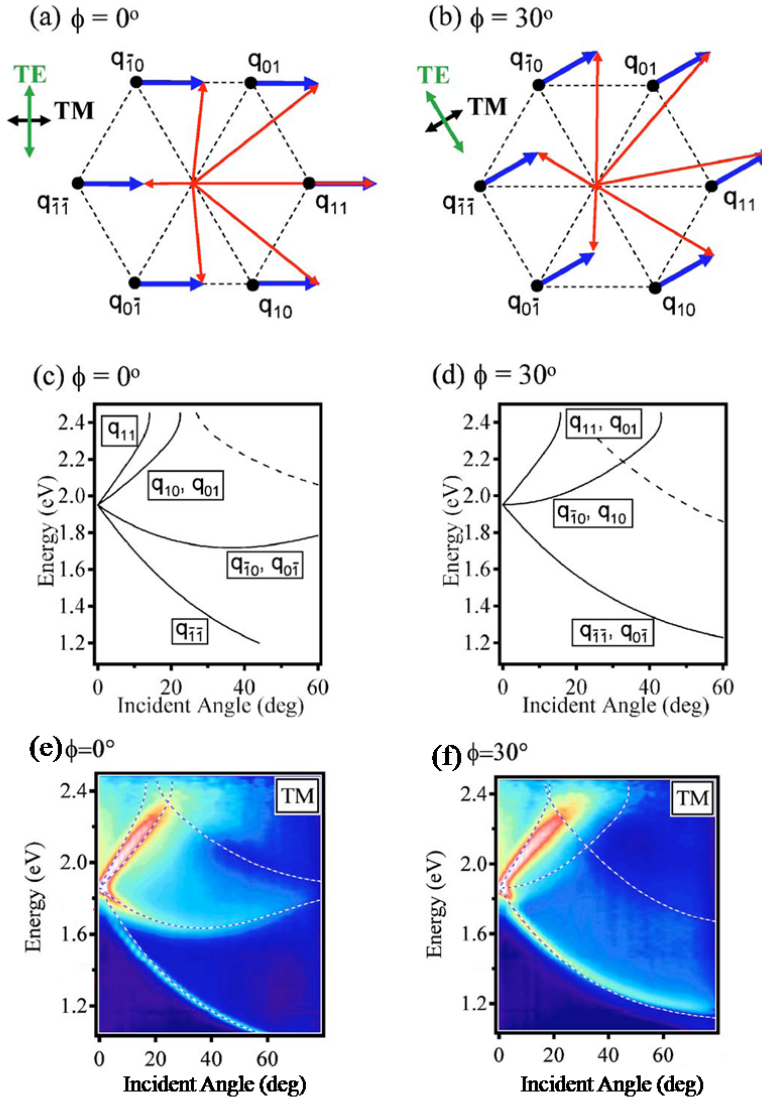


Figure 5.2: Bragg plasmons excited by the coupling to smallest reciprocal lattice vectors \mathbf{q}_{mn} for in-plane components of incident light with $\phi = 0^\circ$ and 30° (2). (a, b) Wavevectors of Bragg plasmons (red) coupled by incident in-plane \mathbf{k}_{mn} (blue). (c, d) Theoretical Bragg plasmon energies as a function of incident angle calculated from equation 5.1 for void separation of 700 nm. The broken lines show plasmon bands excited by the next-nearest wavevectors. Experimental reflectivity of a surface with void diameter 700 nm at a thickness of $\bar{t} = 0.29$ for ϕ (e) 0° and (f) 30° .

5.2 Bragg Plasmons

for different incident light polarisations and plasmon directions. This model can be superimposed on experimental data of angle-resolved reflectivity on a sample with void diameters of 700 nm, and thickness $\bar{t} = 0.29$, shown in figure 5.2(e,f). The broken lines show the predictions from equation 5.1 of the *SPP* dispersion. It is thus possible to clearly identify and characterise the Bragg plasmon modes.

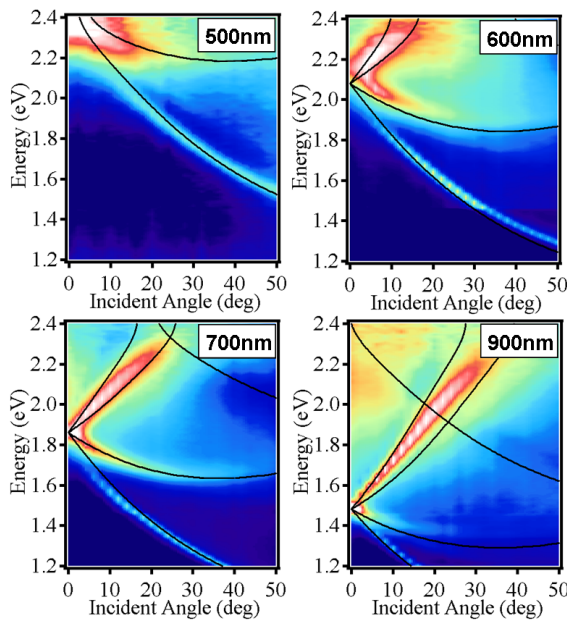


Figure 5.3: Dispersion plots at $\bar{t} = 0.1$ and $\phi = 0^\circ$ for samples with void diameters 500, 600, 700 and 900 nm (1). Lines show theory for Bragg plasmons.

By selecting spheres of different sizes to form the initial template, it is straightforward to change the pitch of the final nanovoid surface. This can be used to tune the *SPP* dispersion across the entire visible and infrared spectrum. The dispersions of four different samples with void diameters between 500 and 900 nm at $\bar{t} = 0.1$ are shown in figure 5.3. The predicted dispersion is overlaid on the data, and again shows a strong agreement between theory and experiment. For each sample the precise pitch is ascertained through *SEM* analysis, and this corrected pitch is used for the theory lines. Similar observations on arrays of square-symmetry pyramidal pits with pitches up to $6 \mu\text{m}$ also show corresponding features as well as higher order bands(59).

5.3 Void Plasmons

When the sample thickness approaches $\bar{t} = 1$, the surface structure takes the form of an array of fully encapsulated spherical cavities, shown in figure 5.4(a). Reflectivity measurements (figure 5.4(b)) reveal strong absorption lines in the visible and near-infrared (*NIR*) spectra due to void plasmon modes localized inside the cavities, as well as propagating Bragg plasmon modes on the surface of the structure. Before presenting the electromagnetic modes of truncated cavities it is useful to introduce the modes within *completely* metal-encapsulated spherical voids.

The Mie solutions to Maxwell's equations describe the electromagnetic scattering from a sphere of arbitrary size. Resonant solutions depend on the size of the sphere and on the dielectric function of the sphere and its surrounding environment. The equations are quite general, so by swapping the dielectric constant of the sphere and the surrounding medium, the modes of a spherical cavity within an infinite expanse of metal can be calculated(57; 60). For spheres much smaller than the wavelength of light ($kR \ll 1$, where k is the wave vector of incident light), the electric field can be considered electrostatic and the mode solutions $\omega_L = \omega_{2D}\sqrt{(L+1)/(2L+1)}$ are pushed above the *SPP* energy, depending on the number of radial nodes, L . As the void size increases, retardation effects modify the mode energies, mixing *SPPs* with Fabry-Perot cavity modes to produce a new class of void plasmons. These plasmon states resemble atomic orbitals with spherical harmonic components $Y_{L,m}(\theta, \phi)$ incorporating a vectorial character.

Due to the complex geometry of truncated spherical cavities, neither full 3D electromagnetic solvers nor analytic calculations can be utilised to effectively model the plasmonic modes of these structures. However, using a boundary element method (*BEM*)(61), our collaborator F.J.Garcia de Abajo has devised a computationally efficient solver for cylindrically symmetric structures, such as nanovoids(61). In the *BEM* model, the field inside a single isolated cavity is expressed in terms of the charges and currents of the structure surface. The boundary conditions provide a set of linear integral equations in these charges and currents that are decomposed in terms of each azimuthal $\exp(im\phi)$ component. Because coupling between different m components is forbidden, their solutions

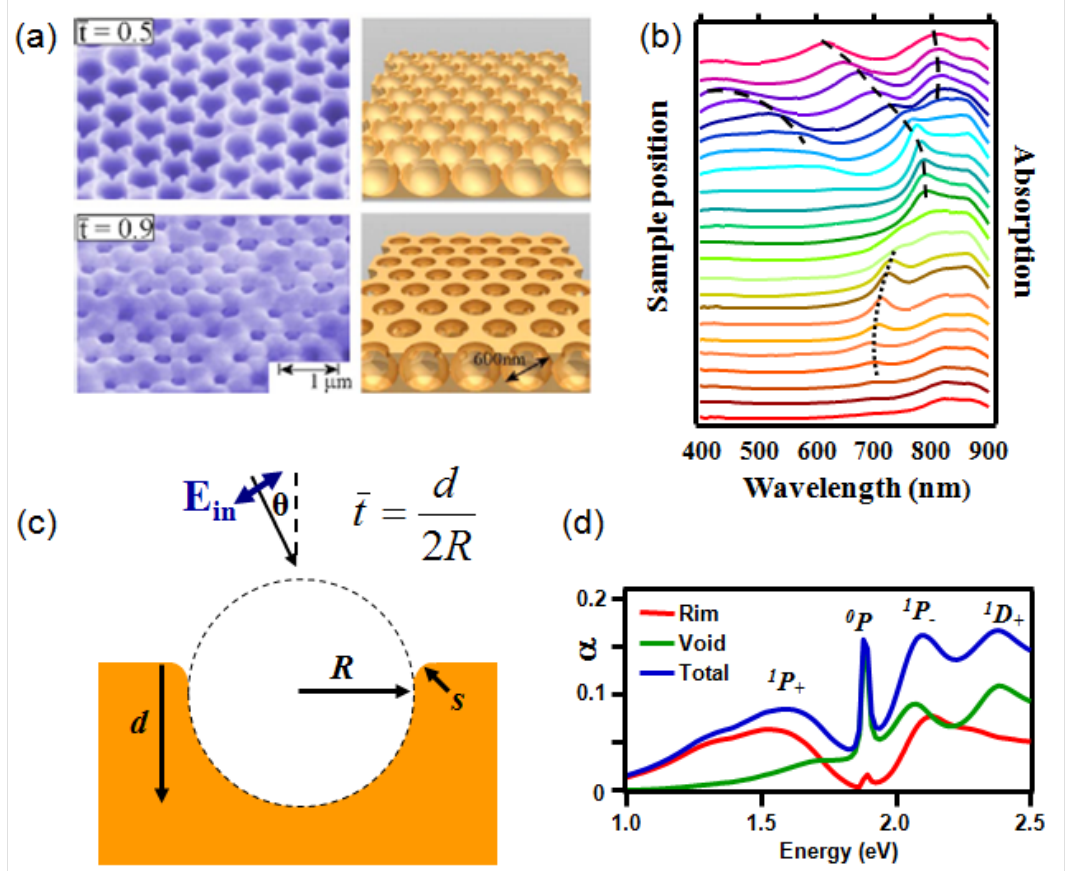


Figure 5.4: (a) *SEM* images (left) and morphologies (right) of 300 nm radius gold nanovoid structures, at normalised cavity thickness $\bar{t} = 0.5$ and 0.9 . (b) Experimental absorption spectra from a nanovoid structure which is graded in thickness from $\bar{t} = 0.1$ (bottom) to 0.95 (top). Dashed lines indicate void plasmon modes inside the cavities, and the dotted line an *SPP* surface mode. (c) Parametrisation scheme for a nanovoid cavity of radius R , with metal thickness d and rim rounding curvature s . (d) Theoretical absorption spectra of a nanovoid of $R = 250 \text{ nm}$, $\bar{t} = 0.92$ and angle of incidence $\theta = 60^\circ$, separated into absorption components from rim region and the interior of the void. Mode labeling is described in the text.

can be analysed independently despite mixing of the L components. Modes are labelled ${}^mL^{1,2}...P, D, F$, where the $L = 0$ mode is forbidden from symmetry arguments. Illuminating a single cavity embedded in a surface with a plane wave at a particular angle of incidence and polarisation allows the extraction of the 3D optical field distribution at each energy as well as the local absorption and Poynting vectors at the metal surfaces. The full frequency-dependent dielectric functions are used for both dielectric and metallic components. To parameterise the truncated void structure (figure 5.4(c)), the normalised thickness is again defined as $\bar{t} = d/2R$, where d is the planar metal thickness and R is the spherical void radius. All calculations presented in this thesis were performed by the author, and typically focus on illumination at visible and *NIR* wavelengths from 400 nm to 2 μm , corresponding to experiment. The upper rim rounding is typically set at $s = 10$ nm, although the mode absorptions and field profiles are found to be rather insensitive for $s \leq 100$ nm.

The absorption for a 250 nm radius cavity, thickness $\bar{t} = 0.92$ and incident angle of 60° is shown in figure 5.4(d), normalised to give absorption strengths comparable to voids in a hexagonal array. The absorption profile reveals several modes, not predicted by the Mie equations. Their mode assignments are based on the decomposition into azimuthal m components and the evolution from the well-defined L -states at $\bar{t} = 1$. While some modes have a narrow spectral width (such as 0P with $FWHM = 45$ meV, others exhibit broadband excitation (such as ${}^1P_+$ with $FWHM = 250$ meV). This arises from the excitation of strong rim dipole modes associated with charge buildup at the void rim for $\bar{t} > 0.6$. This rim mode has $m = 1$ symmetry and will couple only to void modes with $m = 1$ of the same energy, resulting in mixed mode configurations with strongly enhanced fields(62; 63). The hybridised mode associated with the coupling between 1P and the rim is denoted as the lower energy, bonding mode (${}^1P_+$), and the higher-energy configuration as the antibonding (${}^1P_-$) mode [see later]. Such coupled rim-void modes do not exist in the corresponding nanoparticle structures. By identifying the absorption from different m states, and from different spatial regions of the metal surface, the origin of the different modes can be explored.

Experimental reflectivity measurements (figure 5.4(b)) show the tuning of the mode energies as the nanovoid is progressively truncated. The negatively

5.3 Void Plasmons

curved void surface localises the electromagnetic energy in an enclosed region, with higher-order modes increasingly localised at the metal surface. As the nanovoid is increasingly truncated, the modes are less encapsulated and most of them move away from the metal and increase in energy. Approaching from the opposite limit, the modes at low \bar{t} resemble the Bragg plasmon dispersion, and in general, modes drop out of the *SPP* bands toward the Mie solutions as \bar{t} increases.

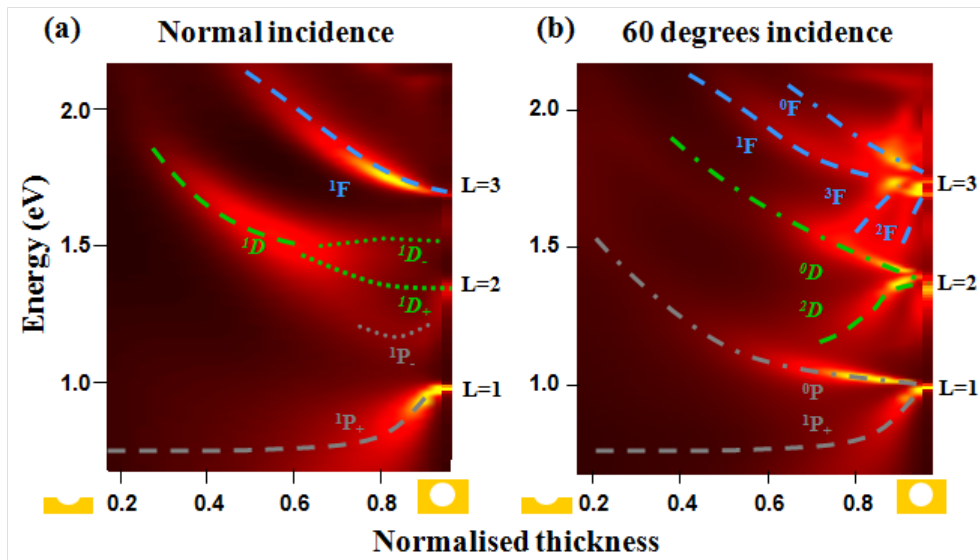


Figure 5.5: (a) Calculated normalised absorption for 500 nm radius gold nanovoids at (a) normal incidence and (b) 60° for increasing film thickness. Dashed lines are guides to the eye, with labeling described in text.

Using the *BEM* model, the actual thickness behavior is revealed in detail in figure 5.5 through the absorption spectra of incident light at both normal incidence and 60° . A rich variety of modes are observed that display a strong energy dependence on the structure morphology. While the modes are strongly dependent on the dimensions of the cavity, all the representative phenomena of note are exemplified for the 500 nm radius cavity shown. On the right side are indicated the $L = 1,2,3$ Mie solution energies in the equivalent full spherical cavity. Clearly evident is the way that these modes split and evolve in energy as

5.3 Void Plasmons

the thickness decreases. Near $\bar{t} = 1$, the modes spectrally sharpen and become isolated from the incident light, matching in detail the Mie solutions.

By examining (figure 5.6) the electric field distributions $|E(r)|^2$ for specific m components, the different modes can be identified. The electric field distribution and vector orientation of each Mie solution (plotted on right-hand side) show which truncated mode they correspond to. Low m modes have optical fields closer to the central z-axis of the void, in less contact with the metal surface. The field vector orientations give a clear understanding of the angle dependence. While modes with $m = 0$ have vertical field alignment that cannot couple to normally incident light, in contrast, $m = 1$ modes are well coupled at normal incidence. The sharpest low-energy mode is the 0P , which is only seen for $\theta > 0^\circ$ (gray, figure 5.5(b)). As the full spherical cavity is truncated, the charge distribution of this mode at the top of the void is strongly perturbed and hence the mode energy rapidly rises (figure 5.6(i)). As the thickness reduces further, the optical coupling to this mode weakens and it draws closer to the metal surface. For low \bar{t} , the 0P turns into a standing wave of propagating *SPPs* which are tethered to the shallow dishes. The tight field distribution and poor symmetry match to incident light mean that this mode is not well coupled for absorption at small thicknesses.

On the other hand the 1P mode shows a very different behavior (figure 5.5(a)). This mode energy splits immediately as the cavity is truncated. This is because the mode strongly couples to the rim dipole mode. The resulting low-energy ${}^1P_+$ bonding mode has field vectors of void mode and rim mode that are parallel (figure 5.6(ii)). On the other hand, the higher-energy antibonding ${}^1P_-$ mode has antiparallel alignment of these field vectors (figure 5.6(iii)), which causes it to have very weak coupling to incident light. As the cavity is further truncated, the ${}^1P_+$ mode drops to a fixed energy and loses its absorption strength. This is because the mode rises above the metal surface and eventually at low \bar{t} corresponds to the interference standing wave of incoming and reflected light, which has a field null at the metal surface. The contrasting positions of field maxima within the cavity for the ${}^1P_+$ and 0P modes (arrows in figure 5.6) highlights the key role of the rim in attracting and repelling the light fields to and from the metal surface. Because the ${}^1P_+$ mode has a strong rim component, it is sensitive to the rim shape and

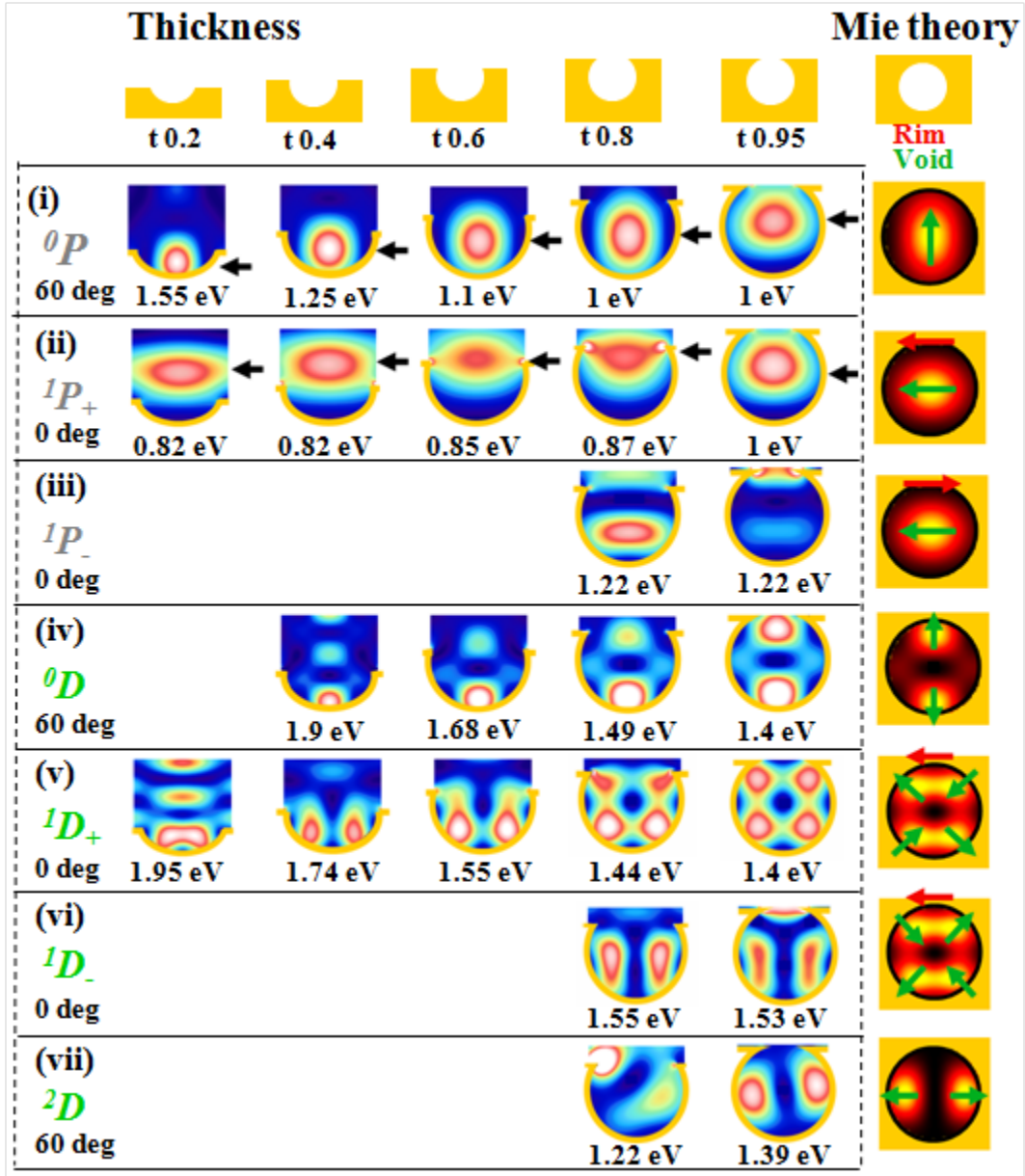


Figure 5.6: Electric field distributions at increasing thickness, with (right) field profiles from Mie theory. Vertical position of the maximum optical field for the ${}^1P_+$ and 0P modes with increasing \bar{t} indicated by black arrows. Field orientations for rim (red) and void (green) modes indicated by arrows.

height and only loses absorption strength as the void mode moves further above the rim height.

A similar type of behavior is seen for the $L = 2$ modes (green dashed lines in figure 5.5). While the 1D mode exhibits strong coupling to the rim mode, near-degeneracy with the $^1P_-$ mode results in further mixings, creating three broad mixed modes for $\bar{t} > 0.6$. For $\bar{t} < 0.6$, the 1D mode dominates the spectrum: the skewed vector alignment of the two strong field lobes close to the metal surface either side of the void bottom (figure 5.6(v)) gives it good symmetry overlap with $m = 1$ incident light. For $\bar{t} > 0.7$, this mode resembles a whispering gallery mode(64) with multiple field nodes at the metal surface. On the other hand, for small \bar{t} , this mode resembles the interferometric standing wave, but with a phase shift that brings it very close to the metal surface. At normal incidence, the $m = 0$ mode is not coupled due to its vertical field orientation, while the $m = 2$ mode is also not seen because of its back-to-back field orientation (figure 5.6(vii)). The $m = 0$ mode has associated charge maxima situated right at the top of the void and is most perturbed by the initial truncation. Eventually, on further truncation, the 0D mode becomes the second-order *SPP* mode, while the 2D mode disappears. A similar story is repeated with the $L = 3$ modes (blue dashed lines in figure 5.5), with the 1F mode absorption dominating at normal incidence.

Experimental spectra reveal a strong angle dependence of the absorption from the low L void modes. Although typically non-dispersive (the lack of energy dependence on angle of incidence is indicative of their localised spatial extent), the modes preferentially absorb at particular incident angles. The angle-dependent absorption of unpolarised light for a 500 nm radius void at $\bar{t} = 0.95$ is shown together with selected $|E|^2$ field plots in figure 5.7(a). The m -dependent coupling is clearly resolved, with angle-dependent absorptions for the 0P , $^1P_+$, and 0D modes extracted in figure 5.7(c). The narrow spectral line width of the 0P mode is ascribed to its lack of radiative coupling to the rim, which both decreases its total absorption strength (and hence radiative decay), and its penetration into the metal (and hence current-induced heating). The absorption matches the expected angular overlap of the incident and void-mode fields in the far field radiation zone(65) (dashed lines) with an additional $\cos(\theta)$ falloff due to the reduced

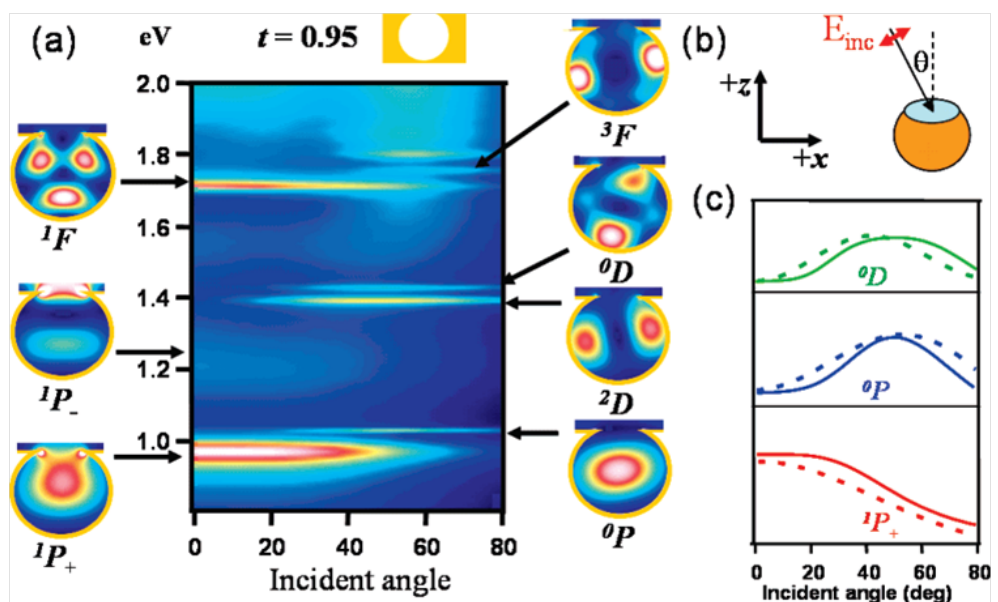


Figure 5.7: (a) Angle-dependent absorption of 500 nm radius nanovoid at $\bar{t} = 0.95$ together with selected $|E|^2$ field plots. (b) Orientation of incident light onto the void and rim gives (c) observed absorption vs angle of the P and D modes. Theory lines (dashed) described in text.

area viewed by an angled incident beam: for the 0P , this goes as $[\sin^2(\theta)]\cos(\theta)$ and the 0D goes as $[\sin^2(\theta) \cos^2(\theta)] \cos(\theta)$. By contrast, the 1P follows a $[1 + \cos^2(\theta)] \cos(\theta)$ angle dependence. At normal incidence, only $m = 1$ modes are excited: the ${}^1P_+$ mode is strongly coupled due to its interaction with the radiative rim mode, while the ${}^1P_-$ is almost invisible. As the angle of incidence is increased, the strength of coupling between void and rim mode is modified, with a maximum coupling at 25° . One result of these dependences is that, in an optical microscope configuration, for a typical $\times 20$ objective with $NA = 0.2$, only the $m = 1$ modes are observed. The intrinsic angle-dependent coupling to these modes has significant implications for the applications of these nanostructures, for example as substrates for *SERS* in typical microscope geometries.

Experimental reflectivity measurements for a 500 nm diameter void structure graded in thickness are compared with calculation in figure 5.8. For this structure, the few modes present are widely separated in energy, allowing their precise characterisation. At $\theta = 0^\circ$ (figure 5.8(a)), two distinct high-energy plasmon modes red-shift for increasing thickness, while an extra low-energy mode (dashed box) is associated with triangular tip features [discussed later], present on structures around $\bar{t} = 0.5$. The first mode (white) rises in energy for $\bar{t} > 0.8$ and comparing with calculation (figure 5.8(b)) is identified as the ${}^1P_+$ mode. The second mode (blue) drops monotonically in energy with \bar{t} , matching with the theory prediction of the ${}^1P_-$ mode; its strong absorption is due to increased ϵ_{Au}'' at shorter wavelengths. The 0P mode is not observed in the experimental data, possibly due to the weaker confinement provided by experimental cavities which feature windows between neighbouring voids.

Several differences between the experimental and simulated structures complicate comparison. Bragg plasmons are strongly coupled for void thicknesses $\bar{t} < 0.4$ and also for $\bar{t} > 0.85$. The Bragg plasmon is degenerate with the ${}^1P_-$ mode, resulting in a modified dispersion for this mode. A second difference are small holes into the top of the voids even for $\bar{t} = 1$ due to geometry-limited electrochemical growth. Therefore, the voids are never completely encapsulated, inhibiting the development of $m = 0$ modes and modifying higher m modes (hence the discrepancy for ${}^1P_+$). Third, for $\bar{t} \approx 0.5$, the appearance of a low-energy mode

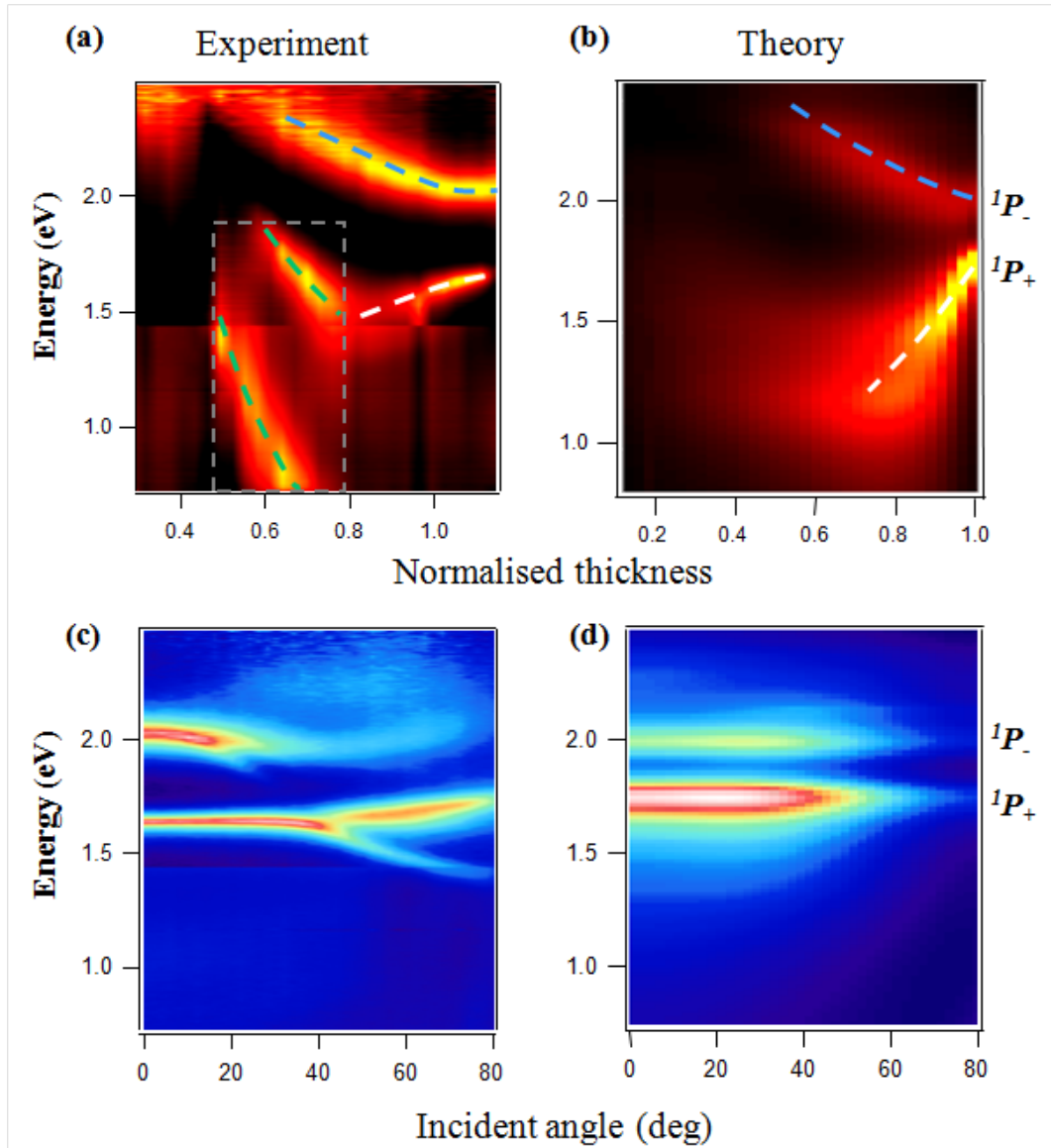


Figure 5.8: (a) Measured and (b) calculated absorption for 500 nm diameter nanovoid structure graded in thickness from thin (left) to thick (right) at $\theta = 0^\circ$ (lines track plasmon modes). (c) Experimental and (d) calculated dispersion for the structure near full encapsulation, $\bar{t} = 0.99$.

5.3 Void Plasmons

coincides with the formation of bowtie-shaped features above circular windows between the voids, and is discussed in the following section.

5.4 Low Energy Plasmon Mode

As well as localised void plasmons located within truncated cavities, nanovoids support a localised plasmon mode which is associated with the bowtie-shaped features present on structures of thickness $\bar{t} \approx 0.5$. The bowtie feature is formed at the contact point between neighbouring spheres in the template layer (figure 5.9(a)), where the re-arrangement of the polymer around the contact points forms a neck between spheres with a diameter of 10% that of the spheres themselves. Electrodeposition through the template produces an inter-connecting hole with two free tips (which comprise the bowtie feature) that close to form a ring around the polymer neck as $\bar{t} \rightarrow 0.6$, shown in figure 5.9(b).

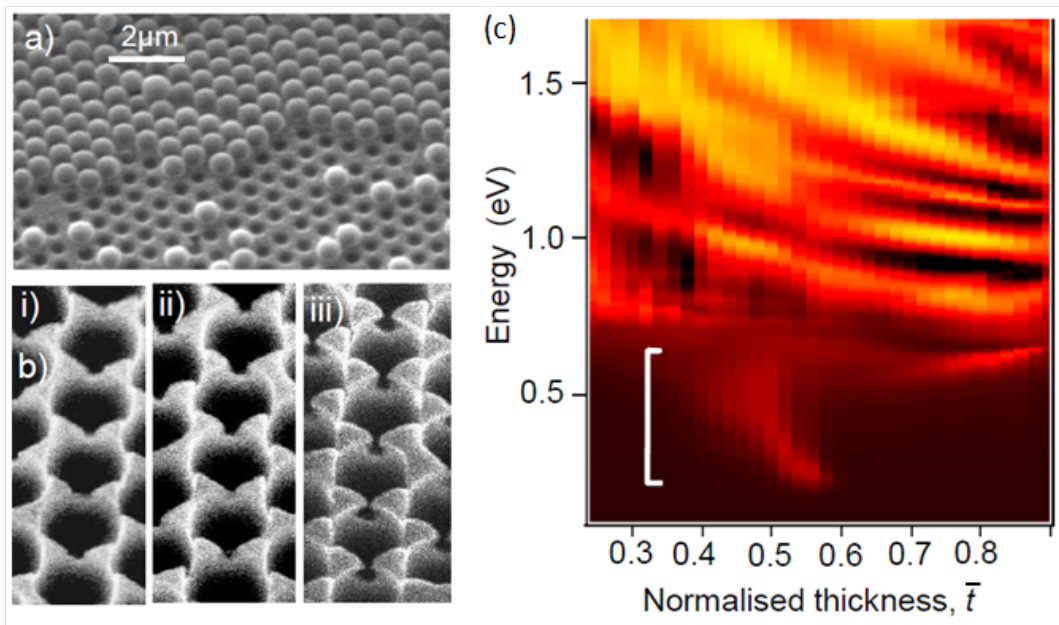


Figure 5.9: *SEM* images of (a) monolayer $D = 600$ nm sphere template over partly electrodeposited gold film, (b) detail of growth around touching spheres for (i) $\bar{t} \approx 0.4$, (ii) $\bar{t} \approx 0.5$, (iii) $\bar{t} \approx 0.6$. (c) Absorption map for a $D = 1600$ nm graded nanovoid sample showing the low-energy mode below 0.6 eV marked by a white bar.

Position resolved absorption measurements reveal a strong correlation between the presence of the bowtie features and a localised plasmon mode which tunes to

5.4 Low Energy Plasmon Mode

the *IR* with increasing \bar{t} . Absorption data for a $D = 1600$ nm graded nanovoid sample (figure 5.9(c)) shows that the plasmon mode appears as the structure thickness exceeds $\bar{t} \geq 0.4$, and drops in energy as the sample thickness approaches $\bar{t} = 0.6$. Fourier transform infra-red spectroscopy (FTIR) reveals that this mode rapidly tunes to the far-*IR* as the bowtie features re-connect, therefore this mode is henceforth referred to as the *low-energy* plasmon mode. Further proof that this low-energy mode is associated with the bowtie features is provided by the fact that this mode is not observed for samples which are fabricated using a double templating procedure(66) which produces truncated nanovoids with identical \bar{t} , but which do not have bowtie features.

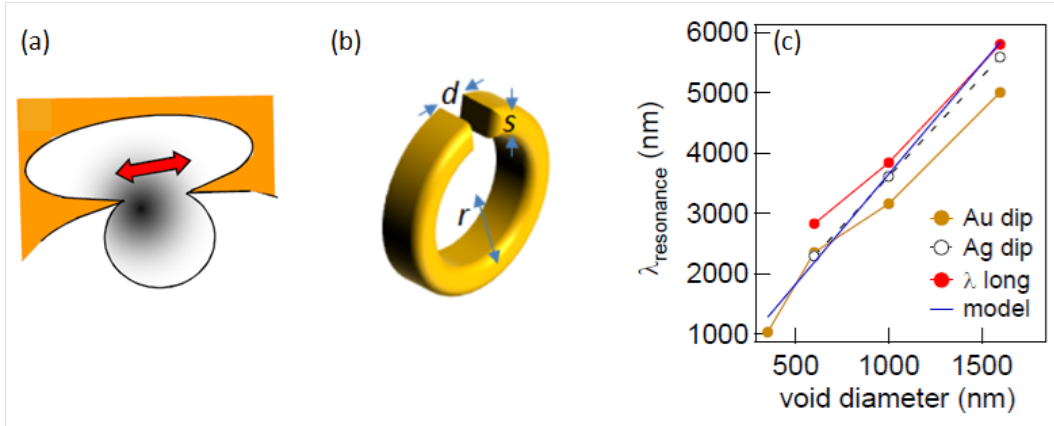


Figure 5.10: (a) Schematic low-energy mode. (b) *SRR* model geometry. (c) Low-energy mode resonant wavelength vs. template sphere size.

A simple analytical model has been devised which accurately reproduces the spectral tuning of the low-energy mode(67). In this model, the bowtie features and accompanying metal surrounding the hole between voids are described by a crescent split-ring resonator (*SRR*) that acts as nanoscale LC circuit (figure 5.10(a,b)). This simple loop inductor has a capacitance $C = \epsilon_0 s^2/d$ and a magnetic inductance given by $L_m = \mu_0 \pi r^2/s$, where s is the frequency-dependent skin depth. In addition there is an extra electron inductance in this geometry, $L_e = 2\pi r/\epsilon_0 \omega_p^2 s^2$ which exists due to the kinetic energy of the electrons(68). These contributions form an LC circuit which resonates at the angular frequency

5.4 Low Energy Plasmon Mode

$\omega_{res} = 1/\sqrt{LC}$, giving a resonant wavelength $\lambda_{res} = 10r\sqrt{s/d} \approx D\sqrt{s/d}$. Taking the skin depth for gold in the *NIR* of $s = 25$ nm, and a gap width of $d = 3$ nm gives a resonant wavelength around $5 \mu\text{m}$, in reasonable agreement with experiment (figure 5.9(c)). In addition, this model predicts a linear scaling with the sphere diameter as found experimentally (figure 5.10(c)).

As the *SRR* gap closes the field of the low-energy mode becomes increasingly compressed into a volume of dimension $\approx d^3$, before the mode abruptly disappears as the bowtie features re-connect and the *SRR* loop is closed. This indicates that this mode provides strong electric-field enhancements around $\bar{t} = 0.6$ which may contribute to the surface enhanced Raman signals recorded from these structures. Furthermore, coupling to this mode is independent of the sample azimuthal orientation and the optical polarisation of incident light, since of the symmetry of the original close-packed 2D spheres results in 6 vertically-oriented *SRR* features around each void.

5.5 SNOM Mapping of Void Plasmons

Whilst reflectivity measurements provide detailed information about the dispersion of plasmons in nanovoids, they do not provide direct verification of the local electric fields in experimentally realised void arrays (and calculations are for isolated voids only). *SNOM* is a microscopy technique which directly probes the electric near field of nanostructures. A series of *SNOM* measurements were performed by P.D. Lacharmoise at the Institut de Cincia de Materials de Barcelona-CSIC with the aim of investigating the influence of edges and defects on the localised near field properties of nanovoids(69).

A schematic of the experimental setup used for *SNOM* imaging is shown in figure 5.11(a). A laser beam at 45° incidence is focused onto a spot of 5 - 10 μm in size at the sample surface. An aluminum coated tip with an aperture diameter of 80 nm scans the excited area at a constant distance of 10 - 20 nm above the surface and collects the electric near field. The dependence of the local field distribution on the laser excitation energy was mapped on a $D = 600$ nm gold nanovoid sample, shown in figure 5.11(b). The *SNOM* images reveal clear differences for the three laser excitation energies selected. For $E = 2.41$ eV a ring-shaped near-field signal is detected inside each cavity, close to the void edges. When excited at 1.96 eV, a completely different pattern is observed, with a void-centered bright signal apparent at the bottom of the cavities. Finally, no clear features can be identified at the voids for the 1.58 eV light. Figure 5.11(d) shows line profiles of both *SNOM* and topography signals along the lines marked on the images of figure 5.11(b) for 2.14 eV and 1.96 eV excitation. The lines along which the intensity cuts were performed effectively map the plasmon electric field distribution inside the voids. As indicated in figure 5.11(a), the tip enters into a void keeping constant the distance s to the void rim. Thus, the tip moves along a funnel-like surface rather than a circular one, leading to topographic line profiles with triangular shape such as the ones displayed in figure 5.11(d). The maximum intensity of the plasmon excited with 1.96 eV light occurs at the void center, whereas for 2.14 eV excitation there is a node at this position and the intensity distribution peaks at a void centered ring of about 320 nm in diameter. The measured spatial field distribution show good agreement with the calculated

5.5 SNOM Mapping of Void Plasmons

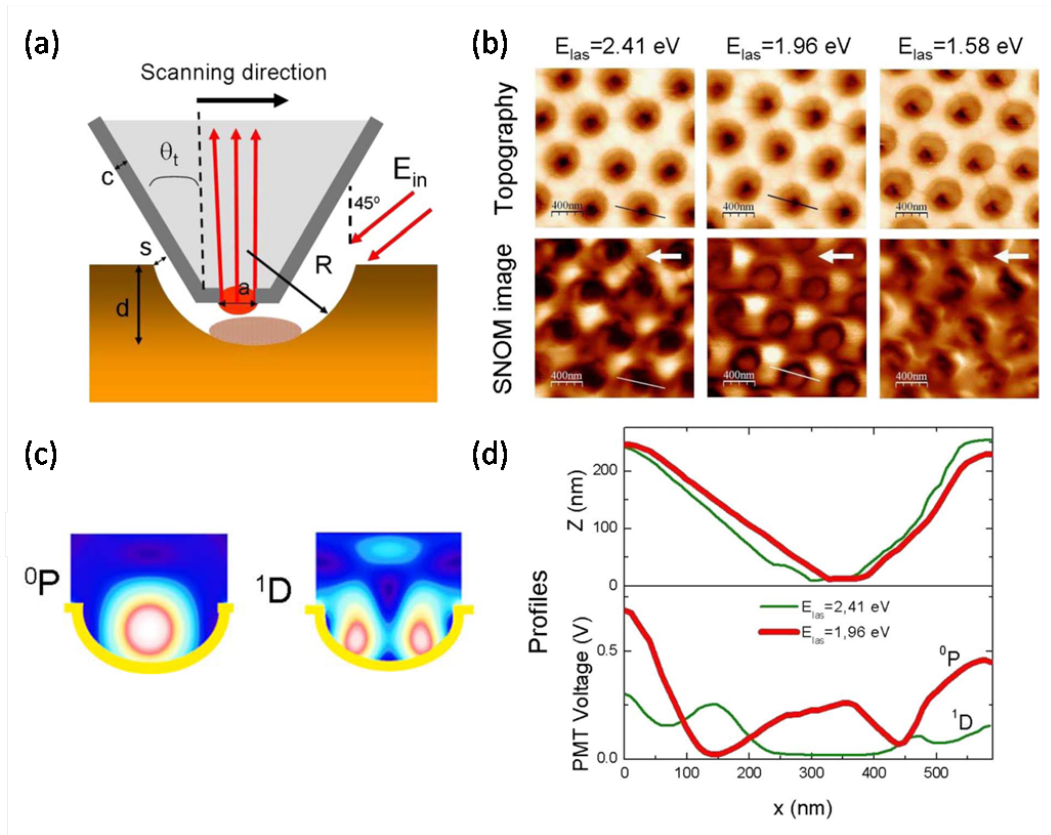


Figure 5.11: (a) Schematic of the experimental setup showing the *SNOM* tip and parameters of the gold nanovoid cavity (69). (b) Topography and *SNOM* images of a 300 nm radius void array at $\bar{t}=0.4$ obtained with different laser excitation energies. White arrows indicate the direction of illumination. (c) Field distributions calculated for the 0P and 1D void modes in a $\bar{t} = 0.4$ cavity. (d) Topography and *SNOM* line profiles along the black and white bars drawn on (b), respectively. Labels correspond to the assigned plasmon modes.

5.5 SNOM Mapping of Void Plasmons

empty void field profiles at these energies, identified as the 0P and 1D modes, shown in figure 5.11(d).

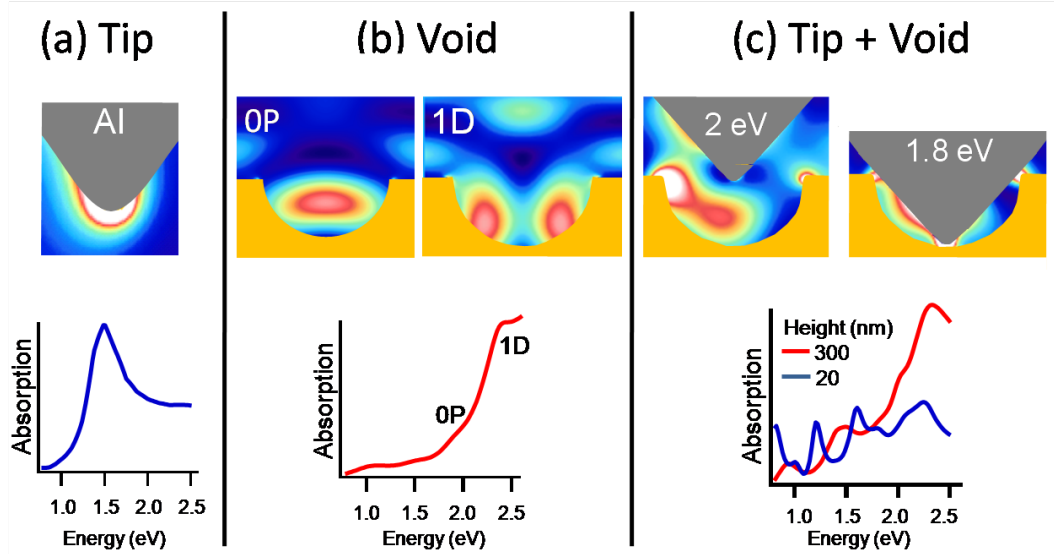


Figure 5.12: Theoretical absorption spectra and on-resonance intensity distributions when illuminated at 45° for (a) aluminium tip alone, (b) void alone at $\bar{t} = 0.5$, and (c) both tip and void with tip level with the rim and at 20 nm above the metal. A 0P like mode at 2 eV is forced down onto the metal by the tip, and a mode at 1.8 eV shows the rim coupling light to the void and tip.

Although these *SNOM* profiles show a remarkably close resemblance to the calculated field distributions of an isolated truncated void, initial calculations on the tip *and* void system show that significant modifications of the plasmon modes are expected. The aluminium tip itself supports localised modes, which are strongly dependent on the tip apex radius, tip angle θ_t , and tip composition, shown in figure 5.12(a). The tip and void modes interact, resulting in new mixed states whose energies and field distributions strongly depend on the penetration of the tip inside the void, shown in figure 5.12(c). However, the calculations confirm that despite the geometrical shadowing caused by the tip for light accessing the nanovoids, the *SNOM* tip clearly maps localised plasmon features within the nanovoids. This suggests that *SPP* modes on the top surface and localised rim modes are coupled to the localised plasmons down in the bottom of the voids,

thus providing a path for light to couple into the *SNOM* tip. This coupling is of great importance for *SERS* sensing applications of molecules, and suggests that a *SNOM* version of *SERS* would be possible in the nanovoid geometry.

5.6 Conclusion

The nanovoid geometry supports a rich variety of plasmon modes, including propagating Bragg plasmons and localised void and tip plasmons. A simple weak scattering approximation accurately describes the energetics of the Bragg plasmons, whilst calculations go someway toward describing the void plasmons located within truncated nanovoids. Calculations show that the L spherical void modes are split by truncation into a number of m states, whose energy tuning with thickness depends closely on the field distribution of each mode. Precisely where absorption takes place on the metal surface is set by the mode numbers, the angle of incidence, and the mode geometry in non-trivial ways. Around half-cavity height, bowtie features are formed which support a low energy plasmon mode which rapidly tunes to the far-infrared with increasing cavity thickness and provides strong local field enhancements. Future calculations and *SNOM* measurements may provide a comprehensive understanding of the plasmonic modes of truncated nanovoid *arrays* and include the influence of edges and window features realised in experimental structures.

Chapter 6

Plasmon Interaction and Control

6.1 Introduction

Nanovoids support a rich variety of plasmonic modes which can be modified by the structure geometry and local dielectric environment. The ability to tune a plasmon resonance or localise electric fields at specific positions in a nanostructure is desirable for almost all plasmonic applications. This chapter explores how the plasmon modes of nanovoids can be modified using a number of approaches. Firstly, experiments are conducted to show how the plasmon resonance energy can be simply tuned as the refractive index of the top dielectric layer is changed. Next, nanovoid structures where the spheres have been left in at the fabrication stage are investigated. These micro-sphere samples are shown to possess novel optical and plasmonic properties, and represent the smallest microsphere resonators yet demonstrated. Thirdly, by fabricating nanovoids in linear arrays, it is possible to guide plasmons on a substrate, creating a plasmon waveguide. Finally, hybrid nanovoid structures composed of multiple metals are shown to possess modified plasmonic properties, and represent a new route toward tailoring plasmon modes for specific applications such as surface enhanced Raman spectroscopy.

6.2 Tuning Plasmons with Refractive Index

Surface plasmons are highly sensitive to variations in the refractive index at the metal/dielectric interface, a result exploited to create novel molecule sensors⁽⁷⁰⁾. The simplest example of this effect is the tuning of a plasmon resonance by immersion of a substrate in solution, producing particularly clear results for Bragg plasmons. Using the automated goniometer, it is straightforward to map the dispersion of Bragg plasmons in air and water. A small fluid cell is created on a nanovoid sample by using a glass cover slip, raised by around 200 nm from the gold surface and fixed in place with Parafilm.

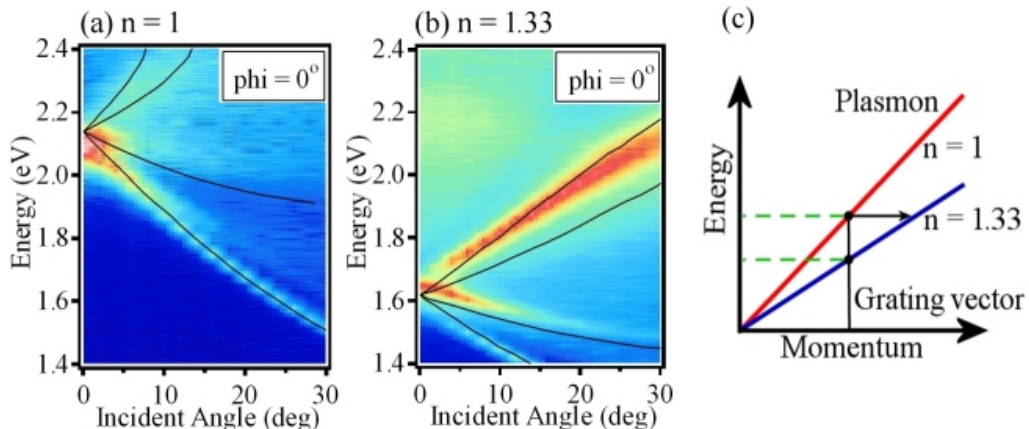


Figure 6.1: Dispersion maps for a 600 nm diameter gold sample in (a) air and (b) water. (c) Schematic showing change in dispersion relation with increasing refractive index of dielectric layer⁽¹⁾.

Figure 6.1 shows dispersion plots for a 600 nm diameter gold sample at $\bar{t} = 0.1$ in air and water. In both sets of data the glass cover slip is present to allow direct comparisons between the data. Theoretical dispersions calculated using equation 2.15 with a value of $\epsilon_d = 1.77$ ($n = 1.33$) used as the effective dielectric constant are seen to fit very well with the data. This dielectric constant is suitable over the range of energies considered⁽⁷¹⁾.

The change in plasmon energy for different refractive indices can be understood by considering the momentum of the optical field. If light starts in free-

space then passes into the fluid cell the k_{\perp} component of its momentum will increase, as shown in figure 6.1(c). The crossing point between the grating vector and the plasmon dispersion provides the solution to the observed mode. Since the periodicity of the structure remains constant, the solution for light in water will be of a lower frequency than in air. For diffractive effects, a shift exactly equal to the refractive index is expected. For surface plasmons the shift will be slightly smaller due to the effective dielectric constant dependence on the refractive indices of both media (equation 2.15). The data fits well with that of a shifted Bragg plasmon mode, as would be expected. Whilst the tuning observed for *SPPs* on thin samples is straight-forward to interpret, the situation becomes more complicated as the structure thickness is increased and localised plasmon modes come into existence.

6.3 Microsphere Samples

Microspheres form one of the key elements in many nanophotonic devices due to the tight confinement and strong enhancement of the optical field they provide. Individual dielectric spheres support optical cavity modes which take on the form of whispering gallery modes (*WGMs*) for sufficiently large sphere dimensions, shown in figure 6.2. However coupling into microspheres has typically proven difficult due to the weak exponentially-decaying evanescent external field, and has to date been demonstrated only with nano-positioned elements such as prisms(72; 73), modified optical fibre probes using tapers(74), etch-eroded-(75) or angle-polished-(76) fibre tips, half-block fibre couplers, or planar waveguides(77). Such methods require precise nanometre control in the optical near field, placing tight tolerance limits on both alignment and fabrication. Moreover, current *WGM* research has tended to focus on relatively large dielectric microspheres (from several to hundreds of microns) with high Q - factors and which support many closely spaced modes of very narrow linewidth. However this mode quasi-degeneracy and the large sphere size restricts the range of potential nanophotonic applications. Additionally, microspheres are frequently supported on flat or grooved substrates, with the outer surface in air or liquid, providing limited scope for the control of interactions.

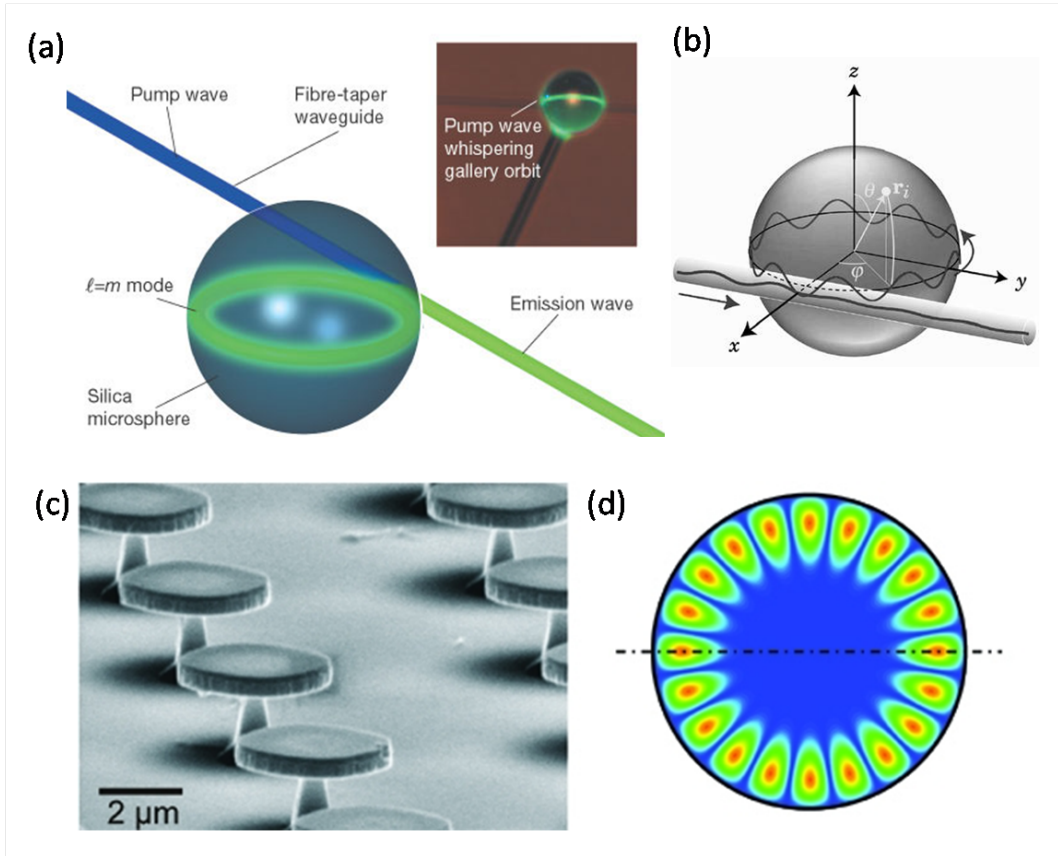


Figure 6.2: (a) Illustration of a fibre coupled dielectric microsphere *WGM* resonator⁽⁷⁸⁾. The green orbit is a $l = m$ mode supported at the spheres inner surface. Inset: photograph showing a doped microsphere. The green emission traces the *WGM* orbit. (b) Illustration of the *WGM* ray path within the sphere⁽⁷⁹⁾. (c) Semiconductor microdisks and (d) simulated *WGM* mode⁽⁸⁰⁾.

By modifying the fabrication procedure described in chapter 3 it is straightforward to produce self-assembled arrays of microspheres embedded in a plasmonic medium (henceforth referred to as a microsphere samples). These modified nanovoid structures posseses radically altered optical and plasmonic properties, more complex than those of nanovoids tuned by filling with solution. Significantly, these structures demonstrate for the first time that light can be efficiently and easily coupled into *sub-micron* microspheres by embedding them in a plasmonic

medium.

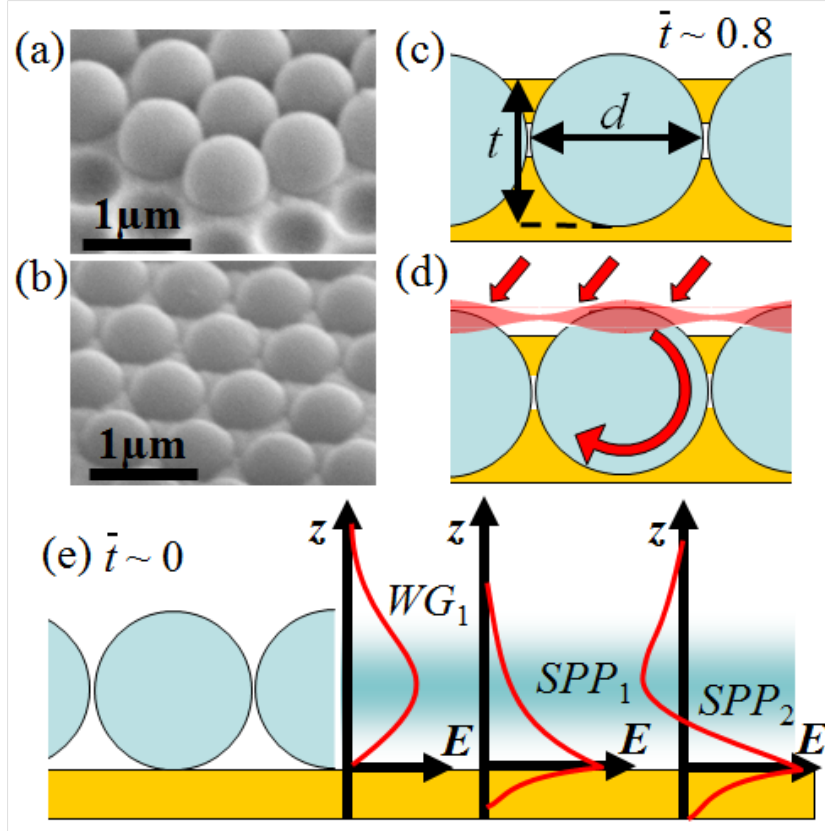


Figure 6.3: (a,b) Angled SEM images of 700 nm diameter spheres at (a) $\bar{t} = 0.15$, (b) $\bar{t} = 0.55$. (c) Schematic film cross-section for normalised thickness $\bar{t} = t/d$ for thickness, t , and diameter, d of $\bar{t} = 0.8$. (d) Schematic SPP_2 coupling. (e) Schematic field profiles for a waveguide mode WG_1 , first surface plasmon (Bragg) mode SPP_1 , and second surface plasmon mode SPP_2

Microsphere samples support both localised and delocalised SPP modes, evident in the experimental dispersions for spheres of 600 and 900 nm diameter (d) shown in figure 6.4. Thin samples $\bar{t} \sim 0$ (figure 6.4(b,f)) clearly support a variety of modes with energies strongly dependent on their in-plane wavevector, characteristic of delocalised propagation. Although more complicated than the bands observed for nanovoid samples, good agreement is found between the observed modes and band structures calculated using the weak scattering model

6.3 Microsphere Samples

(equation 5.1), shown in figure 6.4(a,e). Three principal sets of delocalised modes are seen with effective refractive indices \bar{n} corresponding to a waveguide mode WG_1 (black, $\bar{n} \sim 1.6$) formed by the touching spheres, a first order surface (i.e. Bragg) plasmon mode SPP_1 (blue, $\bar{n} \sim 1.0$) tied to the metal surface, and a second order surface plasmon mode SPP_2 (red, $\bar{n} \sim 1.4$) tied to the metal surface but extending further into the spheres. These delocalised modes exhibit 6 fold symmetry in azimuthal measurements with ϕ , accounted for in the band fittings. The WG_1 and SPP_2 modes have significant field strength within the periodic sphere layer, and hence are more efficiently diffractively coupled than the SPP_1 mode for thicknesses $\bar{t} < 0.5$. The planar waveguide mode WG_1 formed by the chains of touching spheres has elsewhere been termed a *nanojet* mode in 1D propagation(32).

As the thickness of gold is increased from $\bar{t} = 0$, the area of surface available to the SPP_1 mode is reduced and it temporarily disappears around $\bar{t} = 0.5$, reappearing only around $\bar{t} \sim 1$. Similarly the WG_1 mode becomes occluded when the gold reaches half the sphere height and is no longer directly coupled. In contrast, the second-order SPP_2 mode which originates at the gold surface breaks apart into discrete non-dispersive modes by $\bar{t} \sim 0.5$, seen in both s (or TE) - and p (TM) - polarisations, shown in figure 6.4(c,d,g,h). The energies of these discrete modes are independent of ϕ and match well with Mie calculations of the localised plasmonic modes inside microspheres of refractive index $n = 1.6$ embedded inside gold, also shown in figure 6.5(c,d,e,f). Together with the θ - independence of the mode energy (clearest in s - pol) seen for thicknesses $0.4 < \bar{t} < 1$, this behaviour confirms the localised nature of these modes inside the spheres.

The localised plasmonic mode assignment is supported by extracting the dominant mode energies for a range of samples with nominal sphere diameters from $d = 0.6$ to $1 \mu\text{m}$ at $\bar{t} > 0.5$ which all show similar features, shown in figure 6.5(b). The observed localised modes absorb strongly at different angles, hence individual spectra show particular patterns of peaks, shown in figure 6.4(a,c,e,g). The extracted modes are compared to theoretical mode calculations, $E_l(d)$, in the perfect spherical void, calculated by matching boundary conditions at the void rim using the full frequency-dependent dielectric constant for gold (57; 60). Evidence is seen for mixing between near-degenerate TE and TM solutions, resulting in

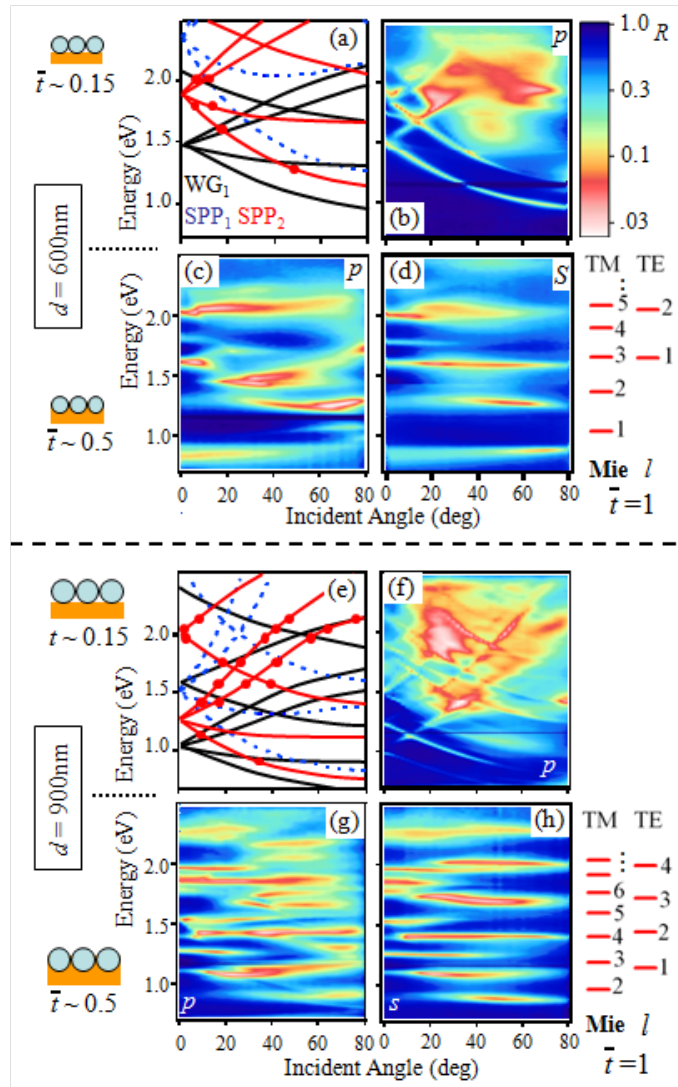


Figure 6.4: Dispersion relations, $E(\theta)$, with $\phi = 0^\circ$ for 600 and 900 nm diameter microsphere samples: (a,e) band theory of WG_1 (black), SPP_1 (blue) and SPP_2 (red) modes on a gold interface. Markers indicate the intersection of the SPP_2 dispersion with localised Mie modes. Measured reflectivity dispersions (on log scale, normalised to flat gold) for (b,f) p -pol at $\bar{t} = 0.15$, (c,g) p -pol at $\bar{t} = 0.5$, (d,h) s -pol at $\bar{t} = 0.5$. Plasmonic WGM energies are calculated from (60).

new modes labelled with a star (*) in figure 6.5(b). Mie theory reproduces well the observed trends and mode spacings with d and l .

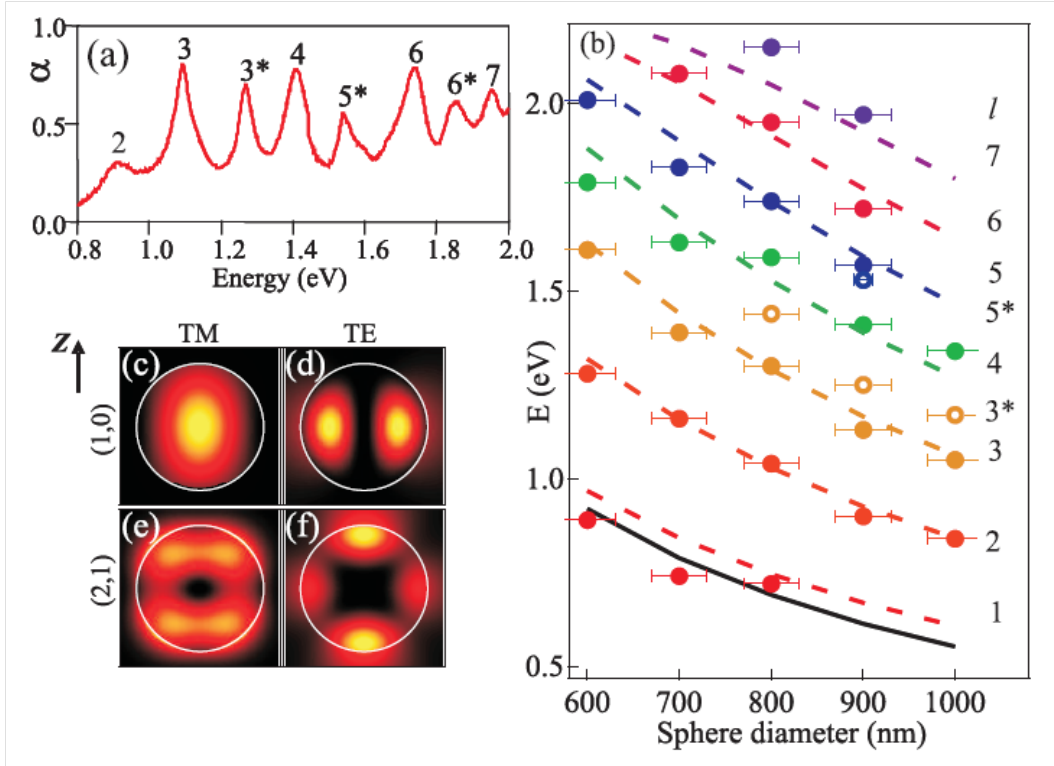


Figure 6.5: (a) Absorption spectrum $\alpha = 1 - R$, of 900 nm diameter microsphere sample at $\bar{t} = 0.6$, $\theta = 25^\circ$, $\phi = 0^\circ$ and s - pol. (b) Observed localised plasmon energies vs. sphere diameter, together with the calculated dependence of TM modes (dashed lines, labelled by radial mode number l). Theoretical limit of diffractive coupling (black line) also shown. (c,d,e,f) Corresponding computed field profiles in xz plane (rotationally symmetric about the z -axis) for $(l, m) = (1,0)$ and $(2,1)$ and TM , TE polarizations.

In Mie theory, each mode is classified by integral indices n, l, m which are the radial, angular and azimuthal mode numbers respectively, in accordance with the classification system of chapter 5. In the perfect spherical void calculation the mode energy is independent of m , while the modes with $n > 1$ occur at high energy and do not clearly appear in the data. However, due to their different boundary conditions, the modes with TE and TM polarisation have different energies. As $d \rightarrow \infty$, the TM large - l solutions tend to the conventional $SPPs$

6.3 Microsphere Samples

on flat gold, while the TE modes resemble the Fabry-Perot modes of spherical microcavities with field nodes at the metal surfaces (and thus they disappear on the flat surface). The TM mode intensity distributions (figure 6.5(c,e)) resemble those of the spherical angular harmonics, $Y_{l-1,m}(\theta, \phi)$, increasingly bound closer to the metal walls at higher l (2). While this simple treatment ignores the influence of the varying gold height encapsulation as well as the interaction with neighbouring spheres, it provides an appropriate basis to understand the system.

For $\bar{t} > 0.4$ incident light is coupled into the localised plasmonic modes with up to 98% efficiency. Measurements of s polarised absorption on thick samples highlight the uncoupled localised plasmons since for p polarisations the modes of neighbouring spheres can couple through the intervening metal surface which supports $SPPs$. Angle resolved measurements reveal a systematic variation of the angle of optimal coupling to the discrete localised plasmons, shown in figure 6.4(d,h). This provides strong evidence that coupling proceeds by diffractive coupling to the SPP_2 mode which is already localised inside the dielectric spheres and effectively mixed with localised plasmons (figure 6.3(d)). Essentially the dispersion is a convolution of the discrete Mie energies of figure 6.4(d,h), with the surface-mediating plasmons SPP_2 of figure 6.4(a,e), marked as the solid markers. The limiting condition for diffractive coupling (at $\theta = 90^\circ$) is given by (figure 6.5(b), solid line):

$$E_l(d) > \frac{4\pi\hbar c}{d\sqrt{3}(1 + \bar{n})} \quad (6.1)$$

which is satisfied even for $l = 1$, for all sphere sizes. Such diffractive coupling to low-order localised plasmons only works because of the surrounding metal which provides the delocalised plasmon. The energy, absorption depth, spectral and angular linewidths are extracted from the measured dispersions for each thickness and diameter, allowing a detailed characterisation of the localised plasmons. The broad angular widths ($\Delta\theta \sim 5 - 20^\circ$) observed imply that delocalised $SPPs$ travel only a few microns before their energy is transferred into the localised plasmons. The linewidth (and hence Q -factor) as well as the absorption depth are seen to only weakly depend on the encapsulation \bar{t} of the spheres. Between $0.6 < \bar{t} < 0.8$ the localised plasmon modes are further broadened, possibly due to mixing by the

6.3 Microsphere Samples

low energy mode associated with the triangular metal islands in the interstices between the microspheres. Plasmonic mode Q -factors reach a maximum of 30 for $\bar{t} \sim 0.95$ where radiative losses are suppressed by the small aperture. For these samples localised plasmons attain maximum absorption strengths of up to 98%. While both the linewidth and absorption strengths are not yet fully understood on these samples, it is probable that the linewidths are limited by the 2% size inhomogeneity of the spheres, rather than radiative, absorptive and coupling losses. For completeness, the full dispersion data set for intermediate metal thicknesses between shallow metal dishes and encapsulated spheres reveals the complicated mixing between Bragg and localised modes with \bar{t} , shown in figure 6.6.

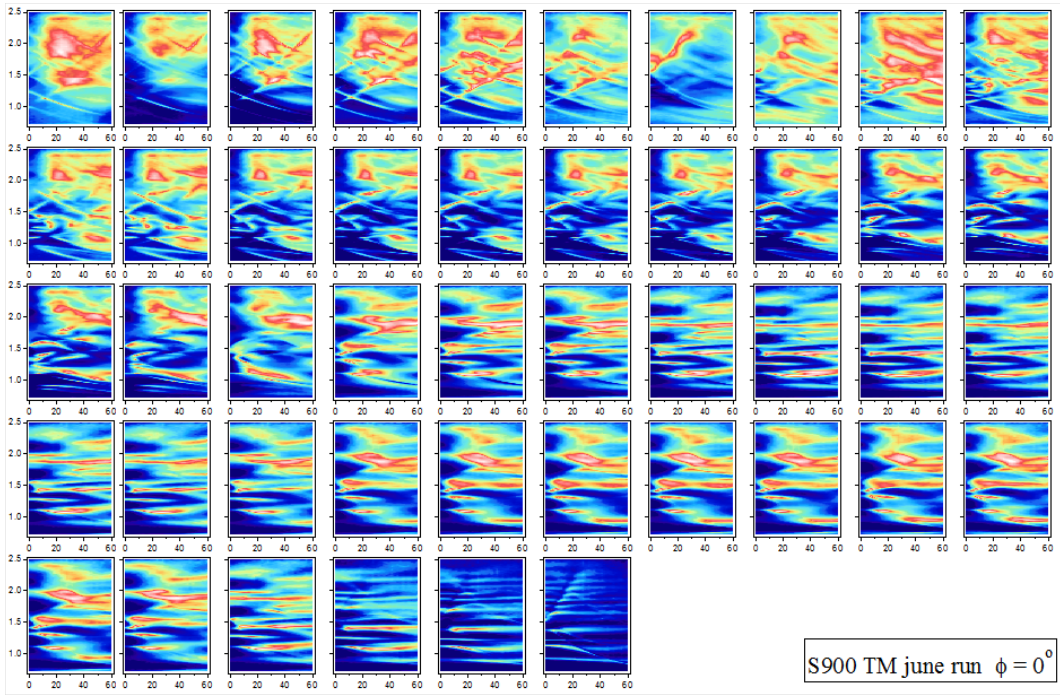


Figure 6.6: Full dispersion data set for a 900 nm diameter graded microsphere sample in p -pol for thicknesses from $\bar{t} = 0.1$ (top left) to 0.95 (bottom right).

As well as observing delocalised plasmon modes (analogous to electronic nearly-free electron bands), and localised plasmons (analogous to atomic orbitals), polarisation resolved measurements reveal nearest-neighbour coupling between lo-

6.3 Microsphere Samples

calised plasmons (analogous to tight-binding electronic bands). Coupling between spheres can occur either via the top metal surface or through small circular windows formed in-between the spheres (due to screening during electrodeposition within the microsphere geometry(2)). By uniformly coating the samples with an extra 6 nm of sputtered gold the spheres become encased in metal, modifying the coupling between spheres, shown schematically in figure 6.7. Hopping of localised plasmons between neighbouring spheres can be identified from the formation of minibands in the dispersion. Dielectric microsphere coupling has been identified previously in one dimension (81) from the photoluminescence (*PL*) emitted by larger 4 μm spheres stacked in a line. While such experiments allow only the discrete states to be observed as a function of the number of spheres in the chain, it is straightforward to map the full dispersion of microsphere samples using the automated goniometer, directly revealing the minibands.

Typical coupling data for thicker structures with $d = 900$ nm (figure 6.7 and full data set in figure 6.6), reveals the complex dispersion in the uncoated spheres resulting from the mixing of the $2(l + 1)$ degenerate modes at each $E_l(d)$. For barely-encapsulated spheres ($\bar{t} = 1.06$) coupling to the localised modes is evident, together with *SPP*₁ modes on the top surface which are only strong when near-degenerate to the localised modes (figure 6.7(c,d)). For smaller thicknesses the modes split and mix in complex ways. However in the coated sphere samples this coupling is reduced: the extra electromagnetic barrier formed by the 6 nm coating suppresses mixing with low l modes whose fields do not penetrate and overlap with either top surface or neighbouring spheres. Measurements at the same points before and after coating reveal reduced coupling between spheres, retaining only the *SPP*₁ mode for $\bar{t} = 1.06$ (figure 6.7(g,h)).

For thinner sample thicknesses \bar{t} (figure 6.7(e,f)) a number of new effects can be identified. Surface plasmons are visible in *p*-pol, propagating over the hemispherical domes (figure 6.3(b)). Minibands appear (figure 6.7(f)), with dispersions following a tight binding model, $E_k = E'_l + 2g \cos(ka)$ with Brillouin zone boundary, $k_{BZ} = \pi/a = 4.0\mu\text{m}^{-1}$ (dashed vertical line) and coupling strength, g , controlled by the mode overlap between spheres (which increases with l). Mixing of Bragg modes and minibands is observed for *p* - polarisation, shown in figure 6.7(e). No theory currently exists for such tight-binding calculations in a

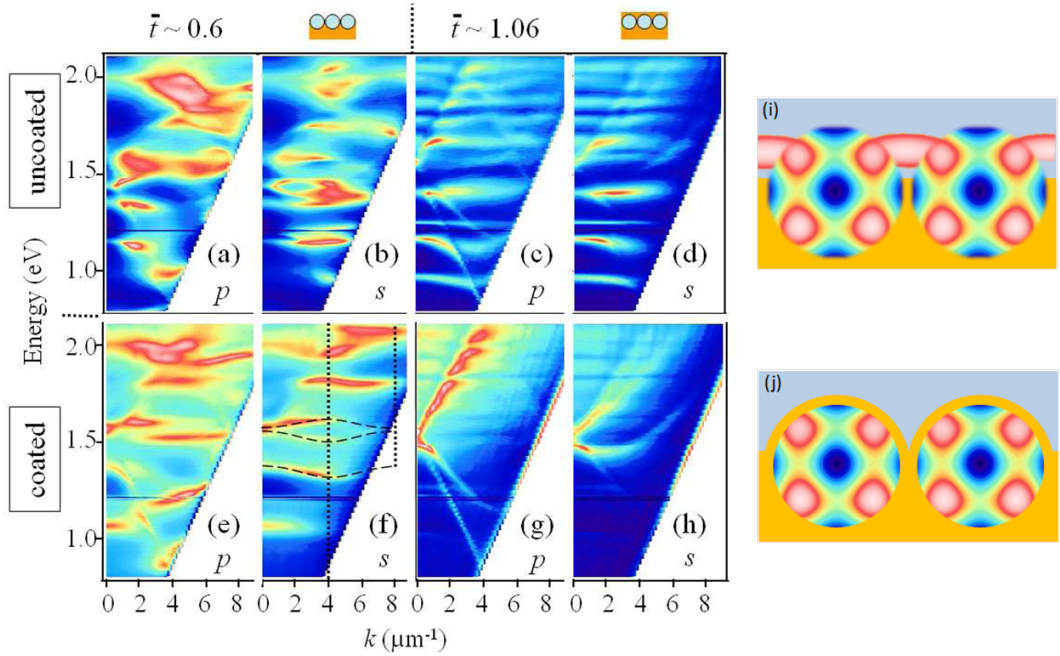


Figure 6.7: Experimental s, p dispersions $E(k)$ for a 900 nm diameter microsphere sample at thicknesses $\bar{t} = 0.6$ and 1.06 using (a-d) uncoated spheres and (e-h) spheres overcoated with 6 nm of gold. Dashed lines in (f) show minibands. (i) Schematic showing mixing between WGM modes in neighbouring spheres and (j) with mixing suppressed by metal coating.

2D-triangular lattice for confined vectorial fields with different l . However the reasonable fit to a 1D linear model suggests that such a development is attainable. The full evolution of plasmonic modes as both the thickness \bar{t} and coating are systematically varied gives an insight into how the coupling proceeds: for $\bar{t} \sim 0.5$ or 1, the localised modes remain rather stable whereas for $\bar{t} \sim 0.75$ or 0.25 they display a great sensitivity to \bar{t} . This indicates that modes with field profiles which overlap with the upper metal surface (figure 6.7) are most involved in plasmonic hopping, and that the metal surfaces are crucial in effecting this interaction. Such behaviour demonstrates that interactions between localised plasmon can be clearly controlled by the geometry of microsphere samples.

To summarise, the microsphere sample geometry allows robust coupling to the plasmon modes of sub-micron spheres in a manner which utilises their periodic

arrangement and does not rely on nano-positioned external coupling devices. Dispersion measurements show that interaction between delocalised surface modes and localised modes is crucial for efficient coupling. Control of the metal thickness in which the spheres are embedded allows the couplings to be tuned, as well as the properties of the localised plasmons to be optimised. Plasmon hopping between neighbouring spheres can be clearly identified, resulting in minibands. Such localised plasmons are useful in a range of applications such as sensors and microlasers, as well as novel matched emitters and absorbers.

6.4 Trench Guided Plasmons

Experiments performed on encapsulated sphere arrays in section 6.3 identified plasmon hopping between neighbouring spheres, leading to the formation minibands in the dispersion. Our collaborator Xiaoli Li at the University of Southampton has fabricated a series of nanovoid structures in linear arrays which guide plasmons in specific geometric directions, forming a plasmon waveguide. To form the waveguide, V-groove trenches with atomically flat walls were fabricated by selectively etching a Si wafer along the (111) plane. Microspheres are then assembled in the trenches, guided by the local geometry and wetting properties of the Si surface. The spheres form a template around which metal is electrodeposited, before being removed to leave a linear nanovoid array. Furthermore, by choice of trench width, both single and multilayer nanovoid arrays can be fabricated.

Preliminary experiments performed by the author reveal that nanovoid trench structures support both localised and propagating modes. Figure 6.8 shows results for single and multilayer arrays, formed in trenches of 1000 and 1500 nm trench width respectively. Dispersion measurements reveal weak but highly dispersive modes, corresponding to plasmon modes propagating along the length of the trenches. The data also reveals highly localised modes, predominant for structures with $\bar{t} > 0.6$. Hopping of localised plasmons between neighbouring spheres can be identified from the presence of *nearly* localised plasmons with mixed Bragg-Mie dispersion, most visible for structures with $\bar{t} \sim 0.5$. Furthermore, whereas light incident on a 2D hexagonal nanoscale void array can couple to plasmon modes at any incident azimuthal angle ϕ to the crystal lattice, in the

6.4 Trench Guided Plasmons

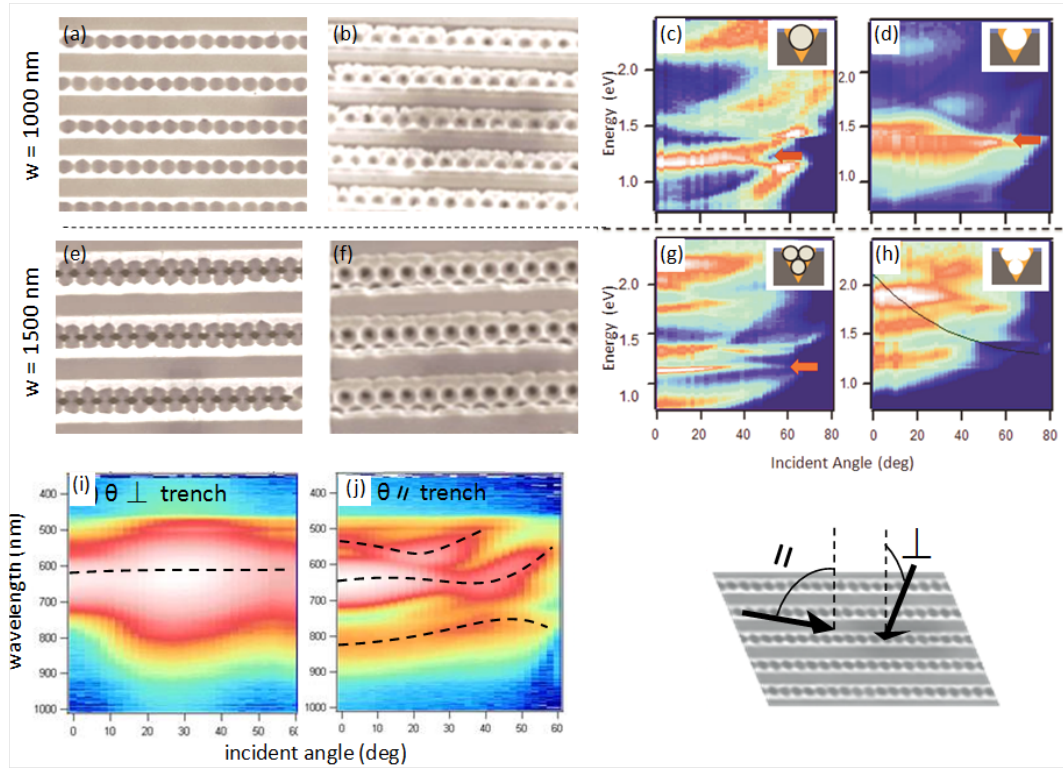


Figure 6.8: *SEM* images of $\bar{t} \approx 0.5$ encapsulated 500 nm spheres in (a) a 1000 and (e) 1500 nm wide trench, (b,f) angled *SEM* with spheres removed. Corresponding dispersion measurements for sphere (c,g) and void arrays (d,h). The black line indicates the calculated dispersion of a Bragg plasmon propagating along the 1D void array. Red arrows indicate localised plasmons. Angle-dependent dispersion of plasmon absorption for light incident (i) across and (j) along the line of the trenches of gold nanovoids of diameter 500 nm in 1490 nm wide trenches. Plasmons (dashed lines to guide eye) do not couple across trenches (flat line), but do propagate along nanovoids.

trench structures only light incident *parallel* to the trenches will couple strongly to plasmon modes, with only weak coupling to localised plasmons by light incident perpendicular to the trenches. This highlights the crucial role of the trenches in guiding and confining the propagating plasmons. Further details of the precise plasmon coupling along the 1D lines of spherical voids are beyond the scope of this thesis and subject to further investigation.

6.5 Hybrid Nanovoids

As discussed in chapter 5, the nanovoid geometry supports very different plasmon modes to metal particles or tips. Spherically-symmetric plasmon modes in the cavity mix with additional rim plasmon modes to produce bonding (lower energy) and antibonding (higher energy) hybridised states with significant field enhancements at the cavity rim. Initial calculations have confirmed that these plasmon modes are dramatically modified by even a small change in the local dielectric environment, for example by coating with another material. Whilst gold is the metal of choice for many plasmonic applications (due to its strong plasmonic properties and ease of fabrication), other transition metals, including nickel, have been investigated for relatively few plasmonic applications. D-band transitions make nickel highly absorbing in the visible wavelength range and hence it supports only heavily-damped surface plasmons. However by fabricating gold-nickel hybrid structures it is possible to experimentally identify the role of precise geometrical features in defining the plasmonic properties of a nanostructure, and create structures with entirely new plasmonic properties. The nanovoid assembly process lends itself ideally to the fabrication of hybrid structures, allowing the comparison of gold rims on nickel voids with nickel rims on gold voids. The results of these experiments give an insight into the complementary roles of field enhancement and absorption, crucial for the optimisation of substrates for applications such as *SERS*.

To fabricate hybrid nanovoid structures, a second stage of electrodeposition is performed during the fabrication procedure described in chapter 3, shown schematically in figure 6.9. The fabrication procedure is identical to that of regular nanovoids up to the point where the first layer of metal is deposited around the sphere template. At this stage, one half of the graded substrate is coated with an insulating paint to isolate it from further electrochemical coating. The sample is then placed in a second plating bath and a uniform thickness of a different metal is deposited around the sphere template and over the first metal layer. Since the polymer spheres remain embedded in the structure, the second metal layer gets plated on the exposed top surface of the nanostructure only. After plating, the sample is sonicated in tetrahydrofuran for 2 hours to completely remove the

6.5 Hybrid Nanovoids

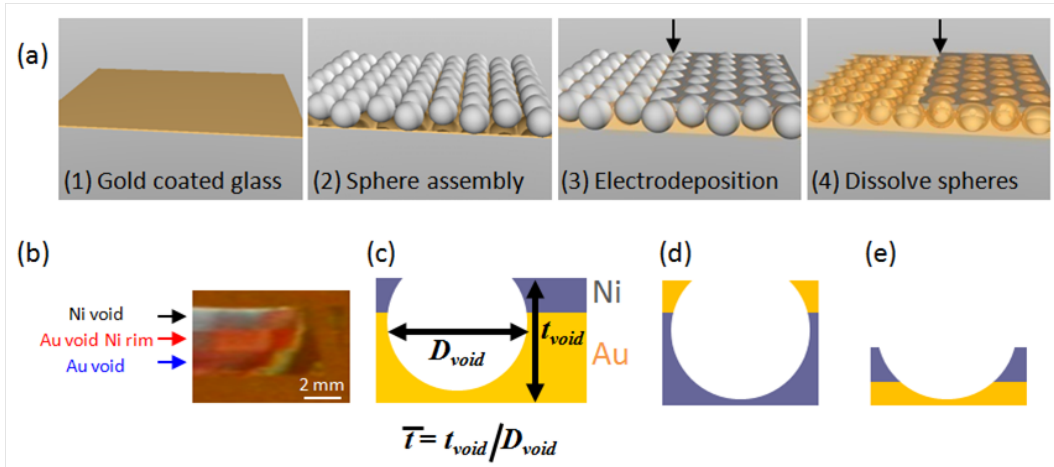


Figure 6.9: (a) Sample fabrication procedure. Electroplating is carried out in two steps to create layers of different metals to yield the hybrid nanovoid structure after dissolution of spheres. (b) Microscope image of a nanovoid structure showing (black arrow) nickel voids, (red arrow) gold voids with nickel rim and (blue arrow) gold voids. (c) Schematic of the nanovoid geometry and definition of normalised thickness \bar{t} . (d,e) Schematic of hybrid structures designed for novel plasmonic and catalytic properties.

sphere template and the insulating paint. Using this procedure, graded gold voids with nickel rims were fabricated. The nickel coating layer can subsequently be etched completely from the structure by immersion and gentle swirling in a 0.5 M solution of H_2SO_4 .

A gold nanovoid sample of sphere diameter $D = 600$ nm and thickness grading, $\bar{t} = 0.3$ to 0.8, is shown in figure 6.10. Initially the sample is plated with two thicknesses of nickel along different longitudinal sections, a thin layer (≈ 10 nm) and a thick layer (≈ 75 nm). Microscope images (figure 6.10(b,f,j)) show the contrast in colouration between the thin and thick nickel strips, highlighted at three key sample thicknesses. *SEM* images confirm nickel plating only on the top surface of the structure and the rim entrance to cavities, with smooth gold clearly visible only within the cavities. This allows the plasmonic properties of rim plasmon modes to be clearly identified and differentiated from plasmons located *within* voids. After the initial experiments were performed, the nickel

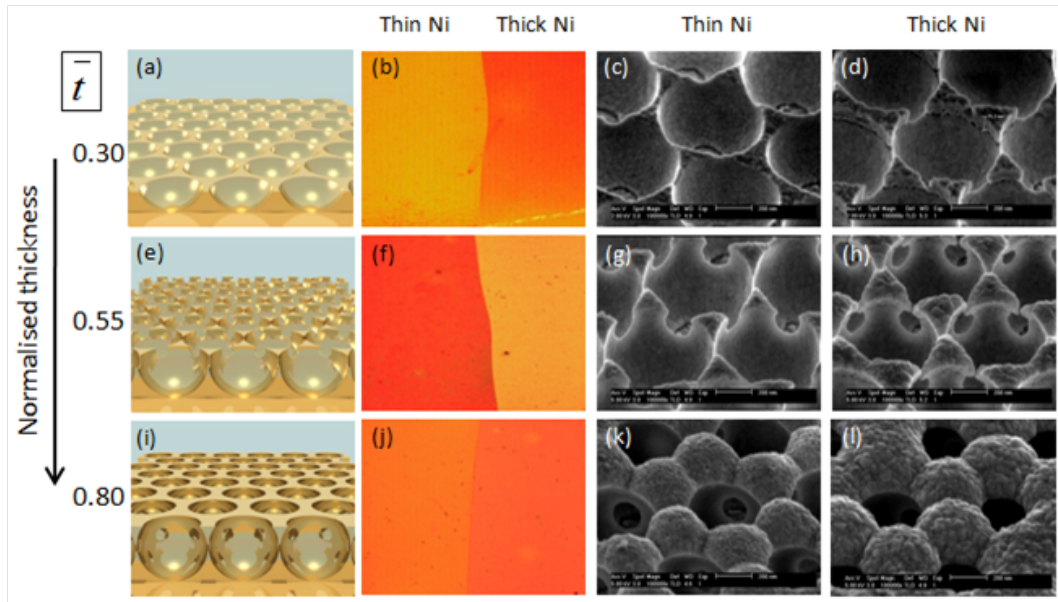


Figure 6.10: (a,e,j) Schematic of gold nanovoids at different normalised thickness, \bar{t} . (b,f,j) Microscope images at $\times 10$ show the resulting color change for each nanovoid structure upon nickel coating. *SEM* images for (c,g,k) thin and (d,h,l) thick nickel coatings.

was completely stripped off the structure by chemical etching, leaving bare gold nanovoids for comparison. Images and spectra recorded using an optical microscope reveal clear differences between the gold and nickel-gold hybrid structures, however they provide only limited information about the plasmon modes responsible for the dramatic colour contrasts observed. As discussed in chapter 5, by comparing angle-resolved reflectivity measurements with calculations, it is possible to identify and label the observed plasmon modes. A pictorial representation of the three different types of plasmon present on these structures is given in figure 5.1.

Angle-resolved reflectivity plots for gold/nickel nanovoid structures of thickness $\bar{t} = 0.55$ are shown as linear colour plots in figure 6.11, where white corresponds to 100% absorption and blue corresponds to 100% reflection. At this thickness nanovoids support three types of plasmon modes: propagating Bragg modes, weak localised modes, and a low-energy tip mode. Therefore by studying

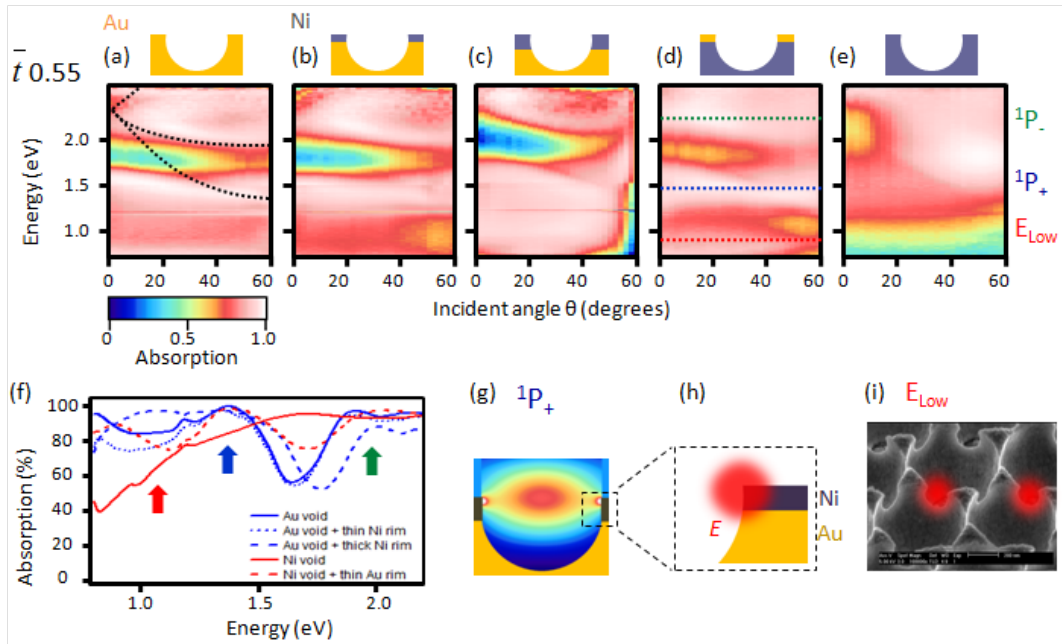


Figure 6.11: (a-e) Angle-resolved reflectivity plots for a series of $D = 600$ nm, $\bar{t} = 0.55$ nanovoid structures of different material compositions. Dashed lines indicate the dispersion of the (black) Bragg plasmon, (green) $^1P_-$, (blue) $^1P_+$ and (red) low-energy tip plasmons. (f) Extracted absorption summed over 0 to 50° incident angles for comparison with experiments carried out with a $NA = 0.85$ objective [discussed later]. Arrows indicate the energy of the plasmon modes. (g) Electric field distribution of the $^1P_+$ mode and (h) schematic of $^1P_+$ field distribution on a hybrid rim. (i) SEM of coated structure with a representation of the low-energy mode field distribution in red.

the angle resolved reflectivity plots it is possible to identify the influence of the top metal surface and cavity rim on these three types of plasmon mode.

Figure 6.11(a) shows data for a gold-only structure which supports several plasmon modes. A dispersive plasmon mode centered at 2.1 eV is identified as the Bragg plasmon, the black dashed lines show the calculated dispersion. Localised modes at 1.5 eV and 2.1 eV are identified as the $^1P_+$ and $^1P_-$ modes respectively, as described in chapter 5. The $^1P_-$ and Bragg plasmon modes are nearly degenerate, resulting in overlapping dispersion bands. Finally, a third

6.5 Hybrid Nanovoids

localised mode is apparent at the low-energy part of the spectra around 0.7 eV. This mode is identified as the low-energy mode associated with triangular pillar features which are supported on this structure, as described in section 5.4. Figure 6.11(i) shows an illustration of the field profile of this mode overlaid on an SEM of the structure and shows that the location of this mode at the cavity rim means that it will be strongly influenced by the nickel coating layer. The dispersion of the three localised plasmon modes is indicated by the dashed lines in figure 6.11(d).

Figure 6.11(b) shows data for the gold void coated with a ≈ 10 nm layer of nickel. The nickel is extremely thin and hence only weakly modifies the observed plasmon modes. However, coating the gold structure with a 75 nm thick layer of nickel strongly modifies the plasmonic modes (6.11(c)). The nickel refractive index blue-shifts the observed plasmon modes, shifting the dispersive Bragg plasmon to 2.4 eV and the $^1P_+$ mode up to 1.7 eV. Also the low-energy tip mode is strongly blue-shifted and both increases in absorption strength and absorption linewidth.

Figure 6.11(d) shows a nickel structure coated with a 75 nm layer of gold. The dispersion of the localised plasmon modes is indicated by the dashed lines. This structure exhibits weaker but similar plasmonic features to the gold only structure (figure 6.11(a)), indicating that the localised $^1P_+$ and $^1P_-$ rim modes are only subtly influenced by the supporting void structure. Figure 6.11(e) shows the nickel-only structure which exhibits very different plasmonic features to the gold-only structure. The $^1P_+$ mode increases in absorption strength and has a significantly broader linewidth, indicative of increased damping and re-radiation for the nickel only structure. Also the low-energy tip mode completely disappears from the data. These results indicate that it is the metal composition of the cavity rim which determines the plasmonic modes of the structure, with the void effectively acting as an antenna, helping to couple incident light to the cavity rim.

Angle-resolved reflectivity for structures of thickness $\bar{t} = 0.8$ are shown in figure 6.12. At this thickness the localised $^1P_+$ and $^1P_-$ modes dominate the spectra. Bragg modes are weakly supported on the top metal surface, indicated by the anti-crossing observed where the Bragg dispersion crosses the $^1P_+$ mode dispersion. Since the triangular pillar features have now joined together, the low

6.5 Hybrid Nanovoids

energy tip mode is no longer present. Therefore by investigating $\bar{t} = 0.8$ structures it is possible to determine the influence of the structure rim on the localised $^1P_+$ and $^1P_-$ modes, removing the influence of mode-mixing with either the Bragg modes or the low-energy tip mode.

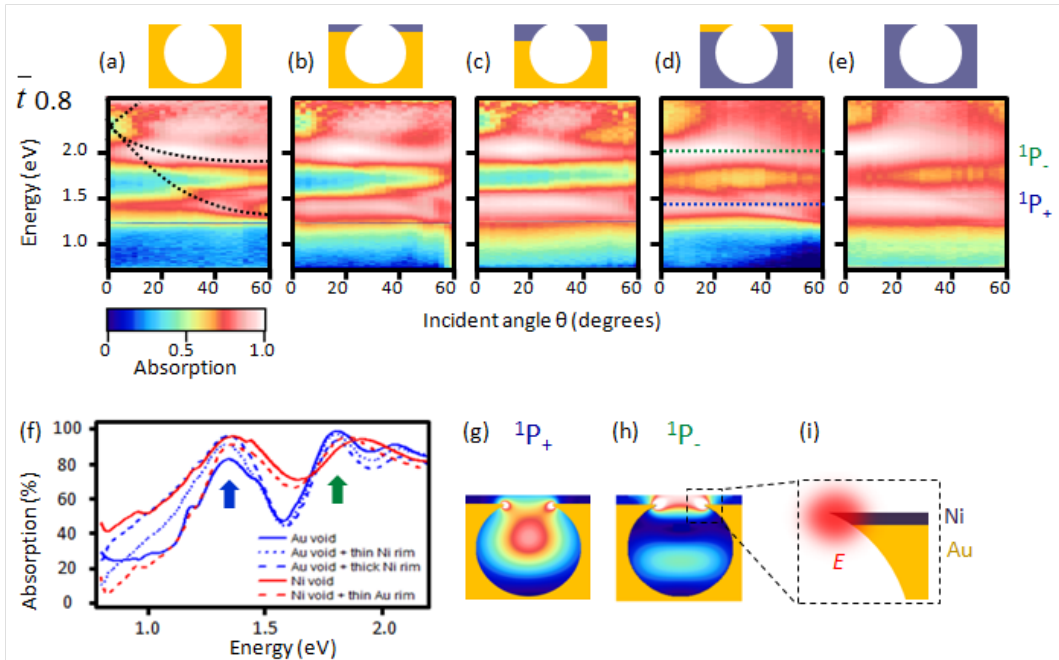


Figure 6.12: (a-e) Angle-resolved reflectivity plots for $\bar{t} = 0.8$ nanovoid structures. Dashed lines indicate the dispersion of the (black) Bragg plasmon, (green) $^1P_-$, (blue) $^1P_+$ and (red) low energy mode plasmons. (f) Extracted absorption summed over 0 to 50° incident angles showing the change in absorption strength of the $^1P_+$ and $^1P_-$ modes with rim coating. Arrows indicate the energy of the plasmons. (g) Electric field distribution of the $^1P_+$ mode and (h) $^1P_-$ mode. (i) Schematic of $^1P_-$ field distribution on a hybrid rim.

Figure 6.12(a) shows data for the gold-only structure which supports strong coupling to the $^1P_-$ mode through mixing with a weak Bragg plasmon propagating on the corrugated top metal surface (with calculated dispersion shown by the black dashed lines). The $^1P_+$ mode is more weakly coupled by comparison, as highlighted in the extracted spectra summed over incident angles from 0 to 50°

6.5 Hybrid Nanovoids

shown in figure 6.12(f). The dispersion of the localised modes is indicated by the dashed lines in figure 6.12(d).

Figures 6.12(b,c) show that upon coating the gold structure with nickel, the absorption strength and linewidth of the $^1P_+$ and $^1P_-$ modes is increased (figure 6.12(f)). Since these plasmon modes are localised at the cavity rim, they are highly sensitive to the precise material composition of the cavity rim, and coating with nickel results in increased damping (and therefore absorption), shown schematically in figure 6.12(i). For the gold structure with a 75 nm layer of nickel (figure 6.12(c)) absorption by the $^1P_+$ and $^1P_-$ modes is almost identical in strength as for a purely nickel structure (figure 6.12(e)). However these modes are significantly broadened for the nickel-only structure due to increased coupling from the rim modes down into the absorptive nickel void.

For the nickel void with a gold rim (figure 6.12(d)) the absorption strength of the $^1P_+$ and $^1P_-$ modes is reduced compared to the purely nickel structure (figure 6.11(e)), and is similar in strength to the gold structure with a thin nickel rim (figure 6.12(b)). This indicates that the absorption strength of the $^1P_+$ and $^1P_-$ modes strongly correlate to the metal composition of the rim. This can be understood more clearly by considering the field distribution of these modes. Figure 6.12(i) shows a schematic of these rim plasmon modes on a coated nanovoid rim. In this schematic, although the mode is mostly supported on the nickel rim, a significant proportion of the field also penetrates into the nearby gold. Therefore we expect the absorption properties of the $^1P_+$ and $^1P_-$ modes to be a complex function of the thickness of the two metals, the sharpness of the rim and the precise structure thickness \bar{t} . [Further calculations and experiments are on-going.]

In summary, by selectively coating the nanovoid structure with a thin layer of nickel the coupling strength, energy and linewidths of the plasmon modes are modified. Dispersion measurements identify the precise geometrical location of plasmon modes on the cavity rim and reveal the subtle relationship between plasmon field distributions and light absorption. This information is crucial for the optimisation of nanovoid substrates for *SERS*, the subject of chapter 7.

6.6 Conclusions

This chapter has described several techniques for manipulating the energy, absorption, coupling and field distribution of plasmons on nanovoids. Firstly, the effect of the refractive index of the dielectric top layer has been shown to strongly alter the plasmon dispersion. Both Bragg and Mie plasmons behave in a predictable manner with changing refractive index, and the understanding gained is crucial for the interpretation of *SERS* measurements performed in solution. Secondly, by fabricating nanovoids in linear arrays it is possible to guide plasmons in specific directions, creating a plasmon waveguide. Finally, by fabricating hybrid nanovoids composed of multiple metals it has been possible to experimentally verify the geometrical location of the plasmon modes responsible for the strong plasmonic properties of the nanovoid geometry. The energetics of plasmon modes located on the cavity rim are shown to be strongly dependent on the local dielectric environment, and by coating the gold structure with a thin layer of nickel it is possible to dramatically tune the absorption and coupling properties whilst maintaining the plasmon field distribution. Nanovoid rim plasmon modes have been shown to be relatively insensitive to the supporting cavity structure, suggesting it is straightforward to fabricate hybrid nanovoid structures with improved plasmonic properties. In chapter 7 the *SERS* properties of hybrid nanovoids are investigated, revealing the relationship between absorption, coupling and *SERS* signals.

Chapter 7

Surface Enhanced Raman Spectroscopy on Nanovoids

7.1 Introduction

Many situations require the detection of small numbers of molecules in varying environments, for example to identify contaminants in river water or to detect explosives in the postal system. Surface enhanced Raman spectroscopy (*SERS*) is a very selective molecular finger-printing technique, in which the inelastic scattering of a photon is measured to reveal the vibrational modes of a target molecule. The technique is capable of detecting single molecules, however the initial promise of *SERS* has largely remained undelivered due to a lack of reproducible plasmonic substrates optimised at *SERS* wavelengths. Nanovoid structures show tremendous potential as *SERS* substrates owing to their ease of manufacture and tunable plasmon modes. A comprehensive understanding of the role of different types of plasmons in the enhancement process is essential in order to optimise substrates for specific *SERS* applications. This chapter presents a systematic investigation of the *SERS* properties of nanovoid substrates. Experiments first identify the *specific* plasmon modes responsible for *SERS* and then investigate the relationship between absorption, coupling and *SERS* signals.

7.2 Raman Spectroscopy

The Raman effect, named after its discoverer C.V.Raman is, in essence, the inelastic scattering of light by molecules. Figure 7.1 shows a schematic representation of the associated energy levels involved in this scattering process. The majority of photons incident on a molecule will undergo Rayleigh scattering; an elastic scattering mechanism where the outgoing photon leaves with the same energy as the incident, but in a random direction. In Raman scattering, however, the scattered photon can lose or gain energy to the molecules internal vibrational levels, known as Stokes and Anti-Stokes transitions respectively. Intuitively, the process can be considered as a change in polarization of the molecules electron cloud when interacting with the oscillating electric field of an incident photon. Upon illumination, the molecules electron cloud will tend to vibrate at the frequency of the incident photon, modulated by the intrinsic molecular oscillation. Scattering proceeds via an intermediate electron state, described as a virtual state since it is not a permanent excited state of the molecule. Raman scattered photons are linearly shifted in frequency by the molecules vibrational frequency (analogous to sidebands in radio communications), allowing the straightforward extraction of the vibrational finger-print of the molecule.

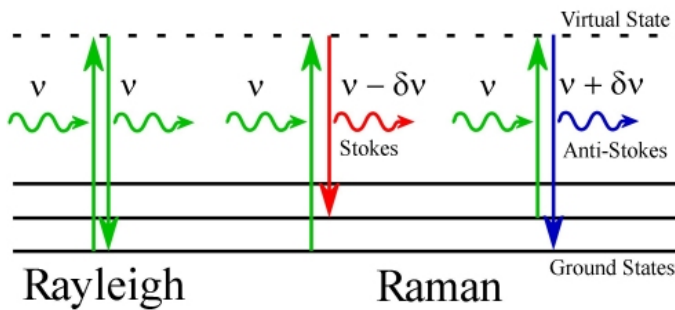


Figure 7.1: Energy levels involved in Rayleigh, Stokes and Anti-Stokes scattering. All transitions pass through the virtual state(1).

However the probability of Raman scattering is very low, with cross-sections of the order of $10^{-30} \text{ cm}^2/\text{molecule}$, and hence *SERS* signals are extremely weak.

The signal can be increased by several orders of magnitude if the incident photon is resonant with an electronic state of the molecule, a process referred to as resonant Raman scattering. Unfortunately the application of this technique is constrained to a limited number of molecules due to the necessity to match the incident laser wavelength to specific electronic transitions. The situation changed in 1974, when M.Fleischman and colleagues⁽⁸²⁾ at the University of Southampton observed massively enhanced Raman signals from molecules on roughened silver surfaces. Fleischman initially attributed the extraordinary large signals to the increase in surface area created by electrochemical roughening. However it was quickly realised that surface area alone could not account for increased Raman signal, and that large local electric field enhancements associated with surface plasmons were principally responsible for the massive signal enhancements observed. In the succeeding 30 years a wide variety of plasmonic structures have been fabricated which show *SERS* enhancements. These structures include nanotriangles⁽⁸³⁾, nanorings⁽⁸⁴⁾, spherical nanoshells⁽⁸⁵⁾, two dimensional gratings⁽⁸⁶⁾, and of course the nanovoids presented in this thesis.

7.3 SERS on Nanovoids

Understanding the precise plasmonic properties of the nanovoid geometry is crucial to the investigation of the *SERS* enhancement process. Nanovoids support a variety of plasmon modes which can be selectively engineered by the structure geometry. By careful choice of structure geometry and composition, substrates have so far been optimised for *SERS* in both the ultraviolet (*UV*)⁽⁸⁷⁾ and the near infrared (*NIR*)⁽⁸⁸⁾. Nanoparticles in close proximity or tips are the structures of choice for most *SERS* studies since the plasmon modes are well characterised and large *SERS* enhancements can be easily generated at *hotspots* on substrates. The contrasting properties of nanoparticles and nanovoids substrates (compared in figure 7.2) essentially depend on how the opposite curvature of their metal surfaces modifies the field energetics. For nanovoids, charge distributions on the walls of the void cavity provide the electric field distributions which constitute the plasmon modes. Since the fields are concentrated inside the dielectric cavity (as

opposed to around the metal of a nanoparticles system), there is reduced damping in the void structure. The field enhancement depends on the contribution of both re-radiation (optical loss) and damping (absorption loss) and in nanovoids is found to result in longer plasmon confinement times (giving narrower plasmon linewidths than for nanoparticle plasmons) and therefore stronger excitation of molecules for *SERS*.

The broad wavelength tunability of plasmons in nanovoids makes these structures ideal for studying *SERS* enhancement by specific modes, where fields are required at both the incoming and outgoing *SERS* wavelengths. Larger (micron diameter) nanovoid structures support many higher order plasmon modes, each with unique field distributions, thereby allowing the investigation of *SERS* from molecules at several distinct locations within a single geometry. Furthermore the open nanovoid geometry can be wetted, allowing the study of *SERS* in solution(89; 90). The wide plasmonic tunability of nanovoids compares favourably with popular nanoparticle-based nanotriangle and AgFON films(91) which are fabricated by vacuum deposition. The *SERS* enhancements of these nanoparticle-based substrates has been identified from correlation with the spectrally-broad localized surface plasmon resonances from *hot spots*(83). By contrast, the plasmonic resonances of nanovoids are typically spectrally narrow, and can be simply tuned by the structure geometry, allowing the precise correlation between structure extinction and *SERS* enhancement to be extracted. Here, the correlation between *SERS* enhancements and the plasmon modes responsible for them are characterised as a function of cavity geometry and for a range of laser excitation wavelengths in both air and solution.

Angle-resolved spectroscopy performed using the automated goniometer allows the full spectral and angular dispersion of the plasmon modes to be mapped with high spatial resolution, for direct correlation with *SERS* signals. For comparison with *SERS* results obtained using microscope systems with $\times 20$ objectives, dispersion plots are integrated over a range of incident angles from 0 to 30° to produce position-resolved absorption maps of the substrates (logged colour plots, black corresponds to 100% reflectivity, yellow to 100% absorption). By comparing these maps to equivalent calculations of the absorption and electric near field distributions of the structure, it is possible to identify the plasmon

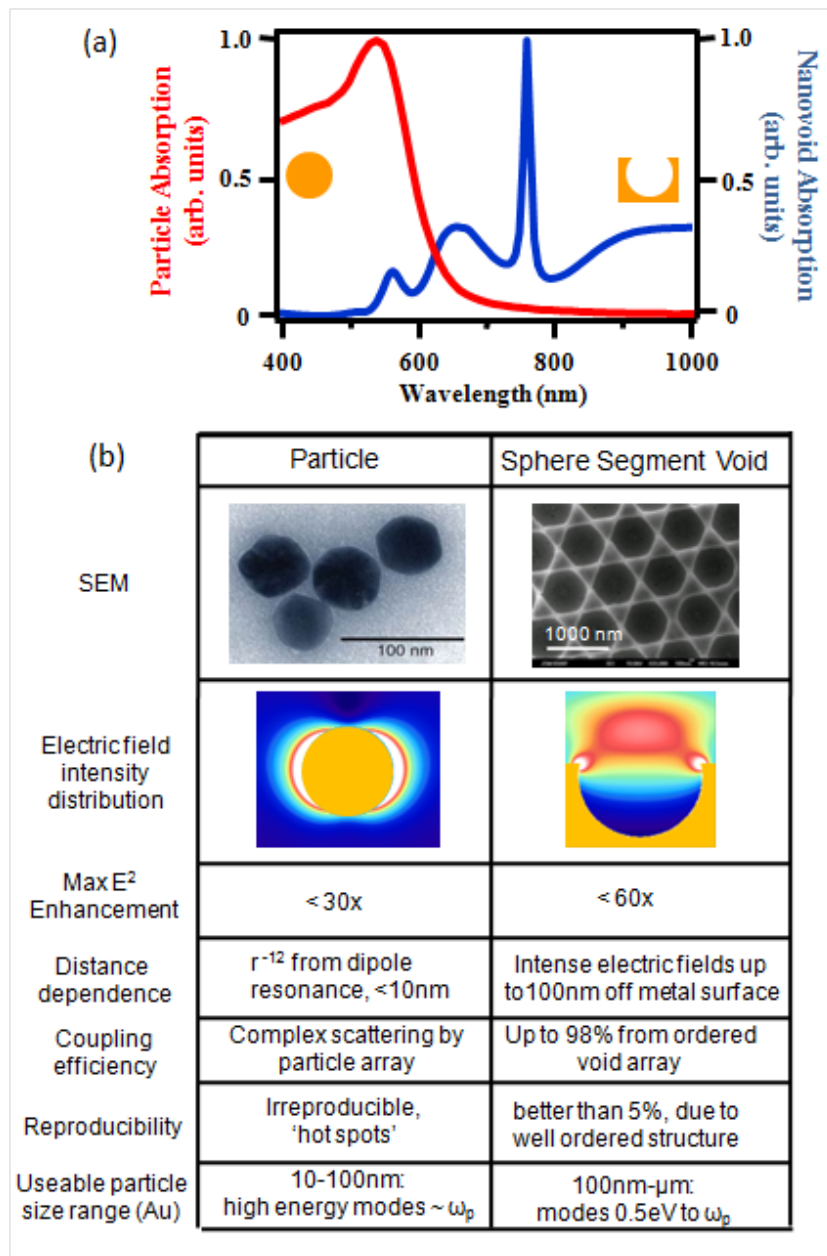


Figure 7.2: (a) Calculated absorption cross section for (red) 50 nm diameter gold nanoparticle and (blue) 600 nm diameter gold nanovoid, normalised to the peak absorption. (b) Comparison of particle and void properties. Electric field intensity distributions show that the nanovoid geometry supports radically different plasmon modes to metal particles. The negative curvature of the cavity surface (yellow) pushes the electric field out of the metal. Localised plasmon modes are not supported for frequencies above the plasmon frequency ω_p .

modes responsible for *SERS* enhancements. The molecule of choice for *SERS* studies is benzenethiol, a benzene ring with a sulphur atom attached to one of the carbon bonds. A typical Raman spectrum is shown in figure 7.3 with the nature of the different observed transitions shown. It is customary for Raman spectra to be plotted in terms of the Raman shift:

$$\text{Raman Shift}(\text{cm}^{-1}) = \frac{(E_{\text{laser}} - E_{\text{Raman peak}})}{100hc} \quad (7.1)$$

where E_{laser} and $E_{\text{Raman peak}}$ are the energies of the excitation laser and the observed energy of the spectra respectively. In this thesis *SERS* spectra will also be plotted against energy in most cases.

For all measurements, benzenethiol molecules were adsorbed onto the substrate by immersion in a 10 mM ethanolic solution for 1 hour, before being thoroughly rinsed with ethanol. Raman spectra collected from nanovoid samples do not show an SH peak (associated with the free thiol). This confirms that the benzenethiol forms a thiolate (metal-sulfur) bond to the gold and results in a monolayer of molecules. A cell was constructed to allow reflectivity measurements to be performed in solution, and the same cell used for the *SERS* measurements in air. *SERS* measurements were carried out on graded nanovoid samples using laser wavelengths of 633, 785 and 1064 nm. Raman spectra with a 633 nm laser were recorded with a Renishaw 2000 Raman microscope. Raman spectra with the 785 nm laser were recorded on a Perkin-Elmer RamanStation 400. Finally, Raman spectra with a 1064 nm laser were acquired with a Perkin-Elmer System 2000 FT-Raman instrument. *SERS* spectra were recorded at uniformly spaced intervals along the length of graded samples, for void diameters from 400 to 800 nm. The peak intensities presented have been calculated after subtracting the background from the spectra, as is common practice for these measurements.

A single graded nanovoid substrate can exhibit intense *SERS* signals for a wide range of incident laser wavelengths and at multiple locations along a substrate. The *SERS* signal for benzenethiol adsorbed on a graded 600 nm diameter gold nanovoid substrate is plotted as a function of thickness \bar{t} and overlaid on the corresponding absorption map in figure 7.4(a). The intensity of the 1571 cm^{-1} Raman scattered peak, corresponding to the ring stretching mode of benzenethiol,

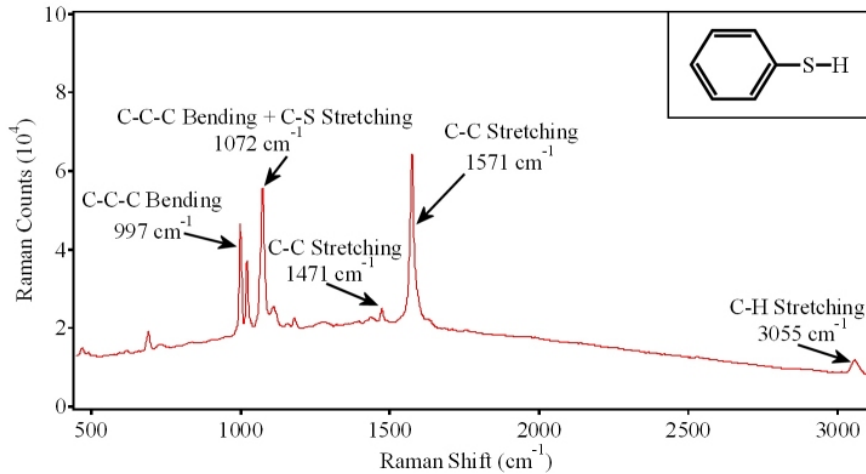


Figure 7.3: Image showing a typical *SERS* spectra for benzenethiol (shown in the inset), the different peaks correspond to different molecular modes(1).

is extracted after background subtraction and plotted for each laser wavelength (*SERS* intensity is plotted as the marker size for each film thickness). The absorption profile reveals several distinct modes, which tune rapidly in frequency with increasing thickness \bar{t} of metal. The maximum *SERS* enhancements are observed when the incident laser is in resonance with a plasmon mode. The broad linewidth of these modes ensures that the plasmon fields and molecules excited are identical at the incoming and outgoing photon wavelengths, a condition required for maximum *SERS* enhancement.

Calculations identify that these modes are the ${}^1P_+$ (bonding) and ${}^1P_-$ (anti-bonding) modes, shown in figure 7.4(b) for one sample thickness. These modes support intense fields located directly at the metal rim, and provide efficient excitation of molecules at the metal surface for *SERS*. However, the calculations are for a single isolated void, which leads to several key differences between the calculated and experimentally realised absorptions. First, in the experiment the periodic array of voids supports highly delocalised Bragg plasmons which contribute to absorption for structures with normalised thickness $\bar{t} < 0.5$, but do not give rise to *SERS*. Second, windows between neighboring voids give rise to a tip structure (shown in figure 7.4(c,d)), not accounted for in the simulations. This tip structure supports a low energy mode which is seen to rapidly tune to

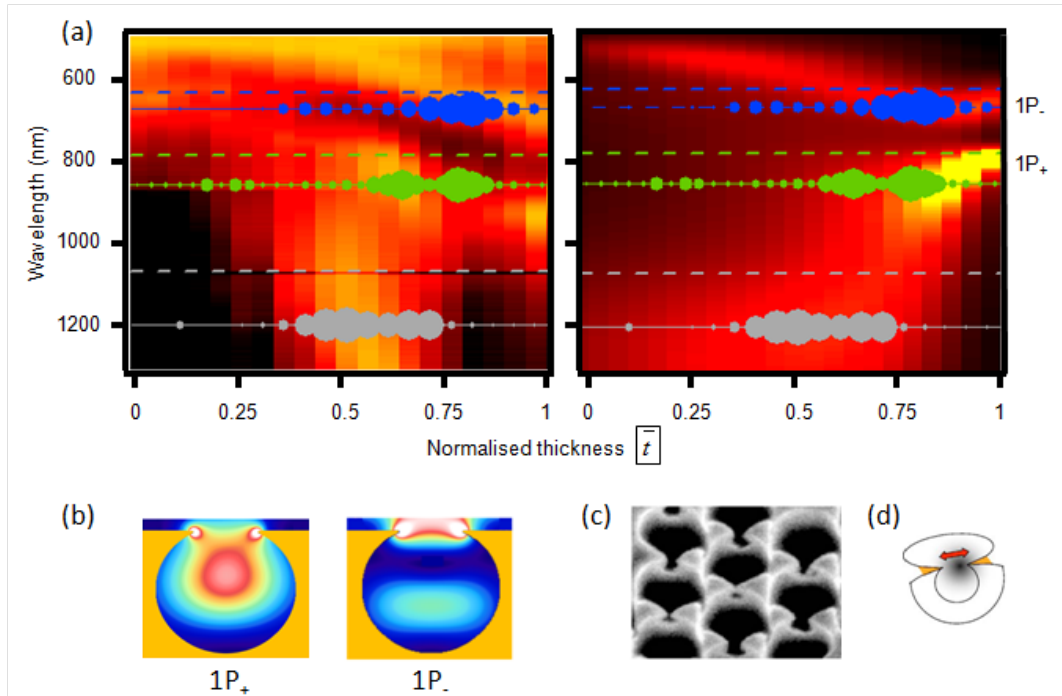


Figure 7.4: (a) Experimental (left) and calculated (right) 600 nm diameter nanovoid position resolved absorption map with peak *SERS* signal for laser wavelengths of 633, 785 and 1064 nm overlaid on each. Dashed lines are incident laser wavelength, and solid lines are for the 1571 cm^{-1} Raman lines at their absolute wavelength red-shifted from the laser. The size of the circles are proportional to the intensity of the *SERS* peak and are relative to each other only for each respective laser excitation. (b) Fields of identified modes. (c) *SEM* showing experimentally realised structure and (d) schematic of the low-energy tip mode.

7.3 SERS on Nanovoids

IR wavelengths with increasing sample thickness, and gives rise to strong *SERS* signals.

These results highlight the fact that *SERS* enhancement does not necessarily correlate to absorption by plasmons, but has a complicated dependence on both the geometry of the nanovoid, the plasmon field distribution and the coupling conditions of each mode. Only electric fields normal to the metal surface give rise to absorption by the metal. However there are scattered and radiated components to the extinction measurements of nanovoid substrates which contribute to *SERS* enhancement(59). A balance is generally expected between more radiative modes which have better out-coupling of the in-elastically scattered plasmons, compared to more localised modes which have larger plasmon field confinement at the metal-molecule interface. Experiments reveal that absorption is indeed by far the greatest contribution to extinction by these structures, and shows good correlation with *SERS* in figure 7.4(a). While quantitative comparison of the enhancement due to different modes at the same position on a sample is complicated by the different efficiencies of the three very different Raman spectrometers employed in this study, similar *SERS* enhancements are found for each plasmon type (except for Bragg plasmons which show little *SERS* enhancement). This is broadly confirmed by calculations which track the optical field averaged around the metal surface and the input and output plasmon coupling. Hence, for nanovoids, all the localised plasmon resonances are effective in providing efficient *SERS*.

Since the plasmon modes and corresponding *SERS* enhancements tune as a function of void diameter and metal thickness \bar{t} , it is possible to systematically investigate and identify the optimum structure for *SERS* at a particular excitation wavelength. *SERS* from benzenethiol molecules was investigated on nanovoid substrates with sphere diameters 400, 500, 600 and 800 nm, (figure 7.5). Again, the maximum *SERS* enhancement is observed when a plasmon mode is resonant with either the incoming laser or outgoing scattered wavelength. Both the $^1P_+$ and $^1P_-$ modes, observed for $\bar{t} = 0.5$ (highlighted with triangles to guide the eye) are seen to provide significant *SERS* enhancements. Variations in the position dependence and final energies of these modes are due to variation in gradation of the samples. Further modes not explicitly highlighted are identified

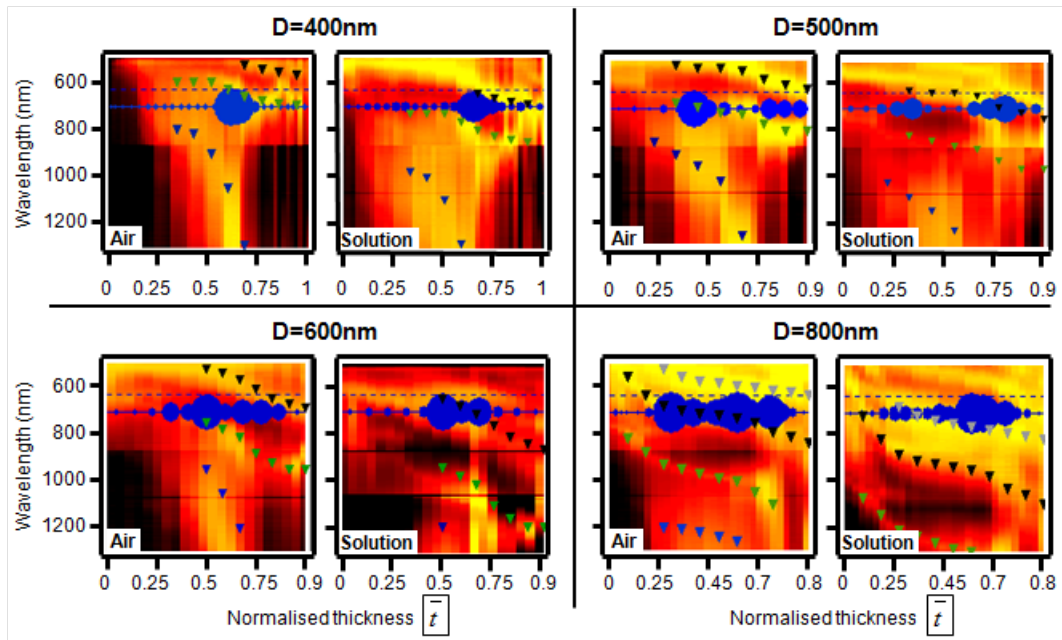


Figure 7.5: Position resolved absorption maps with the *SERS* overlaid in blue, spot size corresponds to signal strength. The plasmon modes indicated by triangles are; (blue) low energy mode, (green) $^1P_+$, (black) $^1P_-$, (grey) 1D . The plotted mode energies are extracted in air and scaled for the solution refractive index. A dashed blue line indicates the 633 nm laser input.

as propagating Bragg plasmon modes below $\bar{t} = 0.5$, which again do not give rise to intense *SERS*, and higher order localised modes above $\bar{t} = 0.5$. It is clear from the results in figure 7.5 that the same laser wavelength will produce strong *SERS* signals from a different (but potentially spatially overlapping) group of molecules on nanovoid samples with different thicknesses. This can be seen from the double resonance observed in figure 7.5(c,d,e,g) when translating across the graded sample. The data also shows that resonance with plasmons either at the incoming laser or at the outgoing scattered wavelength can be effective at producing *SERS* enhancements. Nevertheless, such spatial selection through choice of the nanostructured geometry and wavelength can potentially be discriminated by selective tagging studies (ongoing) where molecules are attached to only specific regions of the nanostructure.

The *SERS* measurements were then repeated in water (figure 7.5(b,d,f,h)) to obtain insight into *in – situ* solution measurements(90). Plasmon modes tune to longer wavelength with a shift proportional to the effective increase in refractive index at the metal/dielectric interface, here $n = 1.3$ for water, (see section 6.2). Upon wetting a given cavity, the plasmons tune in wavelength and different modes are now in resonance with the incident laser light, leading to different *SERS* intensity profiles with respect to position on the graded samples. For the 400 nm diameter cavity the $^1P_+$ mode is responsible for *SERS* enhancement in air, while the $^1P_-$ mode produces the enhancement in water. Similar tuning is observed for the 500 and 600 nm samples, but for the 800 nm sample, both the $^1P_+$ and 1D modes contribute both in air and water. It can also be seen that for larger structures ($D = 800$ nm) localised plasmon modes *do* exist for structures of normalised thickness $\bar{t} < 0.5$ which give rise to *SERS* with a 633 nm laser. However, as the void diameter is increased further the fields near the surface are weaker due the higher order modes being supported at these energies. Figure 7.5 confirms that a wide range of localised plasmons types give rise to *SERS* and that their enhancements can be manipulated by the choice of void diameter, metal thickness \bar{t} , and the refractive index of the dielectric medium surrounding the voids. These results show that the optimum structure geometry for *SERS* enhancement is different for each laser wavelength.

The recorded *SERS* signals (normalised to incident laser power and collection times) are always found to be 5 - 10 times stronger in air than in water. For comparison, experiments performed on a silicon wafer with a coverslip in water showed a 50% loss of Raman signal with the 633 nm laser and 25% loss with the 785 nm laser. Therefore, the decrease in *SERS* intensities for nanovoids in water is not fully explained by either loss from the coverslip and aqueous cell used or by any change in damping of the plasmons (which should reduce as the modes tune to lower photon energy). It is also not expected that the relative coupling strength of the nanovoid plasmons would change since all plasmon modes on the surface tune similarly. A factor of 3 may be accounted for by the increased refractive index of water ($n = 1.3$) which reduces the electric field responsible for *SERS* by n^4 . However a significant consequence of changing the plasmon modes responsible for *SERS* signals (by changing the refractive index of the dielectric) is that *SERS* signals will originate from different molecule populations within the void, contributing to changes in the *SERS* signal (as clear from the field profiles in figure 7.4(b)). However without an understanding of the precise *SERS* signals to be expected from each plasmon mode, speculation about the changes in absolute *SERS* signals expected for *in – situ* measurements remains at best qualitative.

In summary, comparing plasmon absorption with *SERS* enhancements as a function of nanovoid size and metal thickness allows the identification of the optimum geometries for *SERS* at a range of different laser wavelengths and in different media. *SERS* signals show direct correlation to the plasmonic resonances of the structures. However it is clear that not all plasmon modes excite *SERS* with equal efficiency. It is therefore necessary to perform a more targeted investigation into the precise properties of plasmon modes which determine the obtained *SERS* signals. In particular, it is crucial to understand the relationship between plasmonic absorption, field distributions and *SERS* signals; a problem which can be directly investigated using hybrid nanovoids.

7.4 SERS on Hybrid Nanovoids

The experiments performed in section 7.3 reveal that localised plasmons are responsible for the large *SERS* signals observed from nanovoid structures. However not all localised plasmons generate *SERS* signals with equal efficiency. The accepted electromagnetic theory(92; 93) of *SERS* indicates that signal strength is proportional to energy density at the molecule ($SERS \propto E^4$). Thus experimentally recorded *SERS* signals are a convolution of the time-averaged electromagnetic enhancement factor with the efficiency of coupling into and out of a plasmon mode, and are therefore sensitive to both the radiative and absorptive properties of the mode. As shown in chapter 6.5, by coating a gold nanovoid structure with an absorptive metal such as nickel, it is possible to modify the plasmonic properties of the structure. It was also shown that plasmon modes located at the cavity rim determined the overall absorption characteristics of the 600 nm diameter gold nanovoid structure. Starting from an initially gold rim, as the fraction of nickel was increased, the absorption strength and linewidth by the rim plasmon modes was seen to increase. Therefore using hybrid nanovoid structures, it is possible to identify experimentally the correlation between plasmon absorption, coupling strength and *SERS* signals.

The fabrication of hybrid nanovoid structures is described in chapter 6.5. A series of measurements were performed on the hybrid nanovoid structures to investigate the relationship between structure composition, plasmonic properties and *SERS* signals. Measurements were performed on gold only and nickel only voids, and on structures consisting of gold rims on nickel voids and nickel rims on gold voids. As before benzenethiol was used as the probe molecule throughout. Figure 7.6(a) shows the absorption map for a gold nanovoid structure with *SERS* peak intensities overlaid in blue. Equivalent maps for all structures (not shown) show similar plasmon mode evolution and *SERS* dependence with thickness, \bar{t} , but with the absorption strengths and linewidths as presented in figure 6.12(f). The absorption map represents the spectral absorption (summed over incident angles from 0 to 50° which are equivalent to those collected by the $\times 100$ microscope objective used for *SERS* measurements) taken at uniformly spaced intervals along the graded nanovoid sample. *SERS* was performed with 633 and 785 nm lasers

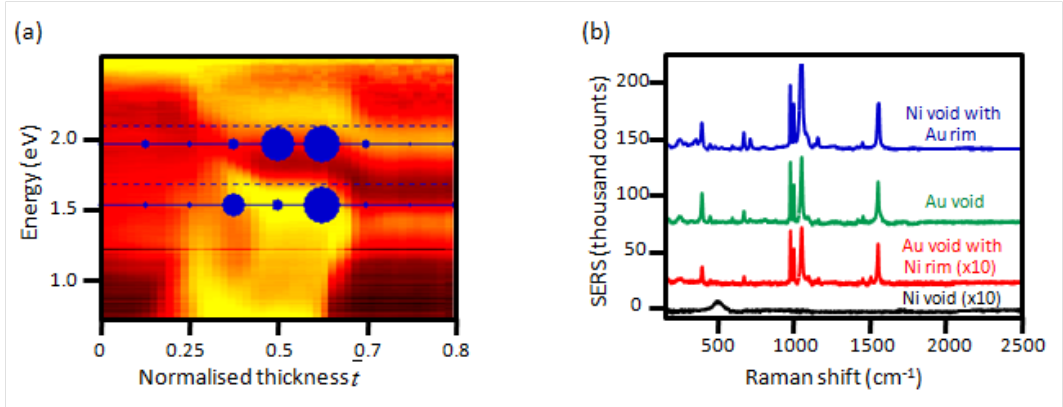


Figure 7.6: (a) Absorption map for $D = 600$ nm gold nanovoid structure graded in thickness \bar{t} , with *SERS* intensity overlaid in blue, with marker size as the magnitude of the $1571\text{ }cm^{-1}$ line. (b) *SERS* spectra for 785 nm laser excitation on gold, gold void/nickel rim and nickel void/gold rim structures of thickness $\bar{t} = 0.8$. The gold void with thicker nickel rim and the nickel-only structures show no observable *SERS* signals.

for a single extended scan (10 s integration time) for all samples. Dashed lines in figure 7.6(a) indicate the incident laser wavelength and solid lines are at the absolute wavelength for the $1571\text{ }cm^{-1}$ Raman lines red-shifted from the laser. The marker size on the plot is proportional to the intensity of the *SERS* peak at each position and is normalised to the maximum *SERS* intensity obtained with each laser. *SERS* signals are strongly dependent on the normalised thickness, \bar{t} , with the maximum enhancement observed whenever the incident laser is in resonance with a localised plasmon mode.

The absorption map reveals several distinct modes, which tune rapidly in energy with increasing thickness. Comparison with calculations and the angle-resolved reflectivity plots of figures 6.11 and 6.12 show that the maximum *SERS* enhancement is provided by the $^1P_+$ and $^1P_-$ modes which are in resonance with the incident lasers for structures of thickness \bar{t} from 0.4 to 0.8. The gold only structure and the nickel void with a gold rim give strong *SERS* signals, however the nickel-only and gold void with nickel rim give negligible *SERS* signals (figure 7.6(b)). Although the nickel layer blue-shifts the plasmon resonances slightly with

respect to the incident laser, previous experiments have shown *SERS* signals to be relatively insensitive to small changes in the resonance energy of the spectrally broad $^1P_+$ and $^1P_-$ modes. Therefore the major factor determining the reduction in *SERS* strength is the interplay between absorption and radiation provided by the nickel-coated rims.

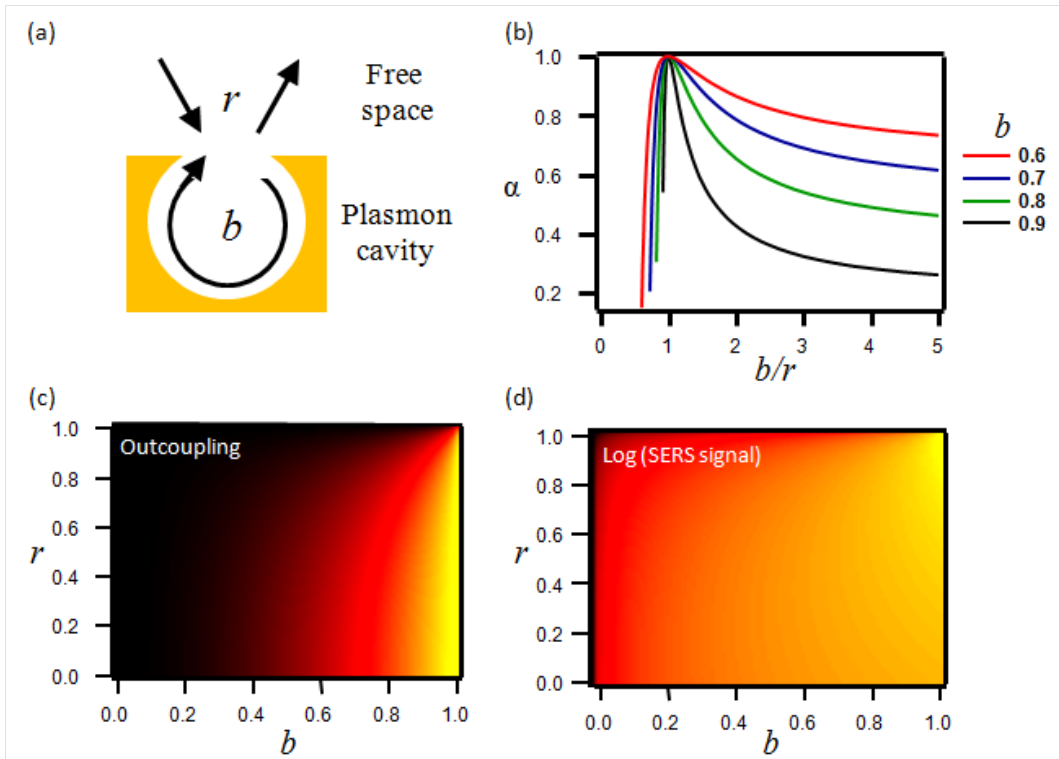


Figure 7.7: (a) Schematic of the resonant plasmon cavity model, where r is the fraction of incident light reflected and b is the field surviving a single round-trip pass of the cavity. (b) Absorption (α) dependence on the cavity parameters b and r as described by equation 7.2. (c) Photon outcoupling (\mathcal{F}_{out}) as a function of b and r . (d) Calculated *SERS* signal (logged plot).

In order to further elucidate the relationship between light coupling, absorption and *SERS* signals a simple resonant plasmon model can be considered (figure 7.7(a)). A full derivation of this model is presented in appendix A.2. This model assumes that light couples to plasmons propagating around the length of the

cavity L , where the field coupling strength of incoming light into the plasmon cavity is t , with r directly reflected such that $r^2 = 1 - t^2$. The cavity round-trip absorption is a , where $a = e^{-A}$ and A is the absorption strength, so that the field surviving a single pass of the cavity is b where $b^2 = 1 - a^2$. Plasmon interference implies that only certain plasmon energies fit within the cavity path length, leading to a round trip phase $\phi = LK_{eff} = L2\pi n_{eff}/\lambda$. Evaluating the multiply-reflected plasmon field, gives the total absorption spectrum:

$$\alpha = \frac{(1 - b^2)(1 - r^2)}{|1 - rbe^{i\phi}|^2} \quad (7.2)$$

Absorption (α) is plotted as a function of the cavity parameters b and r in figure 7.7(b) and confirms that absorption is maximum when coupling and reflection are perfectly matched ($b = r$). Extracting the absorption linewidth in radians (F is the half-width at half maximum) and the maximum absorption (α_m) from equation (7.2) and inverting the resulting equations gives expressions for the cavity parameters in terms of the measured absorption spectra:

$$b^2 = \exp\{-\gamma + \beta\} \quad (7.3)$$

$$r^2 = \exp\{-\gamma - \beta\} \quad (7.4)$$

where $\cos F = 2 - \cosh \gamma$ and $\cosh \beta = \alpha_{max} + \cosh \gamma(1 - \alpha_m)$. Hence by measuring α_m and F , values for b and r can be extracted, giving the enhanced field intensity $|E|^2(\lambda) = |\epsilon_{cavity}(\lambda)/\epsilon_{incident}|^2 = \alpha_m(\lambda)/(1 - b^2)$. It is commonly assumed that the *SERS* intensity for a molecule at r_i is proportional to $|E(r_i, \lambda_{in})|^2 |E(r_i, \lambda_{out})|^2$. However crucially important is the probability, \mathcal{F}_{out} , that the Raman-shifted plasmon emitted by the molecule will escape as a photon and not be re-absorbed in the metal, where:

$$\mathcal{F}_{out}^{-1} = 1 - \frac{1 - b^{-2}}{1 - r^2} \quad (7.5)$$

This is plotted as a function of cavity parameters in figure 7.7(c) and shows that intra-cavity absorption should be minimised in order to increase the probability of photon outcoupling \mathcal{F}_{out} . Calculating the total *SERS* signals leads to:

$$SERS \propto |E_{in}|^2 |E_{out}|^2 \mathcal{F}_{out} \quad (7.6)$$

This is plotted as a function of cavity parameters in figure 7.7(d) and shows that *SERS* favours high r and low absorption cavities where the high finesse leads to strong field enhancements within the cavity. Using the extracted values for α_m and F , gives the dashed curve in figure 7.8(a), which shows good qualitative agreement with the experimental *SERS* signals. The *SERS* contributions are broken down into field intensity $|E|^2$ and out-coupling \mathcal{F}_{out} components in figure 7.8(b). As the proportion of nickel in the rim is increased, absorption increases and both field intensity in the cavity and *SERS* outcoupling are reduced.

Despite this general agreement, the model predicts that the gold void with nickel rim should still give significant *SERS* signals of about 40% of the signal strength relative to a gold-only structure, whereas in experiments *SERS* is negligible for this structure. This discrepancy could partly be due to the reduced coverage of *SERS* probe molecules on nickel compared to gold. Whilst it is firmly established that thiols form well-defined compact monolayers on gold surfaces(94; 95), their attachment to nickel can be less efficient when deposited from dilute (1 mM) ethanolic solutions(96; 97). In this work benzenethiol was adsorbed from 10 mM ethanolic solutions and hence, some difference in relative coverage between gold and nickel cannot be ruled out. Since the field distribution of the rim plasmon modes is concentrated at the tip apex (shown in figure 7.8(c,d,e)), *SERS* signals are critically dependent on the precise location of molecules, magnifying the influence of molecular coverage differences. This implies that the majority of the *SERS* signal originates from molecules which occupy less than 5% of the available structure surface area from around the rim. Improved hybrid plasmon nanovoid performance for *SERS* is thus predicted by optimising the thickness of gold on the rim in concert with the supporting nickel void structure to actively concentrate field on molecules located at the gold tip apex.

In summary, these experiments confirm that the large *SERS* signals observed on gold nanovoid structures are provided by rim plasmon modes unique to the nanovoid geometry which are both strongly coupled to incident light by the underlying cavity void (and therefore highly radiative) and provide strong field

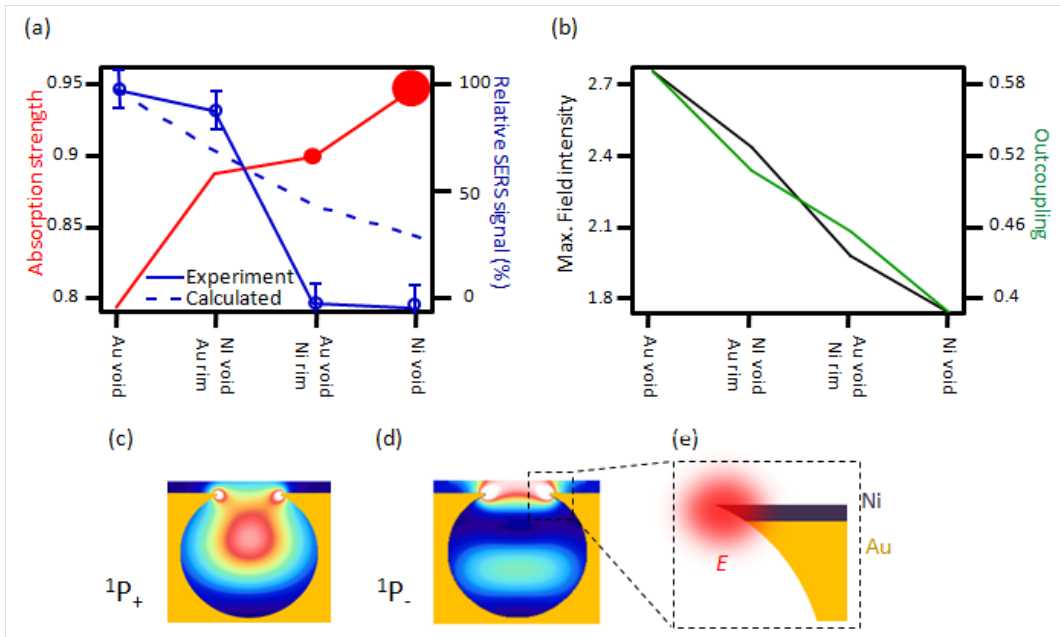


Figure 7.8: (a) Measured absorption strength (red) of plasmon modes with marker size corresponding to $FWHM$ spectral linewidth, compared to observed $SERS$ signal at 785 nm (blue solid line) plotted against rim metal composition ranging from fully gold to fully nickel. Calculated $SERS$ from resonant plasmon cavity model shown dashed. (b) Maximum field intensity and cavity out-coupling calculated using resonant plasmon cavity model. (c,d) Electric field distribution of the (c) $^1P_+$ and (d) $^1P_-$ localised plasmon modes which have a strong rim component. (e) Schematic of $^1P_+$ mode on a hybrid rim.

enhancements localised at the rim apex. By selectively coating the nanovoid structure with a thin layer of nickel the coupling strength, energy and linewidths of the plasmon modes are modified, selectively quenching $SERS$. Conversely, whilst a nickel void structure supports strong plasmons but does not give $SERS$, a hybrid structure composed of a nickel void and a gold rim is shown to give $SERS$ signals of similar magnitude to that of a gold only structure. Such experiments identify the precise geometrical location of plasmon modes responsible for $SERS$, and reveal the subtle relationship between absorption, field coupling and $SERS$ signals using a simple plasmon resonant cavity model. This informa-

tion is crucial for the effective use of plasmons in antenna applications such as reproducible surface enhanced Raman scattering and paves the way for hybrid structures combining novel plasmonic and catalytic properties simultaneously.

7.5 Conclusions

The nanovoid geometry supports a variety of unique plasmon modes which scale with cavity dimensions, making these structures ideal for studying *SERS* enhancement by specific modes. Angle-resolved reflectivity measurements allow the direct correlation between plasmon modes and *SERS* signals, revealing that enhancement is maximum when the incident laser light is resonant with a plasmon mode. However *SERS* is typically only observed for samples of normalised thickness \bar{t} greater than 0.5, where plasmons localised at the cavity rim provide strong field enhancements and efficient coupling to incoming and outgoing *SERS* photons. Experiments performed on hybrid nanovoids reveal that *SERS* signals are critically dependent on the precise composition of the structure rim, suggesting that the majority of the *SERS* signal originates from molecules which occupy less than 5% of the available structure surface area from around the rim. Comparison of experimental results with a simple resonant plasmon cavity model reveal that both the absorption strength and efficiency of coupling into and out of a plasmon mode are the crucial factors determining *SERS* enhancement on nanovoids. These results suggest that it may be possible to optimise substrates for *SERS* by selecting the thickness of gold on the rim in concert with the supporting nickel void structure to actively concentrate field on molecules located at the gold tip apex. Such hybrid nanovoid structures represent a radical new approach toward fabricating optimised *SERS* substrates.

Chapter 8

Flexible Plasmonics

8.1 Introduction

For many applications it is desirable to actively tune the optical or plasmonic properties of nanostructures, for example to create displays based on tunable diffraction gratings or low-cost electrochromic materials. Whilst there have been many examples of nanostructures with plasmonic properties tuneable by the structure geometry, *active* plasmon tuning has been limited in spectral range due to the optical(12), electronic(98), ferroelectric(99) and thermal (100; 101) tuning mechanisms involved. An alternative approach is to fabricate structures with *mechanically-tunable* plasmonic properties. Relatively few examples of mechanically tunable plasmonic structures have been demonstrated, with examples limited to tuneable gratings(102; 103) and plasmonic particle arrays embedded in a polymer matrix(104). However, by using a self-assembly and casting technique it is possible to fabricate a range of flexible nanostructures which have mechanically tunable optical or plasmonic properties. This chapter first presents mechanically tunable 1D and 2D diffractive substrates, before discussing the properties of thin-metal films supported on flexible elastomeric substrates. Flexible metal-elastomer nanovoids are then presented, before finishing with a section on stretchable nanotriangle arrays.

8.2 Stretchable 1D and 2D Diffraction Gratings

Stretchable diffraction gratings have been fabricated and proposed for a variety of applications(103; 105). For example, a display device comprising of a stretchable grating and a white light source would be able to produce the entire range of visible colours by utilising diffraction, producing colours not attainable with traditional emissive displays. Stretchable structures are commonly fabricated from elastic polymers, referred to as elastomers. Elastomers can be moulded around nanoscale structures such as gratings or tips, producing an almost perfect cast of the nanoscale features. Using a simple self-assembly and casting technique it is straightforward to fabricate 1D diffraction gratings. A schematic of the elastomeric grating fabrication process is shown in figure 8.1(a-d).

A thin layer of elastomer (Sylgard 182) was drop coated onto a gold-coated diffraction grating and left to cure. The elastomer was then peeled away from the grating template and a 100 nm gold coating evaporated onto the nanostructured elastomer to enhance the optical reflectivity (figure 8.1(e)). By imaging the first diffracted order of 633 nm light incident on the grating (figure 8.1(f)), the sample pitch was measured to be 890 nm. To measure the structure pitch as a function of strain, the grating was mounted on a computer controlled translation stage and the diffraction pattern was imaged as strain was applied (g) parallel and (h) perpendicular to the grating lines. A 30% applied strain produced a pitch *increase* of 25% when applied parallel to the grating, and a pitch *decrease* of 10% when applied perpendicular to the grating. The Poisson ratio of the elastomer is 0.5, giving a calculated pitch reduction of 15% for a 30% applied strain. Therefore for strains applied parallel and perpendicular to the grating lines the observed pitch change is short of that expected, indicating that the strain is not completely transferred to the nanostructure geometry. Instead, a proportion of the strain is taken up in the formation of cracks in the metal film, shown in the *SEM* images of figure 8.1(i,j). As the sample was increasingly stretched the density of cracks increased, and the reflected light intensity dropped as the film became semi-transparent. Upon removal of the applied strain the grating relaxed back to its original pitch and the reflected light signals recovered.

8.2 Stretchable 1D and 2D Diffraction Gratings

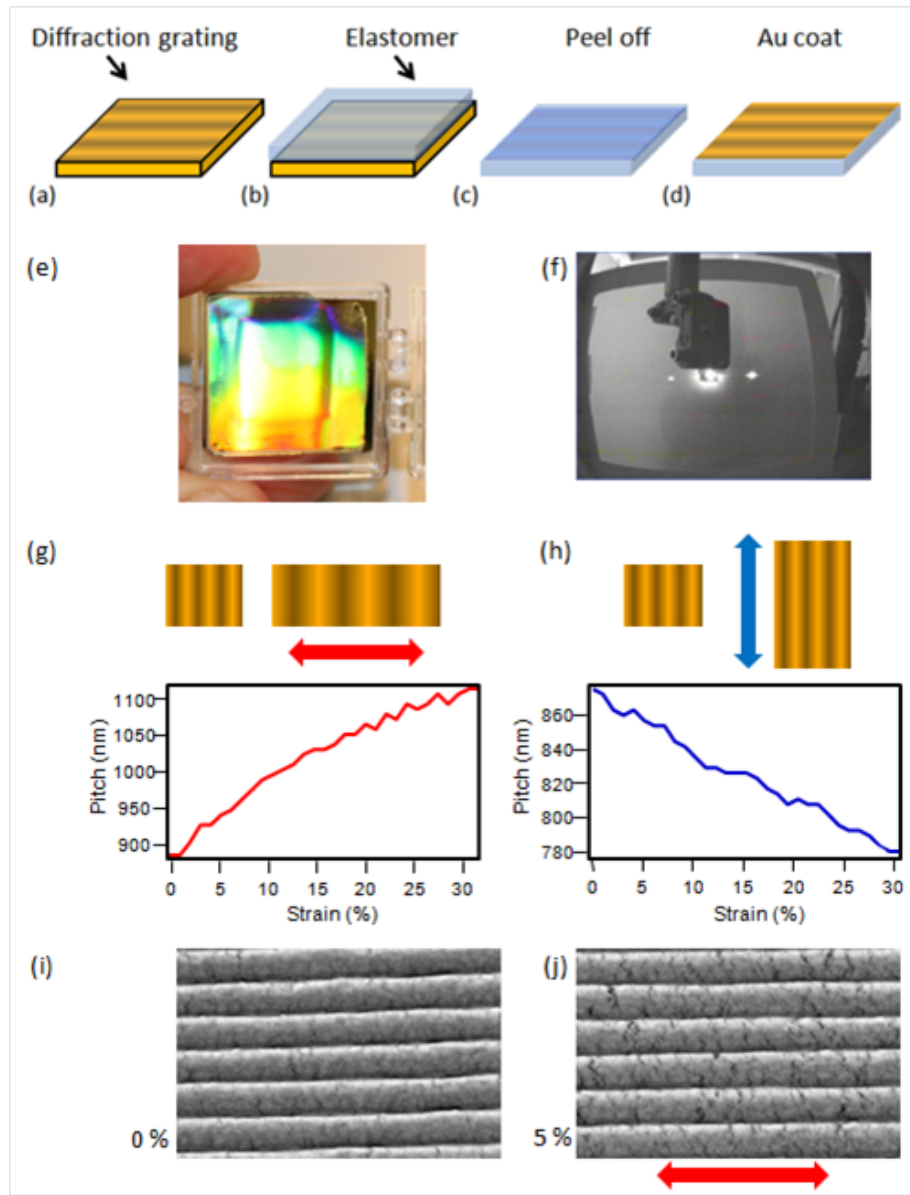


Figure 8.1: (a-d) Schematic of the elastomeric grating fabrication. (e) Photograph of the stretchable elastomeric grating. (f) The two zero-order diffracted spots. The optically measured pitch change with strain applied (g) parallel to and (h) perpendicular to the grating lines. SEM images at (i) 0% applied stretch and (j) at 5% showing the formation of cracks in the gold film. Red arrow indicates stretch direction.

8.2 Stretchable 1D and 2D Diffraction Gratings

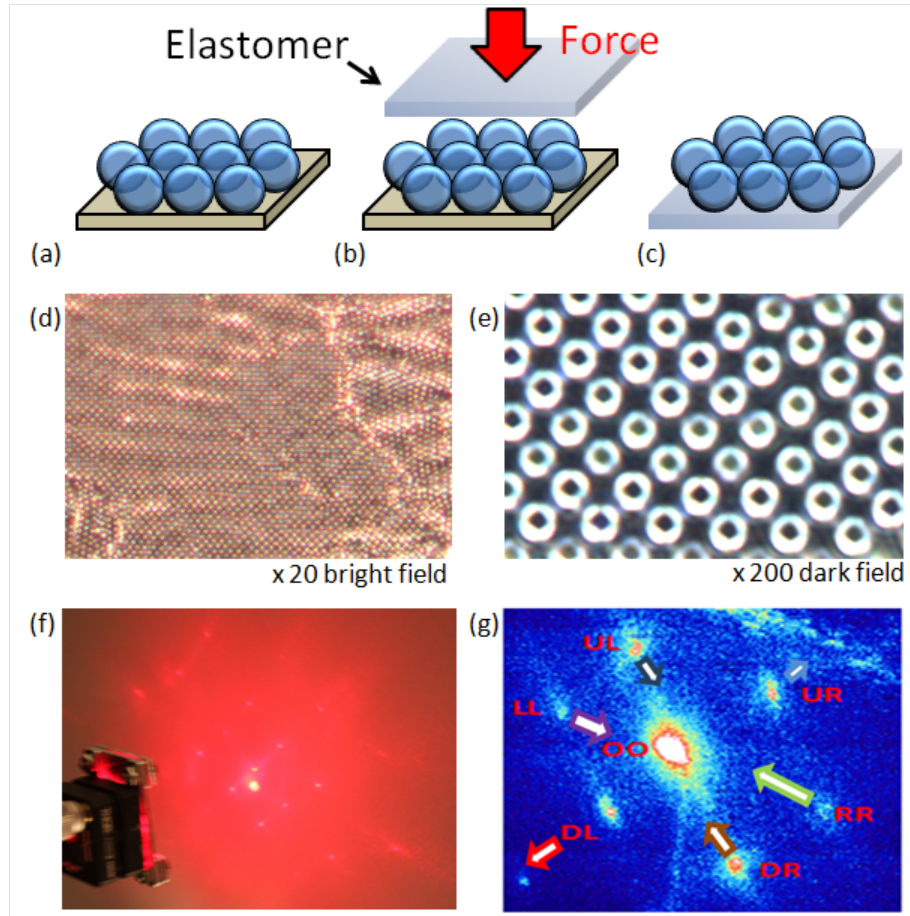


Figure 8.2: (a,b,c) Self-assembled spheres are transferred onto a pre-cured elastomer film. Microscope images of spheres (overcoated with 25 nm of aluminium after experiments to aid imaging) at (d) $\times 20$ bright field and (e) $\times 200$ dark field. (f) Imaged diffraction pattern. (g) Image of the same diffracted pattern with a strain of 30% applied in the plane of the LL-RR peaks. Arrows indicate the direction and magnitude of relative movement of each diffracted peak.

8.3 Metal Films on Elastomers

Having demonstrated a tunable 1D grating, a 2D grating was produced by transferring self-assembled spheres from a glass slide onto an elastomer film (figure 8.2(a,b,c)). A layer of glue ensured the adhesion of the spheres to the elastomer on transfer. This simple technique produces well ordered domains of spheres on the elastomer, as shown in the images of figure 8.2(d,e) and by the well defined diffraction pattern in figure 8.2(e). The sample pitch (corresponding to the arrangement of spheres on the sample surface) was measured as a function of applied strain by imaging the diffraction pattern for 633 nm light incident on the structure. Since the diffraction pattern is essentially a Fourier transform of the 2D surface structure, changes in the diffraction pattern indicate how spheres re-arrange on the elastomer film. The relative motion of the diffraction peaks is shown in figure 8.1(f). The largest increase in pitch is observed for spheres arranged parallel to the stretch direction. However it is clear that the pitch changes are not equal in all directions, indicating that the spheres do not maintain a hexagonal arrangement on the film but re-arrange to reflect the strain in the underlying elastomer film.

These samples demonstrate that by using simple fabrication procedures is it possible to produce elastomeric nanostructures which have stretchable optical properties. However elastomer nanostructures coated with metal do not completely transfer applied strain into changes in the nanostructure geometry. Instead a proportion of the applied strain is absorbed by cracks which form in the metal film. Therefore before moving on to discuss metal-elastomer nanostructures with stretchable plasmonic properties, it is necessary to characterise the behaviour of metal-elastomer films under strain.

8.3 Metal Films on Elastomers

Metals in their bulk form are generally mechanically brittle. However, metal films with thicknesses on the order of tens to hundreds of nanometers can be relatively ductile. Thin-metal films supported on elastomers accommodate strain by two main mechanisms. Firstly, films tear at strains of $\approx 2\%$ (106; 107). In this process, the metal film thins out at localised defect sites, called necking sites. Rupture then proceeds from these sites, where the strain required for rupture is proportional

8.3 Metal Films on Elastomers

to the stiffness of the metal, as quantified by the metals Youngs modulus. The second mechanism by which strain is accomodated is by the wave-like folding of the metal film(108). Wave crests form parallel to the direction of applied strain and are due to the mechanical buckling instability of the film under compressive force, shown schematically in figure 8.3(a).

The strain properties of metal-elastomer films were investigated by stretching samples on a computer controlled translation stage whilst imaging the film with a microscope or *SEM*. Samples were mounted on the translation stage by clamping the two ends of the sample. This compresses the edges of the sample and causes the whole sample to bow upwards in the middle, introducing a small number of cracks even for strains of 0%. Figure 8.3(b) shows a $\times 40$ image of a 100 nm thick flat metal-elastomer film which is being stretched by 10%. Both cracks and waves are clearly visible. The wavelength of the waves is measured to be $\approx 15\mu\text{m}$ for this film with a peak to trough height of $\approx 4\mu\text{m}$. Both the wavelength and amplitude of waves are a function of the film thickness and the strain mis-match between the metal and the underlying elastomer. Waves are typically seeded at the edge of cracks, but form over a much longer time scales. Waves can be almost uniformly distributed across a mm^2 area if stretching is performed very slowly (mm per hour).

A metal-elastomer sample consisting of both flat-metal and nanovoids is shown in figure 8.3(c,d,e,f). The left side of each image is nano-structured with 900 nm diameter voids of thickness $\bar{t} = 0.3$, and the right hand side is flat-metal. Initially the sample was clamped onto the translation stage but not stretched (8.3(c)). Typically any manual handling of a sample will introduce a small number of cracks into the film, and here a single crack can be seen running across the top of the image. Figure 8.3(d) shows the same sample position when stretched by 10%. There are two new cracks in the image and the original crack has increased in width. The density of cracks appears identical across the flat and nanostructured portions of the surface, indicating that the nanostructures do not noticeably alter the mechanical properties of the film. Waves are also seen in the image, and the amplitude and wavelength of the waves is also identical across the flat and nanostructured areas of the surface. When stretched by 20%, the sample surface becomes densely covered with cracks and waves (figure 8.3(e)). Finally, figure

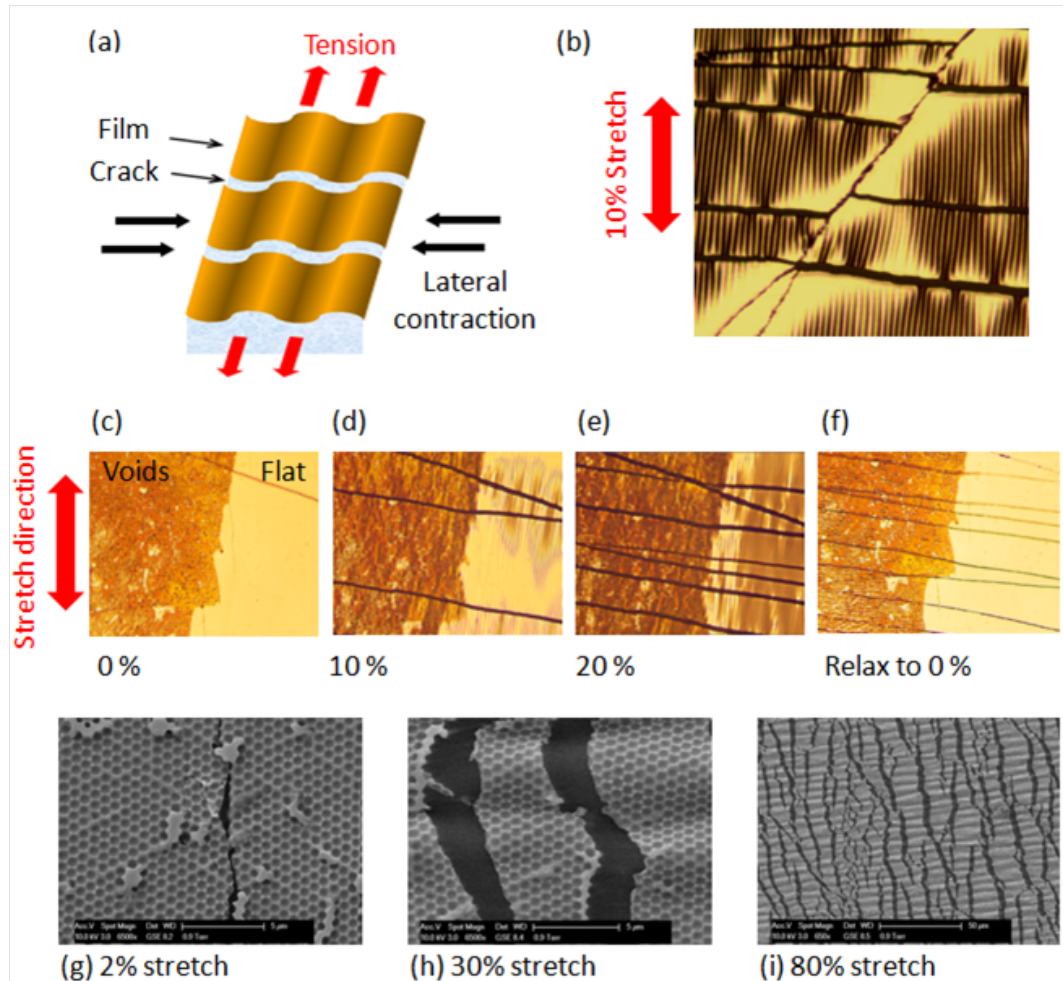


Figure 8.3: (a) Schematic of crack and wave formation on an elastomer-supported metal film under strain. (b) $\times 40$ image of a 100 nm gold film supported on an elastomer stretched by 10%. $\times 10$ image of an elastomeric nanovoid sample, left side of each image is nano-structured with 900 nm diameter voids of thickness $\bar{t} = 0.5$, right hand side is flat metal at (c) no stretching, (d) 10% stretch, (e) 20% stretch and (f) relaxed back to 0% stretch. SEM images of an elastomer being stretched at (g) 2% stretch the metal film supporting voids ruptures. (h) Close-up showing the metal-film bending over waves and tearing at 30% stretch. (i) At 80% stretch showing the high density of cracks and waves on the film surface.

8.4 Flexible Metal-Elastomer Nanostructures

[8.3\(f\)](#) shows the sample was relaxed back to 0% stretch. As the strain was removed, the waves gradually reduced in amplitude, and the cracks closed up but remain visible.

To get more information about the metal-elastomer film stretching process, the film was stretched as it was imaged with an *SEM* (figure [8.3](#)). (g) At 2% stretch the film ruptures, with tearing proceeding from defects in the film. (h) Although the film tears, the metal remains adhered to the underlying elastomer substrate, despite the build up of large-amplitude waves. A lower magnification image in figure [8.3\(i\)](#) shows the high density of cracks and waves when the film is stretched to 80%. These results demonstrate that metal-elastomer films can bend to accomodate applied strain, but will rupture when stretched beyond $\approx 2\%$. Therefore flexible plasmonic nanostructures based on metal-elastomer films should be designed to accomodate strain by bending, and not stretching.

8.4 Flexible Metal-Elastomer Nanostructures

As shown in the preceeding chapters, by fabricating appropriate nanostructures plasmons can become localised on particles or within cavities, producing concentrated optical fields which are utilised for applications such as *SERS*. The energy and field distribution of plasmons are strongly dependent on nanostructure geometry, and can be tuned by slight changes in nanostructure shape or volume. Therefore by fabricating *flexible* metal-elastomer nanostructures, it is in principle possible to create structures with actively-tunable plasmonic properties, for example to create low-cost electrochromic materials or wideband plasmonic filters.

Using self-assembly and casting techniques, a range of flexible metal-elastomer substrates can be fabricated which have mechanically tunable plasmonic properties. These nanostructures include (a) hemispheres, (b) voids, (c) tips and (d) triangular pits (figure [8.4](#)). These structures consist of solid-metal films or particles supported on or embedded within a flexible 3D substrate. Both particles and cavities support plasmon modes with optical field distributions which reflect the symmetry of the nanostructure geometry. Therefore the plasmonic resonances of

8.4 Flexible Metal-Elastomer Nanostructures

flexible metal-elastomer substrates are expected to shift when the bulk sample is mechanically stretched (figure 8.4(e)).

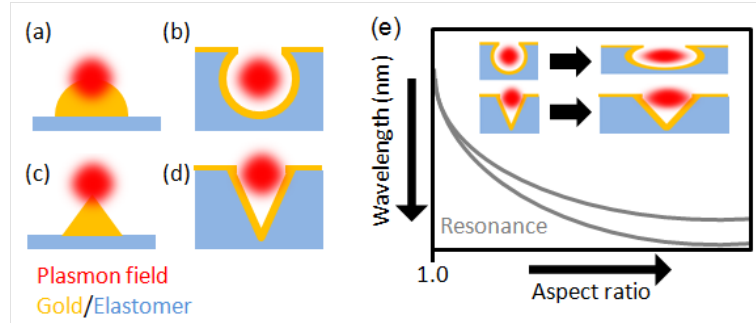


Figure 8.4: Metal-elastomer nanostructures and resonant plasmon fields for (a) hemispheres, (b) voids, (c) tips and (d) triangular pits. (e) Plasmon-resonant wavelength dependence (grey line) on a structures aspect ratio. As structures are stretched, the symmetry of the system is broken, resulting in new plasmon modes.

In the case of particles supported on an elastomer film, stretching the substrate will shift the relative position of particles within an array, thereby tuning the resonances associated with the whole array. However for cavity based nanostructures (such as triangular pits or truncated spherical nanovoids), it is the metal cavity itself which will change shape. Therefore the key design constraint when fabricating flexible metal-elastomer cavities is preserving the metal surface area (to avoid cracking or tearing) while changing the cavity volume or aspect ratio. In this respect, the cavities of nanovoid structures are ideally suited to mechanical manipulation since the spherical geometry uniformly distributes the applied strain, minimising the possibility of damaging the cavity walls. Although triangular pits have been demonstrated, the remainder of this chapter focuses on the properties of flexible metal-elastomer nanovoids.

8.4.1 Flexible Nanovoids

Metal-elastomer nanovoids are fabricated using a self-assembly and casting procedure shown in figure 8.5(a-f). This procedure produces structures ranging from shallow dishes up to fully encapsulated spherical cavities. A monolayer of polystyrene spheres is self-assembled on a gold-coated glass slide and a thin layer of elastomer (Sylgard 182) is drop cast onto the spheres and left to cure. Upon curing, the elastomer film is peeled off of the substrate with the spheres embedded in the film. The spheres are then removed by dissolving in DMF solution, and finally a 100 nm thick layer of gold is sputtered onto the elastomer substrate. To fabricate a nanovoid of a particular \bar{t} , metal is electro-deposited up to a height $\bar{h} = 1 - \bar{t}$ around the self assembled spheres at step (b). If the height of metal deposited is greater than $\bar{h} \approx 0.3$ then spheres remain adhered to the metal template rather than lifting off with the elastomer film. This currently prevents the fabrication of elastomeric cavities in the range of $\bar{t} \approx 0.5 - 0.7$. Nevertheless, using this fabrication procedure it is possible to produce elastomer cavity samples of stucture thicknesses in the range of $\bar{t} = 0 - 0.5$ and $\bar{t} = 0.7 - 1$, yielding structures which support plasmon modes that are tunable by \bar{t} and by stretching.

Metal-elastomer nanovoid samples of cavity diameter 900 nm (figure 8.5(g)) appear opalescent due to diffraction by the periodic structure and absorption by plasmon modes. *SEM* imaging of the structure (figure 8.5(h)) reveals the smooth metal coating achieved by evaporation onto an array of nanovoids of thickness $\bar{t} = 0.8$, and confirms a conformal metal coating within cavities.

As described in chapter 5, nanovoids support both propagating Bragg plasmons and localised void plasmon modes, both of which are sensitive to strain. Therefore to produce electrochromic effects in metal-elastomer nanovoids, both the Bragg or void plasmon resonances can be tuned. However, due to their narrow absorption linewidths, it is expected that localised plasmon resonances should produce the strongest observable colour-change effects. *BEM* calculations show that as the ellipticity of a nanovoid cavity increases, the void plasmons tune to longer resonant wavelengths, where for the 1P mode a 20% strain produces $\approx 10\%$ increase in resonant wavelength (figure 8.6(b)). Similar tuning is found for

8.4 Flexible Metal-Elastomer Nanostructures

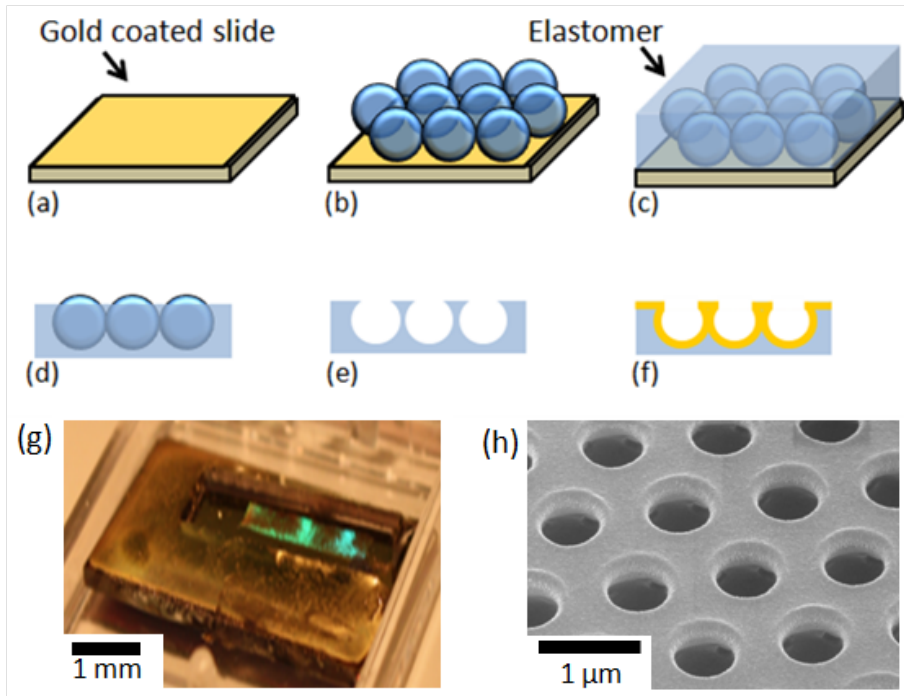


Figure 8.5: (a-f) Schematic of the metal-elastomer nanovoid fabrication procedure. (g) Image of a typical sample, the opalescent strip is nanostructured with nanovoid cavities. (h) *SEM* image of a $\bar{t} = 0.8$ structure.

the higher order 0P and 1D plasmon modes, where the rate of tuning is dependent on the precise field distribution of the mode within the cavity. In contrast, Bragg plasmon coupling is by the periodicity of the surface structure, and tunes linearly with increasing strain.

The experimentally measured angular dispersion of plasmons on metal-elastomer nanovoids is shown in figure 8.7(a). The dispersive absorption peaks of a 900 nm diameter elastomer-metal nanovoid of thickness $\bar{t} = 0.3$ indicate that it is a propagating Bragg plasmon mode. The coupling-strength and energetics of this Bragg plasmon mode match those of Bragg plasmons on solid-metal substrates. The influence of stretching the structure on this Bragg plasmon was investigated by mounting the sample on a translation stage whilst recording the normal incidence reflectivity using a $\times 10$ optical microscope collecting over a range of angles $\theta \leq 5^\circ$. The strain-dependent reflectivity shows an absorption dip which tunes from

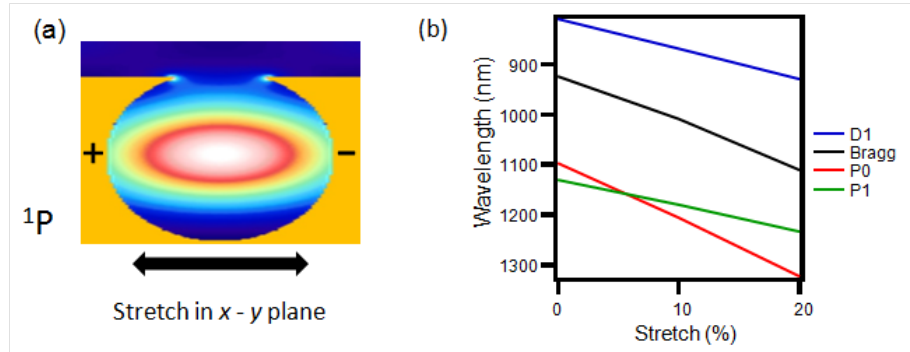


Figure 8.6: (a) Field distribution of the 1P cavity mode in a 900 nm diameter nanovoid which has been stretched by 20% in the x - y plane. +/- indicate position of charge nodes on the cavity walls. (b) Calculated energy of plasmon modes upon cavity stretching.

730 nm at 0% applied strain to 745 nm at 5% applied strain (figure 8.7(b)). This 3 nm/% is less than half that predicted from calculations, indicating that the strain is not completely transferred across the metal film. Comparison of microscope images of the structure at 0% and 5% applied strain (figure 8.7(c,d)) shows the formation of cracks and waves (as described in section 8.3) which absorb a fraction of the applied strain. The sample reflectivity drops as the rippled surface scatters and diffracts light and the density of cracks increases. As the strain is increased beyond 5% the reflected light intensity drops rapidly as the number of defects increases and the plasmon resonances can no longer be accurately identified. In order to overcome these defects and produce samples with more widely tunable plasmon resonances, the flat-metal film must be removed from around the coated nanovoids. This can be achieved using a sacrificial aluminium layer, which is deposited before the removal of the spheres during sample fabrication. This process should leave gold only *within* cavities and ensure that the maximum possible strain is applied to the cavities and not to the surrounding flat surfaces, thereby minimising the formation of cracks and waves.

In these samples localised plasmon resonances are not yet observed on thicker nanovoid structures of $\bar{t} \geq 0.7$. One explanation is that although sputtering successfully coats the cavity conformally, it is unable to coat a sufficiently thick

8.4 Flexible Metal-Elastomer Nanostructures

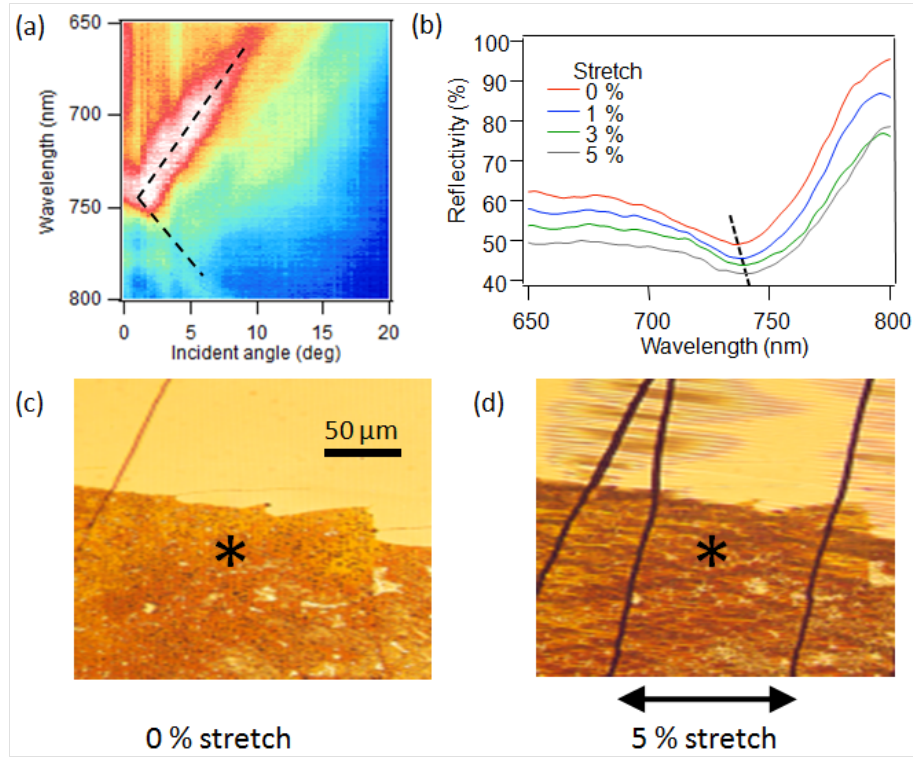


Figure 8.7: (a) Angle-resolved normalised reflectivity for a 900 nm diameter metal-elastomer nanovoid of thickness $\bar{t} = 0.3$. (b) Reflectivity of the structure with applied strain (dashed line indicates the wavelength of peak plasmon absorption). (c,d) $\times 10$ images of (left) nanovoids and (right) flat metal on elastomer at strains corresponding to 0% and 5% stretching. Spectra in (b) taken at * position.

metal layer around the entire cavity due to shadowing by the cavity lip entrance. Therefore the cavity may not provide sufficient confinement for strong localised plasmon resonances. However it may be possible to improve the metal coating within cavities by using additional electrodeposition of metal after the main fabrication procedure, or by seeding the cavity walls with metal nanoparticles [ongoing].

In summary, using a self-assembly and casting procedure it is possible to fabricate flexible metal-elastomer nanovoids of almost any cavity diameter and thickness \bar{t} . Upon coating with metal, these structures support Bragg plasmon

8.4 Flexible Metal-Elastomer Nanostructures

resonances which are tunable by applying strain to the structure. Localised plasmon resonances have not yet been demonstrated on these structures, due to the weak confinement provided by the metal walls of thicker cavities. The fabrication procedure can also be modified to produce alternative geometries, including gratings, pits, spikes and particles. One alternative geometry which is currently being investigated for tunable plasmonics is the stretchable nanotriangle array, described in the following section.

8.5 Tuneable Nanotriangle Substrates

A plasmonic geometry which possessss well characterised localised plasmon resonances is the nanotriangle array (109). Nanotriangles can be fabricated in large area arrays, with good control over the metal thickness and periodicity. Nanotriangles are typically fabricated on solid substrates, however it is straight-forward to fabricate nanotrianlge arrays on stretchable elastomer substrates. By placing nanotriangles on a stretchable substrate, it is possible to actively tune the pitch of the array, thereby tuning the plasmon resonances of the triangle array. Furthermore, since nanotriangles are discrete particles of metal on an elastomer substrate, the cracks and waves associated with stretched metal-films will not be present. Figure 8.8(a-e) shows a schematic of the nanotriangle fabrication procedure.

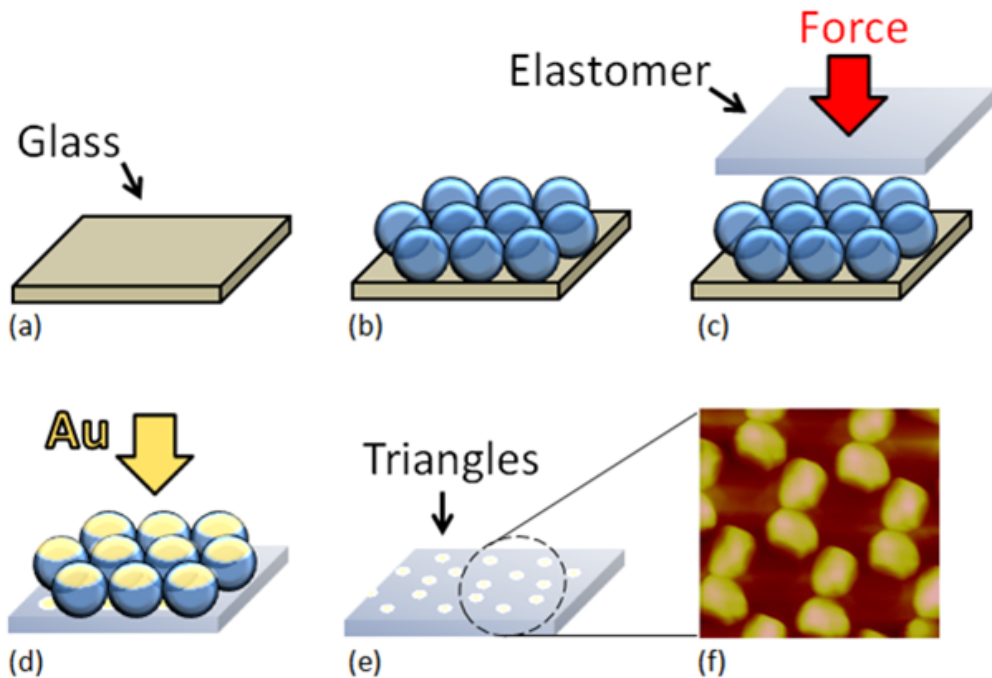


Figure 8.8: (a-e) Schematic of the nanotriangle fabrication procedure. (f) *AFM* image of a nanotriangle array.

A pre-cast elastomer film is forced into contact with a self-assembled 2D sphere

8.5 Tuneable Nanotriangle Substrates

array, transferring spheres from a glass slide onto the elastomer. Metal is then evaporated down onto the structure, where the triangle pitch and metal height are selected by the choice of sphere size and duration of evaporation time. The spheres act as a mask, allowing the deposition of metal between spheres. The spheres are then removed by sonication in DMF for 1 hour, revealing the nanotriangle array underneath. Microscope images confirm large area arrays of nanotriangles, with uniform coverage over areas of up to 3 mm^2 , shown in figure 8.9(a). *AFM* images of the nanotriangles reveal that sputtering achieves smooth metal deposition and indicates that nanotriangles are spatially insulated from each other.

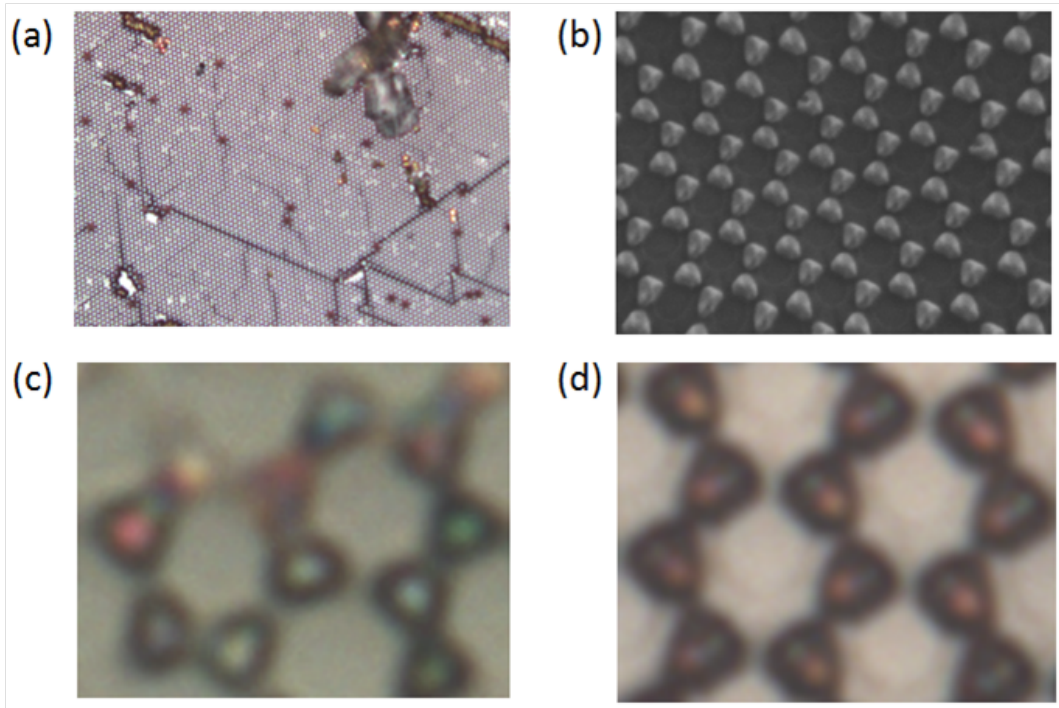


Figure 8.9: (a) $\times 10$ image showing large area coverage of nanotriangles. (b) *SEM* image of nanotriangles showing large area of uniformly arranged nanotriangle arrays. $\times 200$ bright-field microscope images of nanotriangles fabricated from (c) $2 \mu\text{m}$ and (d) $3 \mu\text{m}$ spheres.

Figure 8.9 shows $\times 200$ microscope images of nanotriangles fabricated from (c) $2 \mu\text{m}$ and (d) $3 \mu\text{m}$ spheres. Images of nanotriangles fabricated from $2 \mu\text{m}$

8.5 Tuneable Nanotriangle Substrates

spheres show that each triangle scatters strongly at a single wavelength, where the scattered wavelength is a function of the triangle morphology and location with respect to nearby triangles. Nanotriangles fabricated from $3\mu\text{m}$ spheres show a variation in colour across the triangle. It is possible that, due to the larger size of these triangles, the colours observed are due to higher order localised plasmon resonances. Preliminary position-resolved spectroscopy performed on these samples reveal large variations in the dark field scattered spectra from different nanotriangles within an array, shown in figure 8.10. Future measurements will use a scanning stage with nanometer spatial resolution to track the spectra of individual nanotriangles as the sample is stretched, and the plasmon resonances of both individual particles and the array are tuned.

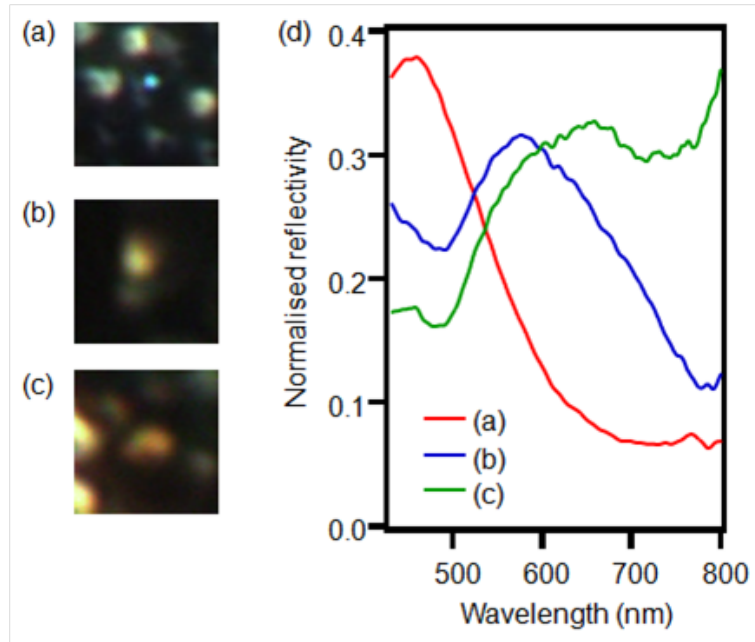


Figure 8.10: (a-c) $\times 200$ dark-field images of nanotriangles fabricated from $2\mu\text{m}$ spheres, and (d) corresponding dark-field spectra.

In summary, arrays of nanotriangles supported on an elastomer substrate support localised plasmon resonances which depend on the triangles morphology and position within an array. Upon stretching, the arrangement of particles is modified, tuning their plasmon resonances. [Experiments are ongoing.]

8.6 Conclusion

Using simple fabrication procedures is it possible to produce a range of flexible nanostructured substrates with tunable optical and plasmonic properties. Stretchable diffraction gratings were fabricated with periodicity in both 1D and 2D. The diffraction pattern was imaged as the gratings were stretched, allowing the change in periodicity of the nanostructure to be measured. Flexible metal-elastomer nanovoid structures were shown to support plasmon resonances equivalent to those found on traditional solid-metal nanovoid substrates, and dispersion measurements indicate that these resonances tune when the sample is stretched. However, a significant proportion of the applied strain is taken up by the formation of cracks and waves in the metal film which currently limit the range of spectral tuning possible. Finally, stretchable nanotriangle arrays were shown to support localised plasmon resonances which depend on the size and periodicity of the triangles, and the position of the triangle within an array. Potential applications for stretchable plasmonic substrates include new colour changing materials and tuneable *SERS* substrates.

Chapter 9

Conclusions

This thesis has presented a study into the plasmonic properties of nanovoid surfaces under a range of conditions. It has been shown that the technique of template self-assembly and electrochemical deposition can be used to produce well-ordered nanovoids with a range of sizes and from a range of metals. These structures have been thoroughly characterised to understand the physical properties of the sub-micron geometries. Gold structures have been the primary focus of this thesis due to their chemical inactivity and robustness. The surface geometry follows that of the initial template except when the sample thickness becomes close to the diameter of the voids. Here, instead of encapsulating the cavities the structures form funnels leading from the top surface into the spherical cavities.

Both localised and delocalised surface plasmon modes have been found to exist on the samples and these different modes have been analysed in detail using a custom-built computer controlled goniometer. Delocalised Bragg modes exist when the samples form arrays of shallow dishes and their energetics have been found to fit well with a weak-scattering model. Bragg plasmons have been shown to scale linearly with pitch and refractive index as predicted. The localised plasmon modes of truncated spherical cavities have, for the first time, been comprehensively modelled using boundary element calculations, with results showing excellent agreement with experiment.

Calculations of the cavity absorption and electric near-field distribution identify plasmon wavefunctions in voids according to their atomic-like symmetries, and modes are correspondingly labelled by quantum numbers ${}^mL^{1,2\cdots}P,D,F$ in

accordance with Mie theory. For a fully encapsulated cavity, mode solutions are identical to those calculated using Mie theory. As the spherical voids are progressively truncated, degenerate radial modes split in energy, with intense coupling to incident light at specific optimal angles. In general, as the nanovoid is increasingly truncated, the modes are less encapsulated and most of them move away from the metal and increase in energy. Approaching from the opposite limit, the modes of shallow cavities resemble the Bragg plasmon dispersion, and in general, modes evolve out of the surface plasmon bands toward the Mie solutions as the cavity thickness increases.

The calculations performed provide a clear and intuitive understanding of the properties of plasmon modes in truncated spherical cavities. The electric field distribution and vector orientation of each wavefunction solution determine the energy and coupling efficiency of each mode. Significantly, the calculations performed revealed that nanovoids possess additional rim plasmon modes not present on particles or fully encapsulated voids; these modes selectively couple with void plasmons to produce bonding and antibonding hybridised states which provide the significantly enhanced optical fields responsible for the large *SERS* signals generated by these structures. The rim modes possess a dipole like symmetry, and will strongly couple to void modes with $m = 1$ symmetry; the most significant of which is the ${}^1P_+$ mode, a mode which is responsible for many of the phenomena investigated in this thesis due to the fact that this mode conveniently sits in the middle of the visible spectral range for a 600 nm diameter nanovoid cavity. The ${}^1P_+$ mode is strongly coupled due to its interaction with the radiative rim mode, giving this mode a broad spectral width. This mode is strongly modified by coating the rim with another metal; a property which has allowed the experimental verification of many of the plasmon properties predicted by calculations.

With an understanding of the optical and plasmonic properties established, a series of techniques were investigated for modifying the plasmonic properties of nanovoids. Firstly, microsphere structures consisting of an array of spheres partially embedded in a plasmonic metal film were shown to support new propagating surface modes with modified dispersion characteristics. Diffractively coupled optical and plasmonic surface modes couple light into the localised modes of the

sub-micron spheres, producing structures with well defined resonances whose energies scale with sphere diameter and agree closely with Mie calculations. This provides a novel technique for coupling light into the modes of microspheres, a process which has typically proven very difficult and had previously only been demonstrated using nano-positioned alignment procedures. Further experiments revealed that upon coating the spheres with a thin layer of metal, the interaction between the modes of neighbouring spheres is modified, revealing strong coupling between adjacent spheres which leads to the formation of minibands. This result suggests that clusters of microspheres effectively form a plasmonic molecule. Adding spheres to the cluster change the overall properties, allowing customised resonances for future plasmonic applications.

The next technique explored was the guiding of plasmons by fabricating nanovoids in linear arrays. Spheres were self-assembled in V-groove trenches, and electrodeposition performed to fabricate linear arrays of nanovoids graded in thickness. Angle-resolved reflectivity measurements revealed that these structures support a variety of plasmons, which are only coupled for light incident parallel to the trench array. This result indicates that the observed plasmons propagate along the length of the void array, forming a plasmon waveguide. Comparison with reflectivity data from regular 2D void arrays suggest that trench structures support modified plasmons, and provides a route to understanding the coupling between neighbouring void plasmons, not currently accounted for in calculations.

The last technique for modifying the plasmonics of nanovoids investigated was the use of coatings to modify specific plasmon modes located on the structure rim. Upon coating a gold nanovoid rim with a layer of nickel the absorption strength and linewidth of plasmon modes *only* located on the rim were modified, allowing the distinction between absorption occurring at the rim and from inside the void. It was found that coating with lossy nickel increased the absorption strength and linewidth of the observed plasmon resonances. These experiments verified for the first time the precise geometrical location of plasmon modes within the nanoscale architecture and provide a technique for investigating and modifying the properties of specific plasmon modes.

One of the main applications of plasmonic nanostructures is as substrates for *SERS*. However in practice the commercial exploitation of *SERS* has been

hindered by the lack of reproducible substrates optimised at *SERS* wavelengths. Therefore understanding the relationship between plasmon modes and *SERS* signals is crucial for the optimisation of substrates. To this end, a series of experiments were performed to investigate the *SERS* properties of nanovoids. By comparing calculations with angle-resolved reflectivity measurements, the role of specific plasmon modes in *SERS* from nanovoids has for the first time been identified. Maximum *SERS* is observed when an incident laser is in resonance with a plasmon mode of the structure. However not all plasmon modes enhance *SERS* with equal efficiency. To investigate further, experiments were performed on coated nanovoid structures. Upon coating a gold void with a nickel rim, *SERS* signals were completely quenched, with the removal of the nickel, *SERS* signals completely recovered. This confirmed that rim plasmons were primarily responsible for the large *SERS* signals observed from nanovoids. A series of intermediate coated structures were fabricated, allowing the investigation of the relationship between rim metal composition, plasmonic absorption and coupling, and *SERS* signals. Comparison of experimental results with a resonant cavity model highlight that *SERS* signals are a convolution of the plasmon field strength with the efficiency of coupling into and out of that mode. Such experiments pave the way for *SERS* optimised nanostructures and provide a unique insight into the fundamental physical processes taking place during *SERS* measurements.

Finally, the use of metal-elastomer thin films to fabricate flexible plasmonic substrates was investigated. Using simple fabrication procedures it was possible to produce a range of flexible nanostructures, such as stretchable nanovoids, gratings and triangle arrays. Dispersion measurements reveal that these structures support plasmon modes which tune when the samples are stretched. Future devices based on stretchable plasmonic surfaces could include tuneable *SERS* substrates and new colour changing materials.

Appendix A

Derivations

A.1 Finding Electric Charge Density

From equations (2.1) - (2.4) the divergence of equation (2.4) leads to:

$$\nabla \cdot (\nabla \times \mathbf{H}) - \epsilon \nabla \cdot \frac{\partial \mathbf{E}}{\partial t} = \sigma \nabla \cdot \mathbf{E} \quad (\text{A.1})$$

Since $\nabla \cdot (\nabla \times \mathbf{H}) = 0$, equation (A.1) can be substituted into equation (2.2) to give:

$$-\frac{\epsilon}{\sigma} \nabla \cdot \frac{\partial \mathbf{E}}{\partial t} = \frac{\rho}{\epsilon} \quad (\text{A.2})$$

This equation can be compared to the temporal differentiation of equation (2.2):

$$\nabla \cdot \frac{\partial \mathbf{E}}{\partial t} = \frac{1}{\epsilon} \frac{\partial \rho}{\partial t} \quad (\text{A.3})$$

Now $\frac{\partial \mathbf{E}}{\partial t}$ can be eliminated between eqautions (A.2) and (A.3) leading to:

$$-\frac{\sigma \rho}{\epsilon} = \frac{\partial \rho}{\partial t} \quad (\text{A.4})$$

This equation can only be valid if ρ takes the form given in equation (2.5).

A.2 Resonant Plasmon Model

In order to further elucidate the relationship between light coupling, absorption and *SERS* a simple resonant plasmon model is discussed. This model assumes that light couples to plasmon's propagating around the length of the cavity L , where the field coupling strength of incoming light into the plasmon cavity is t , with r directly reflected such that $r^2 = 1 - t^2$, shown in figure A.1(a). The cavity absorption is a , where $a = e^{-A}$ and A is the absorption strength, so that the field surviving a single pass of the cavity is b where $b^2 = 1 - a^2$.

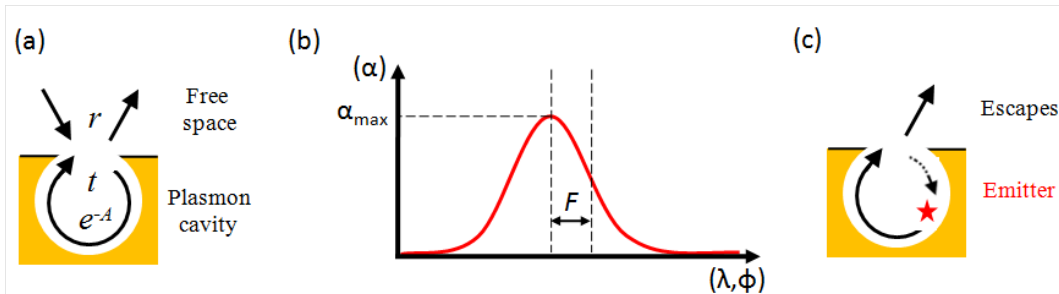


Figure A.1: (a) Schematic plasmon cavity. (b) Extracted absorption α_m and *HWHM* (F) of an absorption peak. (c) Schematic of an emitter in a cavity, only a fraction of the internally generated field can escape.

Plasmon interference implies that only certain plasmon energies fit within the cavity path length, leading to a round trip phase $\phi = LK_{eff} = L2\pi n_{eff}/\lambda$. The expression for the multiply reflected plasmon field E is:

$$E = at(1 + bre^{i\phi} + [bre^{i\phi}] + \dots) = \frac{at}{1 - rbe^{i\phi}} \quad (\text{A.5})$$

The light absorbed from the field in the cavity is $|E|^2$ where:

$$|E|^2 = \alpha = \frac{a^2 t^2}{|1 - rbe^{i\phi}|^2} = \frac{(1 - b^2)(1 - r^2)}{|1 - rbe^{i\phi}|^2} \quad (\text{A.6})$$

Solving for maximum absorption on resonance α_m :

$$\alpha_m = \frac{(1 - b^2)(1 - r^2)}{(1 - rb)^2} \quad (\text{A.7})$$

A.2 Resonant Plasmon Model

Now calculating the absorption at *HWHM* (F), as shown in figure A.1:

$$\frac{\alpha_m}{2} = \frac{(1 - b^2)(1 - r^2)}{|1 - rbe^{iF}|^2} \quad (\text{A.8})$$

Substituting α_m from equation (A.7) and re-arranging in terms of F :

$$\cos F = 2 - \frac{rb + \frac{1}{rb}}{2} \quad (\text{A.9})$$

Now let $rb = e^\gamma$:

$$\cos F = 2 - \frac{e^\gamma + e^{-\gamma}}{2} = 2 - \cosh \gamma \quad (\text{A.10})$$

Similarly setting $\frac{r}{b} = e^\beta$, substituting into equation (A.7) and re-arranging gives:

$$\cosh \beta = \alpha_m + \cosh \gamma(1 - \alpha_m) \quad (\text{A.11})$$

Now since $rb = e^\gamma$ and $\frac{r}{b} = e^\beta$, then $b^2 = \exp\{-\gamma + \beta\}$ and $r^2 = \exp\{-\gamma - \beta\}$. Hence by measuring α_m and F (shown in figure A.1(b)), we find b and r . Now take the ratio of incident and coupled fields:

$$E(\lambda) = \frac{\epsilon_{cavity}(\lambda)}{\epsilon_{incident}} = \frac{t}{1 - rbe^{i\phi}} \quad (\text{A.12})$$

Giving the enhanced field intensity:

$$|E|^2(\lambda) = \frac{(1 - r^2)}{|1 - rbe^{i\phi}|^2} \quad (\text{A.13})$$

And by substitution from equation (A.7), the maximum field intensity on resonance:

$$I_m = \frac{(1 - r^2)}{(1 - rb)^2} = \frac{\alpha_m}{1 - b^2} \quad (\text{A.14})$$

For an emitter inside a cavity (shown schematically in figure A.1(c)) the field absorbed in the cavity is f_α and the field out-coupled is f_ϵ where:

$$f_\alpha = a(1 + bre^{i\phi} + [bre^{i\phi}] + \dots) \quad (\text{A.15})$$

$$f_\epsilon = tb(1 + bre^{i\phi} + [bre^{i\phi}] + \dots) \quad (\text{A.16})$$

A.2 Resonant Plasmon Model

Now the ratio of field absorbed in the cavity to the field out-coupled is:

$$\frac{f_\alpha}{f_\epsilon} = \frac{a}{tb} \quad (\text{A.17})$$

The ratio of intensities is:

$$\frac{|f_\alpha|^2}{|f_\epsilon|^2} = \frac{a^2}{(tb)^2} = \frac{(1 - b^2)}{b^2(1 - r^2)} \quad (\text{A.18})$$

So the fraction of light escaping \mathcal{F}_{out} is:

$$\mathcal{F}_{out} = \frac{f_\epsilon^2}{f_\alpha^2 + f_\epsilon^2} = \frac{1}{\frac{f_\alpha^2}{f_\epsilon^2} + 1} = \frac{1}{\frac{\frac{1}{b^2} - 1}{1 - r^2} + 1} \quad (\text{A.19})$$

Finally, this allows an expression for measured *SERS* signals:

$$SERS \propto |E_{in}|^2 |E_{out}|^2 \mathcal{F}_{out} \quad (\text{A.20})$$

where $|E_{in}|^2$ and $|E_{out}|^2$ are the enhanced field intensity at the input laser wavelength and Raman shifted wavelength respectively.

Appendix B

Publications

List of publications in order of authorship contribution.

Easily coupled whispering gallery plasmons in dielectric nanospheres embedded in gold films.

R.M.Cole, Y.Sugawara, J.J.Baumberg, S.Mahajan, M.Abdelsalam, and P.N.Bartlett.

Phys. Rev. Lett. 97: 137401, 2007

Understanding Plasmons in Nanoscale Voids.

R.M.Cole, J.J.Baumberg, J.G.de Abajo, S.Mahajan, M.Abdelsalam, and P.N.Bartlett.

Nano. Lett. 7(7): 2094 - 2100, 2007

Relating SERS Intensity to Specific Plasmon Modes on Sphere Segment Void Surfaces.

S.Mahajan, R.M.Cole, B.F.Soares, S.H.Pelfrey, A.E.Russell, J.J.Baumberg, and P.N.Bartlett.

J. Phys. Chem. C 21: 9284 - 9289, 2009

Fabrication of plasmonic Au nano-void trench arrays by guided self-assembly.

X.Li, R.M.Cole, C.A.Milhano, P.N.Bartlett, B.F.Soares, J.J.Baumberg, and C.H.de Groot.

Nanotechnology 20, 285309, 2009

Engineering SERS via Absorption Control in Novel Hybrid Ni/Au Nanovoids.
R.M.Cole, S.Mahajan, P.N.Bartlett, and J.J.Baumberg.
Optics Express 17, 13298, 2009

Stretchable Elastomeric Nanovoids for Tunable Plasmons.
R.M.Cole, S.Mahajan, P.N.Bartlett, and J.J.Baumberg.
APL Submitted 2009

Imaging optical near fields at metallic nanoscale voids.
P.D.Lacharmoise, N.G.Tognalli, A.R.Goi, M.I.Alonso, A.Fainstein, R.M.Cole,
J.J.Baumberg, J.G.de Abajo, and P.N.Bartlett.
Phys. Rev. B. 78: 125410, 2008

UV SERS at well ordered Pd sphere segment void (SSV) nanostructures.
L.Cui, S.Mahajan, R.M.Cole, B.Soares, P.N.Bartlett, J.J.Baumberg,
I.P.Hayward, B.Ren, A.E.Russell, and Z.Q.Tian.
Physical. Chemistry. Chemical. Physics. 11(7): 1023 - 1026, 2009

Localized and delocalized plasmons in metallic nanovoids.
T.A.Kelf, Y.Sugawara, R.M.Cole, J.J.Baumberg, M.E.Abdelsalam, S.Cintra,
S.Mahajan, A.E.Russell, and P.N.Bartlett.
Physical. Review. B. 74: 245415, 2006

Electrodeposition of Highly Ordered Macroporous Iridium Oxide Films
Through Self-assembled Colloidal Templates.
J.Hu, S.Mahajan, M.Abdelsalam, P.N.Bartlett, R.Cole, Y.Sugawara,
J.J.Baumberg, and G.Denuault.
J. Mater. Chem. 19: 3855 - 3858, 2009

References

- [1] Tim Kelf. Thesis. 2005. [2](#), [11](#), [30](#), [31](#), [32](#), [38](#), [45](#), [65](#), [87](#), [92](#)
- [2] T. A. Kelf, Y. Sugawara, R. M. Cole, J. J. Baumberg, M. E. Abdelsalam, S. Cintra, S. Mahajan, A. E. Russell, and P. N. Bartlett. Localized and de-localized plasmons in metallic nanovoids. *Physical Review B*, 74(24):245415, 2006. [3](#), [44](#), [72](#), [74](#)
- [3] P. Vukusic and J. R. Sambles. Photonic structures in biology. *Nature*, 424(6950):852–855, 2003. [6](#), [7](#)
- [4] <http://www.buygemstones.com>. [7](#)
- [5] <http://labsji.wordpress.com/2008/03/>. [7](#)
- [6] J. J. Baumberg. Breaking the mould: Casting on the nanometre scale. *Nature Materials*, 5:2–5, 2006. [7](#)
- [7] S. I. Bozhevolnyi, V. S. Volkov, E. Devaux, J. Y. Laluet, and T. W. Ebbesen. Channel plasmon subwavelength waveguide components including interferometers and ring resonators. *Nature*, 440(7083):508–511, 2006. [8](#), [9](#)
- [8] C. Ropers, C. C. Neacsu, M. B. Raschke, M. Albrecht, C. Lienau, and T. Elsaesser. Light confinement at ultrasharp metallic tips. *Japanese Journal of Applied Physics*, 47(7):6051–6054, 2008. [8](#), [9](#)
- [9] W. L. Barnes, A. Dereux, and T. W. Ebbesen. Surface plasmon subwavelength optics. *Nature*, 424(6950):824–830, 2003. [8](#), [26](#)

REFERENCES

- [10] B. Hecht, H. Bielefeldt, L. Novotny, Y. Inouye, and D. W. Pohl. Local excitation, scattering, and interference of surface plasmons. *Physical Review Letters*, 77(9):1889–1892, 1996. [9](#)
- [11] J. Pendry. Playing tricks with light. *Science*, 285(5434):1687, 1999. [9](#)
- [12] A. V. Krasavin, A. V. Zayats, and N. I. Zheludev. Active control of surface plasmonpolariton waves. *Journal of Optics A: Pure and Applied Optics*, 7(2):S85–S89, 2005. [9](#), [105](#)
- [13] S. Wang, D. F. P. Pile, C. Sun, and X. Zhang. Nanopin plasmonic resonator array and its optical properties. *Nano Letters*, 7(4):1076–1080, 2007. [9](#), [10](#)
- [14] K. Li, L. Clime, B. Cui, and T. Veres. Surface enhanced raman scattering on long-range ordered noble-metal nanocrescent arrays. *Nanotechnology*, 19(14):145305, 2008. [9](#), [10](#)
- [15] B. J. Wiley, Y. Chen, J. M. McLellan, Y. Xiong, Z. Y. Li, D. Ginger, and Y. Xia. Synthesis and optical properties of silver nanobars and nanorice. *Nano Letters*, 7(4):10321036, 2007. [9](#), [10](#)
- [16] K. Kneipp, Y. Wang, H. Kneipp, L. T. Perelman, I. Itzkan, R. R. Dasari, and M. S. Feld. Single molecule detection using surface-enhanced raman scattering (sers). *Physical Review Letters*, 78(9):1667–1670, 1997. [9](#)
- [17] S. Nie and S. R. Emory. Probing single molecules and single nanoparticles by surface-enhanced raman scattering. *Science*, 275(5303):1102, 1997. [9](#)
- [18] N. Anderson, A. Bouhelier, and L. Novotny. Near-field photonics: tip-enhanced microscopy and spectroscopy on the nanoscale. *Journal of Optics A Pure And Applied Optics*, 8(4):227, 2006. [9](#)
- [19] A. J. Babadjanyan, N. L. Margaryan, and K. V. Nerkararyan. Superfocusing of surface polaritons in the conical structure. *Journal of Applied Physics*, 87:3785, 2000. [9](#)
- [20] M. I. Stockman. Nanofocusing of optical energy in tapered plasmonic waveguides. *Physical Review Letters*, 93(13):137404, 2004. [9](#)

REFERENCES

- [21] A. Bouhelier, J. Renger, M. R. Beversluis, and L. Novotny. Plasmon-coupled tip-enhanced near-field optical microscopy. *Journal of Microscopy*, 210(3):220–224, 2003. [9](#)
- [22] D. Mehtani, N. Lee, R. D. Hartschuh, A. Kisliuk, M. D. Foster, A. P. Sokolov, F. Cajko, and I. Tsukerman. Optical properties and enhancement factors of the tips for apertureless near-field optics. *Journal Of Optics A Pure And Applied Optics*, 8(4):183, 2006. [9](#)
- [23] D. K. Gramotnev and K. C. Vernon. Adiabatic nano-focusing of plasmons by sharp metallic wedges. *Applied Physics B: Lasers and Optics*, 86(1):7–17, 2007. [9, 10](#)
- [24] L. Novotny, D. W. Pohl, and B. Hecht. Light confinement in scanning near-field optical microscopy. *Ultramicroscopy*, 61(1-4):1–9, 1995. [9](#)
- [25] K. Li, M. I. Stockman, and D. J. Bergman. Self-similar chain of metal nanospheres as an efficient nanolens. *Physical Review Letters*, 91(22):227402, 2003. [9](#)
- [26] Z. Liu, J. M. Steele, W. Srituravanich, Y. Pikus, C. Sun, and X. Zhang. Focusing surface plasmons with a plasmonic lens. *Nano Letters*, 5(9):1726–1729, 2005. [9](#)
- [27] D. K. Gramotnev. Adiabatic nanofocusing of plasmons by sharp metallic grooves: Geometrical optics approach. *Journal of Applied Physics*, 98:104302, 2005. [10](#)
- [28] K. V. Nerkararyan. Superfocusing of a surface polariton in a wedge-like structure. *Physics Letters A*, 237(1-2):103–105, 1997. [10](#)
- [29] D. F. P. Pile and D. K. Gramotnev. Adiabatic and nonadiabatic nanofo-cusing of plasmons by tapered gap plasmon waveguides. *Applied Physics Letters*, 89:041111, 2006. [10](#)
- [30] K. Su, S. Durant, J. M. Steele, Y. Xiong, C. Sun, and X. Zhang. Raman enhancement factor of a single tunable nanoplasmonic resonator. *Journal Of Physical Chemistry B*, 110(9):3964, 2006. [10](#)

REFERENCES

- [31] T. R. Jensen, M. D. Malinsky, C. L. Haynes, and R. P. Van Duyne. Nanosphere lithography: tunable localized surface plasmon resonance spectra of silver nanoparticles. *Journal of Physical Chemistry B*, 104(45):1054910556, 2000. [10](#)
- [32] Z. Chen, A. Taflove, and V. Backman. Highly efficient optical coupling and transport phenomena in chains of dielectric microspheres. *Optics Letters*, 31(3):389–391, 2006. [10](#), [69](#)
- [33] L. J. Sherry, S. H. Chang, G. C. Schatz, R. P. Van Duyne, B. J. Wiley, and Y. Xia. Localized surface plasmon resonance spectroscopy of single silver nanocubes. *Nano Letters*, 5(10):20342038, 2005. [10](#)
- [34] Archimedes. <http://www.mlahanas.de/greeks/mirrors.htm>. [10](#)
- [35] Jewelery. <http://en.wikipedia.org/wiki/jewelery>. [10](#)
- [36] G. Mie. Beitrage zur optik truber medien, speziell kolloidaler metallosungen. *Ann. Phys.*, 25(4):377–445, 1908. [11](#)
- [37] M. Born and E. Wolf. *Principles of Optics: Electromagnetic Theory of Propagation, Interference and Diffraction of Light*. Cambridge University Press, 1999. [12](#), [15](#)
- [38] C. F. Bohern and D. R. Huffman. Absorption and scattering of light by small particles. *J. Wiley Sons, New York*, 1983. [14](#), [17](#)
- [39] S. Kupratakuln and G. C. Fletcher. Electron band structure of gold. *Journal of Physics C: Solid State Physics*, 2:1886–1888, 1969. [17](#)
- [40] M. Winter. Webelements tm. URL: <http://www.webelements.com>, 2003. [18](#)
- [41] D. W. Lynch and W. R. Hunter. Comments on the optical constants of metals and an introduction to the data for several metals. *Handbook of Optical Constants of Solids*, page 275, 1985. [18](#)

REFERENCES

- [42] P. B. Johnson and R. W. Christy. Optical constants of the noble metals. *Physical Review B*, 6(12):4370–4379, 1972. [18](#), [19](#), [23](#), [25](#), [43](#)
- [43] M. A. Ordal, L. L. Long, R. J. Bell, S. E. Bell, R. R. Bell, R. W. Alexander, and C. A. Ward. Optical properties of the metals al, co, cu, au, fe, pb, ni, pd, pt, ag, ti, and w in the infrared and far infrared. *Applied Optics*, 22(7):1099–1119, 1983. [18](#)
- [44] G. B. Irani, T. Huen, and F. Wooten. Optical constants of silver and gold in the visible and vacuum ultraviolet. *Journal of the Optical Society of America*, 61(1):128, 1971. [19](#)
- [45] H. Ehrenreich and H. R. Philipp. Optical properties of ag and cu. *Physical Review*, 128(4):1622–1629, 1962. [19](#)
- [46] A. J. McAlister and E. A. Stern. Plasma resonance absorption in thin metal films. *Physical Review*, 132(4):1599–1602, 1963. [19](#)
- [47] R. H. Ritchie. Plasma losses by fast electrons in thin films. *Physical Review*, 106(5):874–881, 1957. [19](#)
- [48] H. Raether. *Surface plasmons on smooth and rough surfaces and on gratings*. Springer-Verlag New York, 1988. [21](#), [26](#)
- [49] E. D. Palik. *Handbook of Optical Constants of Solids*. Academic Press, 1985. [25](#)
- [50] F. J. Garica de Abajo. Colloquium: Light scattering by particle and hole arrays. *Reviews Of Modern Physics*, 79(4):1267, 2007. [25](#)
- [51] A. S. Barker Jr. Optical measurements of surface plasmons in gold. *Physical Review B*, 8(12):5418–5426, 1973. [26](#)
- [52] D. J. Nash and J. R. Sambles. Simultaneous observation of surface plasmons on both sides of thin silver films. *Journal of Modern Optics*, 46(12):1793–1800, 1999. [26](#)

REFERENCES

- [53] A. E. Craig, G. A. Olson, and D. Sarid. Experimental observation of the long-range surface-plasmon polariton. *Optics Letters*, 8:380–382, 1983. [26](#)
- [54] P. N. Bartlett, J. J. Baumberg, S. Coyle, and M. E. Abdelsalam. Optical properties of nanostructured metal films. *Faraday Discussions*, 125:117–132, 2004. [28](#), [29](#)
- [55] P. N. Bartlett, J. J. Baumberg, P. R. Birkin, M. A. Ghanem, and M. C. Netti. Highly ordered macroporous gold and platinum films formed by electrochemical deposition through templates assembled from submicron diameter monodisperse polystyrene spheres. *Chemistry Of Materials*, 14(5):2199–2208, 2002. [29](#)
- [56] M. C. Netti, S. Coyle, J. J. Baumberg, M. A. Ghanem, P. R. Birkin, P. N. Bartlett, and D. M. Whittaker. Confined surface plasmons in gold photonic nanocavities. *Advanced Materials*, 13(18):1368, 2001. [29](#)
- [57] S. Coyle, M. C. Netti, J. J. Baumberg, M. A. Ghanem, P. R. Birkin, P. N. Bartlett, and D. M. Whittaker. Confined plasmons in metallic nanocavities. *Physical Review Letters*, 87(17):176801, 2001. [29](#), [46](#), [69](#)
- [58] T. V. Teperik, V. V. Popov, F. J. Garca de Abajo, M. Abdelsalam, P. N. Bartlett, T. A. Kelf, Y. Sugawara, and J. J. Baumberg. Strong coupling of light to flat metals via a buried nanovoid lattice: the interplay of localized and free plasmons. *Optics Express*, 14(5):1965–1972, 2006. [43](#)
- [59] N. M. B. Perney, J. J. Baumberg, M. E. Zoorob, M. D. B. Charlton, S. Mahnkopf, and C. M. Netti. Tuning localized plasmons in nanostructured substrates for surface-enhanced raman scattering. *Optics Express*, 14(2):847–857, 2006. [45](#), [94](#)
- [60] A. D. Boardman. *Electromagnetic surface modes*. Wiley, 1982. [46](#), [69](#), [70](#)
- [61] F. J. Garca de Abajo and A. Howie. Relativistic electron energy loss and electron-induced photon emission in inhomogeneous dielectrics. *Physical Review Letters*, 80(23):5180–5183, 1998. [46](#)

REFERENCES

- [62] J. Kim, G. Liu, Y. Lu, and L. Lee. Intra-particle plasmonic coupling of tip and cavity resonance modes in metallic apertured nanocavities. *Opt. Express*, 13:8332–8338, 2005. [48](#)
- [63] M. Cortie and M. Ford. A plasmon-induced current loop in gold semi-shells. *Nanotechnology*, 18(23):235704, 2007. [48](#)
- [64] R. M. Cole, Y. Sugawara, J. J. Baumberg, S. Mahajan, M. Abdelsalam, and P. N. Bartlett. Easily coupled whispering gallery plasmons in dielectric nanospheres embedded in gold films. *Physical Review Letters*, 97:137401, 2007. [52](#)
- [65] J. D. Jackson. Classical electrodynamics. NY: Wiley, 1999. [52](#)
- [66] M. E. Abdelsalam, P. N. Bartlett, J. J. Baumberg, and S. Coyle. Preparation of arrays of isolated spherical cavities by self-assembly of polystyrene spheres on self-assembled pre-patterned macroporous films. *Advanced Materials*, 16(1), 2004. [58](#)
- [67] S. Mahajan D. Zhang A.E. Russell J.J. Baumberg, B.N. Soares and P.N. Bartlett. Enhancing infra-red absorption with scalable nanovoid metamaterials. *Submitted to Optics Express*, 2009. [58](#)
- [68] J. Zhou, T. Koschny, M. Kafesaki, E. N. Economou, J. B. Pendry, and C. M. Soukoulis. Saturation of the magnetic response of split-ring resonators at optical frequencies. *J. Nonlinear Opt. Phys. Mater Phys Rev Lett*, 95:223902, 2002. [58](#)
- [69] P. D. Lacharmoise, N. G. Tognalli, A. R. Goi, M. I. Alonso, A. Fainstein, R. M. Cole, J. J. Baumberg, J. G. de Abajo, and P. N. Bartlett. Imaging optical near fields at metallic nanoscale voids. *Faraday Discuss Phys Rev B*, 78:125410, 2008. [60, 61](#)
- [70] J. Homola, S. S. Yee, and G. Gauglitz. Surface plasmon resonance sensors: review. *Sensors Actuators: B. Chemical*, 54(1-2):3–15, 1999. [65](#)
- [71] <http://www.philiplaven.com/p20.html>. 2009. [65](#)

REFERENCES

- [72] A. C. R. Pipino, J. W. Hudgens, and R. E. Huie. Evanescent wave cavity ring-down spectroscopy with a total-internal-reflection minicavity. *Review of Scientific Instruments*, 68:2978, 1997. [66](#)
- [73] C. Gu, Y. Xu, Y. Liu, J. J. Pan, F. Zhou, and H. He. Applications of photorefractive materials in information storage, processing and communication. *Optical Materials*, 23(1-2):219–227, 2003. [66](#)
- [74] J. P. Laine, B. E. Little, and H. A. Haus. Etch-eroded fiber coupler for whispering-gallery-mode excitation inhigh-q silica microspheres. *Photonics Technology Letters, IEEE*, 11(11):1429–1430, 1999. [66](#)
- [75] Y. P. Rakovich, J. F. Donegan, M. Gerlach, A. L. Bradley, T. M. Connolly, J. J. Boland, N. Gaponik, and A. Rogach. Fine structure of coupled optical modes in photonic molecules. *Physical Review A*, 70(5):51801, 2004. [66](#)
- [76] V. S. Ilchenko, X. S. Yao, and L. Maleki. Pigtailing the high-q microsphere cavity: a simple fiber coupler for optical whispering-gallery modes. *Optics Letters*, 24(11):723–725, 1999. [66](#)
- [77] M. Cai, O. Painter, K. J. Vahala, and P. C. Sercel. Fiber-coupled microsphere laser. *Optics Letters*, 25(19):1430–1432, 2000. [66](#)
- [78] Kerry J. Vahala. Optical microcavities. *Nature*, 424(6950):839–846, 2003. [67](#)
- [79] S. Arnold, M. Khoshima, I. Teraoka, S. Holler, and F. Vollmer. Shift of whispering-gallery modes in microspheres by protein adsorption. *Optics Letters*, 28(4):272–274, 2003. [67](#)
- [80] T. Kipp, K. Petter, C. Heyn, D. Heitmann, and C. Schller. Broadband emission and low absorption in microdisks with algaas quantum wells. *Applied Physics Letters*, 84:1477, 2004. [67](#)
- [81] T. Mukaiyama, K. Takeda, H. Miyazaki, Y. Jimba, and M. Kuwata-Gonokami. Tight-binding photonic molecule modes of resonant bispheres. *Physical Review Letters*, 82(23):4623, 1999. [74](#)

REFERENCES

- [82] M. Fleischmann, P. J. Hendra, and A. J. McQuillan. Raman spectra of pyridine adsorbed at a silver electrode. *Chemical Physics Letters*, 26(2), 1974. [88](#)
- [83] C. L. Haynes and R. P. Van Duyne. Plasmon-sampled surface-enhanced raman excitation spectroscopy. *Journal of Physical Chemistry B*, 107(30):7426 – 7433, 2003. [88](#), [89](#)
- [84] J. Aizpurua, P. Hanarp, D. S. Sutherland, M. Kall, G. W. Bryant, and F. J. G. de Abajo. Optical properties of nanorings. *Physical Review Letters*, 90:57401, 2003. [88](#)
- [85] S. J. Oldenburg, R. D. Averitt, S. L. Westcott, and N. J. Halas. Nanoengineering of optical resonances. *Chemical Physics Letters*, 288(2-4):243–247, 1998. [88](#)
- [86] P. M. Tessier, O. D. Velev, A. T. Kalambur, J. F. Rabolt, A. M. Lenhoff, and E. W. Kaler. Assembly of gold nanostructured films templated by colloidal crystals and use in surface-enhanced raman spectroscopy. *Journal of the American Chemical Society*, 122(39):9554–9555, 2000. [88](#)
- [87] L. Cui, S. Mahajan, R. M. Cole, B. Soares, P. N. Bartlett, J. J. Baumberg, I. P. Hayward, B. Ren, A. E. Russell, and Z. Q. Tian. Uv sers at well ordered pd sphere segment void (ssv) nanostructures. *Physical Chemistry Chemical Physics*, 11(7):1023–1026, 2009. [88](#)
- [88] S. Mahajan, M. Abdelsalam, Y. Suguwara, S. Cintra, A. Russell, J. Baumberg, and P. Bartlett. Tuning plasmons on nano-structured substrates for nir-sers. *Physical Chemistry Chemical Physics*, 9(1):104–109, 2007. [88](#)
- [89] M. Abdelsalam, P. N. Bartlett, A. E. Russell, J. J. Baumberg, E. J. Calvo, N. G. Tognalli, and A. Fainstein. Quantitative electrochemical sers of flavin at a structured silver surface. *LANGMUIR*, 24(13):7018–7023, 2008. [89](#)
- [90] S. Mahajan, J. Richardson, T. Brown, and P. N. Bartlett. Sers-melting: A new method for discriminating mutations in dna sequences. *Journal of the American Chemical Society*, 130(46):15589–15601, 2008. [89](#), [96](#)

REFERENCES

- [91] S. Lal, N. K. Grady, J. Kundu, C. S. Levin, J. B. Lassiter, and N. J. Halas. Tailoring plasmonic substrates for surface enhanced spectroscopies. *Chemical Society Reviews*, 37(5):898–911, 2008. [89](#)
- [92] M. Moskovits. Surface-enhanced spectroscopy. *Reviews Of Modern Physics*, 57(3):783–826, 1985. [98](#)
- [93] M. Moskovits. Surface-enhanced raman spectroscopy: a brief retrospective. *Journal of Raman Spectroscopy*, 36(6-7):485496, 2005. [98](#)
- [94] A. Ulman. Formation and structure of self-assembled monolayers. *Chemical Reviews*, 96(4):1533, 1996. [102](#)
- [95] J. C. Love, L. A. Estroff, J. K. Kriebel, R. G. Nuzzo, and G. M. Whitesides. Self-assembled monolayers of thiolates on metals as a form of nanotechnology. *Chemical Reviews*, 105(4):1103–1170, 2005. [102](#)
- [96] Z. Mekhalif, J. Riga, J. J. Pireaux, and J. Delhalle. Self-assembled monolayers of n-dodecanethiol on electrochemically modified polycrystalline nickel surfaces. *LANGMUIR*, 13(8):2285–2290, 1997. [102](#)
- [97] Z. Mekhalif, F. Laffineur, N. Couturier, and J. Delhalle. Elaboration of self-assembled monolayers of n-alkanethiols on nickel polycrystalline substrates: time, concentration, and solvent effects. *LANGMUIR*, 19(3):637–645, 2003. [102](#)
- [98] W. Dickson, G. A. Wurtz, P. R. Evans, R. J. Pollard, and A. V. Zayats. Electronically controlled surface plasmon dispersion and optical transmission through metallic hole arrays using liquid crystal. *Nano Lett*, 8(1):281–286, 2008. [105](#)
- [99] H. L. Chen, K. C. Hsieh, C. H. Lin, and S. H. Chen. Using direct nanoimprinting of ferroelectric films to prepare devices exhibiting bi-directionally tunable surface plasmon resonances. *Nanotechnology*, 19(435304):435304, 2008. [105](#)

REFERENCES

- [100] G. Xu, Y. Chen, M. Tazawa, and P. Jin. Surface plasmon resonance of silver nanoparticles on vanadium dioxide. *J. Phys. Chem. B*, 110(5):2051–2056, 2006. [105](#)
- [101] G. Xu, C. M. Huang, M. Tazawa, P. Jin, and D. M. Chen. Nano-ag on vanadium dioxide. ii. thermal tuning of surface plasmon resonance. *Journal of Applied Physics*, 104:053102, 2008. [105](#)
- [102] S. Rehwald, M. Berndt, F. Katzenberg, S. Schwieger, E. Runge, K. Schierbaum, and D. Zerulla. Tunable nanowires: An additional degree of freedom in plasmonics. *Physical Review B*, 76(8):85420, 2007. [105](#)
- [103] S. Olcum, A. Kocabas, G. Ertas, A. Atalar, and A. Aydinli. Tunable surface plasmon resonance on an elastomeric substrate. *Optics Express*, 17(10):8542–8547, 2009. [105](#), [106](#)
- [104] D. K. Avasthi, Y. K. Mishra, D. Kabiraj, N. P. Lalla, and J. C. Pivin. Synthesis of metal-polymer nanocomposite for optical applications. *Nanotechnology*, 18(12):125604, 2007. [105](#)
- [105] M. Aschwanden and A. Stemmer. Polymeric, electrically tunable diffraction grating based on artificial muscles. *Optics Letters*, 31(17):2610–2612, 2006. [106](#)
- [106] T. Li, Z. Huang, Z. Suo, S. P. Lacour, and S. Wagner. Stretchability of thin metal films on elastomer substrates. *Applied Physics Letters*, 85:3435, 2004. [109](#)
- [107] S. L. Bazhenov, A. L. Volynskii, V. M. Alexandrov, and N. F. Bakeev. Two mechanisms of the fragmentation of thin coatings on rubber substrates. *Journal Of Polymer Science Part B Polymer Physics*, 40(1):10–18, 2002. [109](#)
- [108] A. L. Volynskii, S. Bazhenov, O. V. Lebedeva, and N. F. Bakeev. Mechanical buckling instability of thin coatings deposited on soft polymer substrates. *Journal of Materials Science*, 35(3):547–554, 2000. [110](#)

REFERENCES

- [109] A. D. McFarland, M. A. Young, J. A. Dieringer, and R. P. Van Duyne. Wavelength-scanned surface-enhanced raman excitation spectroscopy. *Journal of Physical Chemistry B*, 109(22):11279–11285, 2005. [119](#)